Title
Thermal Decomposition Mechanisms of Molecules Relevant to Chemical Vapor Deposition and Fuel Combustion by Flash Pyrolysis Photoionization Time-of-Flight Mass Spectrometry

Author
Shao, Kuanliang

Publication Date
2023

UNIVERSITY OF CALIFORNIA
RIVERSIDE

Thermal Decomposition Mechanisms of Molecules Relevant to Chemical Vapor Deposition and Fuel Combustion by Flash Pyrolysis Photoionization Time-of-Flight Mass Spectrometry

A Dissertation submitted in partial satisfaction
of the requirements for the degree of

Doctor of Philosophy

in

Chemistry

by

Kuanliang Shao

June 2023

Dissertation Committee:
Dr. Jingsong Zhang, Chairperson
Dr. James Davies
Dr. Francisco Zaera

The Dissertation of Kuanliang Shao is approved:

Committee Chairperson

University of California, Riverside

PUBLICATIONS AND CONTRIBUTIONS TO THE DISSERTATION

The following chapters in this dissertation have been published, either in whole or in part, as part of prior work:

Chapter 3: "Thermal decomposition mechanism of allyltrichlorosilane and allyltrimethylsilane"

Published in: Shao, K.; Tian, Y.; Zhang, J., *International Journal of Mass Spectrometry* **2021**, *460*, 116476.

Chapter 4: "Mechanistic study of thermal decomposition of 1,1,2,2-tetramethyldisilane"

Published in: Shao, K.; Tian, Y.; Zhang, J., *The Journal of Physical Chemistry A* **2022**, *126*, 1085-1093.

Chapter 5: "Flash pyrolysis mechanism of trimethylchlorosilane"

Published in: Shao, K.; Brunson, J.; Tian, Y.; Zhang, J., *International Journal of Mass Spectrometry* **2022**, *482*, 116933.

Chapter 6: "Thermal Decomposition Mechanism of Tetraethylsilane: The Competition between β-Hydride Elimination and Bond Homolysis"

Published in: Shao, K.; Liu, X.; Zhang, J., *The Journal of Physical Chemistry A*. **2023**, *127*, 3966–3975

Chapter 7: "Thermal decomposition of cyclohexane by flash pyrolysis: A study on the initial unimolecular decomposition mechanism"

Published in: Shao, K.; Liu, X.; Jones, P. J.; Sun, G.; Gomez, M.; Riser, B. P.; Zhang, J., *Physical Chemistry Chemical Physics* **2021**, *23*, 9804-9813.

Chapter 8: "Flash pyrolysis vacuum ultraviolet photoionization mass spectrometry of cycloheptane"

Published in: Shao, K.; Liu, X.; Zhang, J., *The Journal of Physical Chemistry A*. **2023**. doi.org/10.1021/acs.jpca.2c09081

ACKNOWLEDGEMENT

I would like to express my deepest gratitude to Professor Jingsong Zhang, my esteemed PhD advisor, for his invaluable guidance, unwavering support, and constant encouragement throughout the entire journey of this research. His expertise, wisdom, and commitment to excellence have been critical in shaping my academic and research endeavors.

I am also grateful to Professor James Davies, Professor Francisco Zaera, Professor Leonard Mueller, Professor De-en Jiang, Professor Yadong Yin, and Professor Gregory Beran for their dedicated instruction and mentorship during my graduate-level courses. Their profound knowledge, rigorous teaching, and insightful feedback have greatly enriched my understanding and development in Chemistry study.

I would like to extend my heartfelt appreciation to Dr. Kevin Simpson, Dr. Rena Hayashi, Professor Haofei Zhang, and Krisanto Pranata for their invaluable assistance during my time as a Teaching Assistant. Their guidance, patience, and support have played a pivotal role in my growth as an educator and researcher.

Furthermore, I am deeply indebted to Christina Youhas and Prisciliano Saavedra for their exceptional help during my academic study and general research work. Their diligence, professionalism, and willingness to lend a helping hand have made a significant impact on the success of my research endeavors.

I would also like to acknowledge the support and encouragement from my family, my friends, and my church community who have been a constant source of inspiration and motivation throughout this challenging but rewarding journey.

I am humbled by the collective efforts and contributions of all those mentioned above, as well as countless others who have played a role in shaping my academic journey. I am truly grateful for their unwavering support, and I am honored to have had the privilege of working with such exceptional individuals.

Thank you all for your immeasurable contributions, encouragement, and support.

ABSTRACT OF THE DISSERTATION

Thermal Decomposition Mechanisms of Molecules Relevant to Chemical Vapor Deposition and Fuel Combustion by Flash Pyrolysis Photoionization Time-of-Flight Mass Spectrometry

by

Kuanliang Shao

Doctor of Philosophy, Graduate Program in Chemistry
University of California, Riverside, June 2023
Dr. Jingsong Zhang, Chairperson

Flash pyrolysis microreactor coupled with molecular beam extraction and photoionization time-of-flight mass spectrometry along with theoretical calculations are employed to study the pyrolysis of gas phase molecules with relevance to chemical vapor deposition (CVD) and fuel combustion. This dissertation presents a comprehensive exploration of the flash pyrolysis mechanisms of various organosilanes and hydrocarbons, including allyltrichlorosilane, allyltrimethylsilane, 1,1,2,2-tetraethylsilane, trimethylchlorosilane, tetraethylsilane, cyclohexane, and cycloheptane.

Chapters 3 to 6 of this dissertation focus on investigating the decomposition pathways and identifying key reaction products of various CVD precursors through a combination of experimental observations and theoretical analyses. The study specifically examines allyltrichlorosilane, allyltrimethylsilane, 1,1,2,2-tetramethylsilane, trimethylchlorosilane, and tetraethylsilane. The findings reveal that allyltrichlorosilane decomposes primarily through Si-C bond homolysis, while the thermal decomposition of allyltrimethylsilane proceeds primarily via molecular eliminations. The pyrolysis of

1,1,2,2-tetramethylsilane involves molecular elimination reactions, Si-Si bond fission, H_2 elimination, and decomposition to trimethylsilane and methylsilylene. Trimethylchlorosilane predominantly undergoes HCl molecular elimination, while tetraethylsilane follows Si-C bond homolysis. These studies have conducted a thorough examination of the pyrolysis mechanism of organosilane precursors, providing a comprehensive overview, and investigating their potential applications in SiC thin film production.

Additionally, Chapters 7 and 8 explore the thermal decomposition mechanisms of cyclohexane and cycloheptane, elucidating the diradical mechanism in the primary initiation reactions. These comprehensive studies provide valuable insights into the intricate pyrolysis mechanisms of organosilanes and aviation fuel prototypes, facilitating the development of accurate models and efficient utilization strategies for these compounds.

LIST OF CONTENTS

ACKNOWLEDGMENT

CHAPTER

LIST OF FIGURES

LIST OF SCHEMES

CHAPTER 1 Introduction

1.1 Pyrolysis.

Pyrolysis is a chemical process that involves the thermal decomposition of organic materials in the absence of oxygen.[1] During pyrolysis, materials are heated to a high temperature and break down into smaller pieces; then those smaller fragments could be collected, analyzed, and utilized for various purposes. Pyrolysis is used extensively in the chemical industry field to produce many forms of chemicals, such as petroleum, coal, SiC thin films, and to treat organic waste materials.[2] Pyrolysis is also used to convert post-consumer plastic waste into chemicals, to transform heavier hydrocarbons into lighter ones under high temperatures, and to thermo-chemically treat biomass.[3] Pyrolysis-related material processing techniques also allow for the fabrication of SiC-based materials at a lower temperature compared to traditional approaches.[4] In this work, the applications of pyrolysis on the SiC thin film production and fuel combustion modeling will be discussed in detail.

Pyrolysis process can be used in the manufacturing of a wide range of organic materials into valuable products, such as SiC thin films.[5] SiC is a promising material due to its unique properties, such as hardness, high thermal conductivity, thermal shock resistance, chemical inertness, and large band gap.[6] Pyrolysis methods using chemical vapor deposition (CVD) method for SiC thin film production involve the introduction of the precursor mixture, gas phase chemical reactions of the precursor which leads to the decomposition of a suitable precursor material at high temperatures in the absence of oxygen, and finally production of the thin film of SiC that can be deposited on the substrate.[7, 8] One of the advantages of this technique is that it allows for the deposition of uniform thin films with controlled thickness, morphology, and crystallinity.[9-11] This single precursor pyrolysis process can also be readily scaled up for industrial applications, and it is relatively cost-effective compared to other methods.[12, 13]

Pyrolysis has also been widely used in the study of fuel combustion modeling, and it is an important method to understand the fundamental mechanisms of pyrolysis and combustion processes, and to develop more efficient and environmentally friendly combustion systems.[14, 15] In fuel combustion modeling, pyrolysis is used to simulate the initial decomposition of fuel molecules into smaller, more reactive species, which then undergo further reactions to produce more products. This approach can provide insight into the chemical kinetics, heat transfer, and mass transfer processes that occur during fuel combustion, which are crucial for the optimization of combustion efficiency and reducing pollutant emissions.[16-18] With ongoing research and development, the study of pyrolysis is predicted to have an increasingly significant impact on the field of fuel combustion. It is expected to contribute towards the development of more sustainable and energy-efficient systems.

1.2 Flash pyrolysis method.

To fully understand the mechanism of a pyrolysis reaction, it is important to study the early-stage reactive intermediates involved in the thermal decomposition process. The thermal degradation of molecules involves the breakdown of larger molecules into smaller fragments, and those newly formed fragments (intermediates) can undergo a series of secondary reactions to form other smaller fragments.[19, 20] Some of those intermediates, for example free radicals, are highly reactive and have very short lifetime, which makes it challenging for them to be detected in the process.[20] By studying these intermediates, researchers can have an insight into the fundamental mechanism of the reaction and can identify different reaction pathways. Therefore, it is crucial to investigate the early-stage reactive intermediates for the full characterization of the reaction mechanism in a pyrolysis reaction.

Unfortunately, traditional pyrolysis studies cannot provide direct information on the early-stage intermediates. The pyrolysis kinetic study approaches, such as static reactors, flow reactors, or shock tubes method, typically have pyrolysis and sampling times on the scale of 10 ms to 10 s, and rely on the detection of stable, detectable products to infer the identities of possible reactive intermediates.[21, 22] Despite the advancements in theoretical chemistry method and computational modeling, a comprehensive understanding of the pyrolysis mechanisms still requires direct identifications of as many intermediates and their kinetic parameters. Failure to address some of the key reaction intermediates, or even the products, would lead to problematic numerical simulation that does not fit the experimental data.[23, 24] Therefore, conventional kinetic study methods have made it challenging to verify and improve current kinetic models and identify previously underestimated reaction pathways.

In this work, a flash pyrolysis micro-reactor coupled with supersonic cooling and vacuum ultraviolet photoionization mass spectrometry (VUV-PI-TOFMS) is used to overcome the limitations of traditional approaches to directly identify initial labile reaction intermediates. The technique involves using a SiC microreactor with a short residence time (~ 100 μs), followed by expanding the after-pyrolysis mixtures into vacuum and undergoing supersonic cooling to freeze the species in a molecular beam.[25-27] The frozen species are then sampled by a skimmer and intercepted and ionized by a VUV radiation beam in the photoionization region, and their signals are then recorded by the mass spectrometry detector, which achieves the identifications of the unreacted reactants, intermediates, and products in the pyrolysis reaction. Thus, the limitations of the conventional methods for identifying reactive intermediates in pyrolysis reactions are overcome, making it possible to obtain more comprehensive information on the reaction mechanisms.

1.3 Flash pyrolysis studies in this work.

This thesis consists of two major components of study. The first part focuses on the flash pyrolysis study of several gas-phase organosilane molecules. The main focus of this part of the study is to investigate the initiation steps of the pyrolysis reaction by identifying reactive intermediates in the system. To determine the most favorable reaction, the energetics of several competing reactions are calculated. Based on the mass spectra and computational chemistry results, several secondary reaction routes are also proposed, resulting in a more comprehensive report of the pyrolysis mechanism. Additionally, important parameters that would be of interest to the semiconductor industry are provided, including the onset temperature for the organosilane pyrolysis and the onset temperature to produce SiC. This component will include the mechanistic study of allyltrichlorosilane, allyltrimethlysilane,[28] 1,1,2,2-tetramethylsilane,[29] trimethylchlorosilane,[30] and tetraethylsilane.[31] In the study of trimethylchlorosilane and tetraethylsilane, a new transition state theory calculation protocol is employed to generate more convincing theoretical interpretations of the experimental results.

The second component is the pyrolysis study of two cycloalkane molecules, and their applications in fuel combustion modeling.[32, 33] The main objective of this component is to investigate the initiation of cycloalkane pyrolysis by examining the reactive intermediates of two critical diradicals, namely, 1,6-cyclohexyl diradical and 1,7-heptyl diradical, and their dissociation pathways. The results provide evidence to support the diradical mechanism of their decomposition, which resolves a long-standing debate on how cycloalkane pyrolysis is initiated. Additionally, several important thermodynamic parameters are reported to help construct an improved cycloalkane combustion model.

REFERENCE

1. G. Wang, Y. Dai, H. Yang, Q. Xiong, K. Wang, J. Zhou, Y. Li and S. Wang, *Energy & Fuels*, 2020, **34**, 15557-15578.

2. M. Holubčík, I. Klačková and P. Ďurčanský, *Energies*, 2020, **13**, 4849.

3. N. Cai, H. Zhang, J. Nie, Y. Deng and J. Baeyens, *IOP Conference Series: Earth and Environmental Science*, 2020, **586**, 012001.

4. D. A. Hoffman and R. A. Fitz, *Environmental Science & Technology*, 1968, **2**, 1023-1026.

5. R. R. Amashaev, N. M.-R. Alikhanov, A. M. Ismailov and I. M. Abdulagatov, *Journal of Vacuum Science & Technology A*, 2022, **40**, 052401.

6. M. A. H. Mohd Sohor, M. Mustapha and J. Chandra Kurnia, *MATEC Web Conf.*, 2017, **131**, 04003.

7. C.-S. Hsu and B.-H. Hwang, *Journal of The Electrochemical Society*, 2006, **153**, A1478.

8. L. V. Interrante, W. R. Schmidt, P. S. Marchetti and G. E. Maciel, *MRS Online Proceedings Library*, 1992, **271**, 739-748.

9. K. P. Nolan and J. S. Shapiro, *Journal of Polymer Science: Polymer Symposia*, 1976, **55**, 201-209.

10. G. Bailey, R. Dimlich, K. Alexander, J. McCarthy, T. Pretlow, A. Garg, D. R. Hull and R. T. Bhatt, *Microscopy and Microanalysis*, 1997, **3**, 743-744.

11. Z. Zhang, F. Wang, X. Yu, Y. Wang, Y. Yan, K. Li and Z. Luan, *Journal of the American Ceramic Society*, 2009, **92**, 260-263.

12. A. Hess, R. Parro, J. Du, J. Dunning, M. Scardelletti and C. A. Zorman, *MRS Online Proceedings Library*, 2007, **1009**, 403.

13. J. Du, N. Singh, J. B. Summers and C. A. Zorman, *MRS Online Proceedings Library*, 2011, **911**, 528.

14. H. Zhang, S. Shao, G. Ryabov, Y. Jiang and R. Xiao, *Energy & Fuels*, 2017, **31**, 13639-13646.

15. M. Piaskowska-Silarska, S. Gumuła, K. Pytel and P. Migo, *E3S Web Conf.*, 2017, **14**, 02016.

16. F. Vidian, A. Surjosatyo and Y. S. Nugroho, *Journal of Combustion*, 2016, **2016**, 9243651.

17. S. Su, C. Chen, L. Wang, C. Wei, H. Cui and C. Guo, *AIP Conference Proceedings*, 2018, **1971**, 030011.

18. S. Bolegenova, A. Askarova, N. Slavinskaya, S. Ospanova, A. Maxutkhanova, A. Aldiyarova and D. Yerbosynov, *Physical Sciences and Technology*, 2022, 69-82%V 69.

19. X. Xing, X. Niu, Y. Liu, C. Yang, S. Wang, Y. Li and X. Jing, *Polymer Degradation and Stability*, 2021, **186**, 109534.

20. Q. Wang, H. Song, S. Pan, N. Dong, X. Wang and S. Sun, *Scientific Reports*, 2020, **10**, 3626.

21. L.-N. Wu, Z.-Y. Tian, D. Wang, Z.-H. Zheng, K.-R. Jin, B.-Z. Liu, C. Xie, Q. Xu and Z.-D. Wang, *Combustion and Flame*, 2022, **245**, 112358.

22. J. Proano Aviles, J. Lindstrom, P. Johnston and R. Brown, *Modeling the early stages of cellulose pyrolysis*, 2016.

23. G. SriBala, D. C. Vargas, P. Kostetskyy, R. Van de Vijver, L. J. Broadbelt, G. B. Marin and K. M. Van Geem, *ACS Engineering Au*, 2022, **2**, 320-332.

24. J. Ma, H. Luo, Y. Li, Z. Liu, D. Li, C. Gai and W. Jiao, *Bioresource Technology*, 2019, **282**, 133-141.

25. D. W. Kohn, H. Clauberg and P. Chen, *Review of Scientific Instruments*, 1992, **63**, 4003-4005.

26. Q. Guan, K. N. Urness, T. K. Ormond, D. E. David, G. Barney Ellison and J. W. Daily, *International Reviews in Physical Chemistry*, 2014, **33**, 447-487.

27. M. V. Zagidullin, R. I. Kaiser, D. P. Porfiriev, I. P. Zavershinskiy, M. Ahmed, V. N. Azyazov and A. M. Mebel, *The Journal of Physical Chemistry A*, 2018, **122**, 8819-8827.

28. K. Shao, Y. Tian and J. Zhang, *International Journal of Mass Spectrometry*, 2021, **460**, 116476.

29. K. Shao, Y. Tian and J. Zhang, *The Journal of Physical Chemistry A*, 2022, **126**, 1085-1093.

30. K. Shao, J. Brunson, Y. Tian and J. Zhang, *International Journal of Mass Spectrometry*, 2022, **482**, 116933.

31. K. Shao, X. Liu and J. Zhang, *The Journal of Physical Chemistry A*, 2023.

32. K. Shao, X. Liu, P. J. Jones, G. Sun, M. Gomez, B. P. Riser and J. Zhang, *Physical Chemistry Chemical Physics*, 2021, **23**, 9804-9813.

33. K. Shao, G. Sun, M. Gomez, X. Liu and J. Zhang, *European Journal of Mass Spectrometry*, 2023, **29**, 88-96.

CHAPTER 2 Research Approaches

2.1 Experimental Setup

The thermal decomposition experiments were conducted using a home-made flash pyrolysis vacuum ultraviolet photoionization time-of-flight mass spectrometer (VUV-PI-TOFMS).[1-6] The design of the flash pyrolysis microreactor was similar to that reported by Chen and co-workers.[7] The design of the experimental setup was summarized in Scheme 2.1. The precursor was seeded in the carrier gas and introduced in the apparatus by bubbling helium carrier gas through the liquid precursor sample; the total backing pressure of the

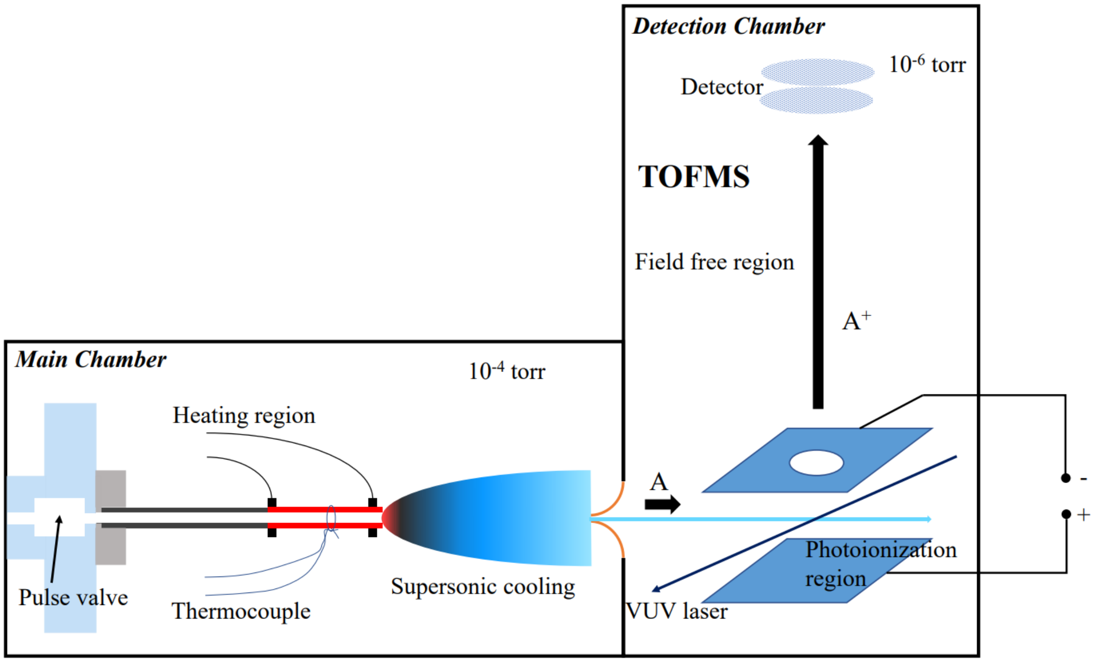

Scheme 2.1 Setup of the flash pyrolysis vacuum ultraviolet photoionization time-of-flight mass spectrometer (VUV-PI-TOFMS).

gas mixture was around 950 torr, while the precursor was diluted to ~ 1 % in the gas phase. The concentration of the precursor in the gas mixture was calculated based on the assumption that the vaporization and condensation of the precursor were in equilibrium over the liquid phase.

The gas mixture then expanded into a SiC microreactor (Carborundum, 2 mm o.d., 1 mm i.d.) after passing through a pulse valve (General Valve, Series 9). The pyrolysis of the precursor took place in the heated region (10 mm length) of the SiC microreactor which was heated resistively by electric currents that flowed through. The temperature was monitored by a type C thermocouple which was attached to the outside surface of the microreactor and was calibrated to the inside temperature of the microreactor. It is important to mention that the temperature of the mixture inside the microreactor has a non-uniform distribution both radially and axially due to the high flow rate and short residence time. A complete understanding of the flow would require extensive computational fluid dynamic calculations.[8] However, as the current study did not require a quantitative analysis

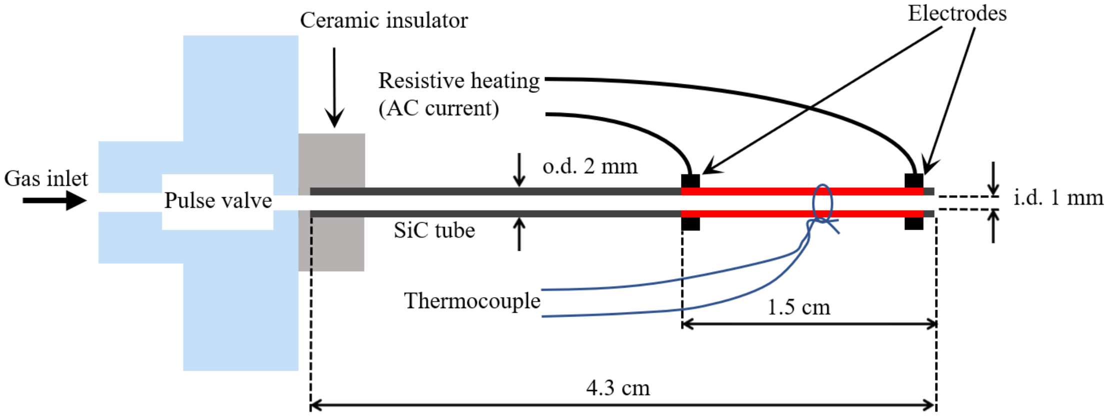

Scheme 2.2 Design of the microreactor.

of the relationship between mass signal and its corresponding temperature, the temperature utilized in this work was considered to be the same as the calibrated inside temperature, as described previously. The design of the microreactor is summarized in Scheme 2.2.

Likewise, there is also a non-uniform distribution of pressure both radially and axially. This estimation of the mass flow rate was based on the different vacuum reading in the reaction chamber with and without the pulsed flow. After including other parameters such as the gas throughput, pumping speed, and conductance of the different components, the flow rates of the gas mixture could be estimated; and according to Zagidullin et al., the average centerline pressure within the heated region in the microreactor could be estimated to be ~ 10 torr.[8] From there, the residence time within the heated region could also be estimated to be around 100 μs.[8, 9] From the simulation results, as well as the previous work, the reaction conditions within the microreactor were found to significantly favor unimolecular reactions, while bimolecular reactions and wall reactions were reduced.[6, 8-10]

After exiting the nozzle, the gas mixture, which contained the products, reactive intermediates, and unreacted reactants, supersonically expanded into the main chamber and then underwent free expansion, resulting in significant cooling to translational and rotational temperatures under 50 K due to collisions with the carrier gas.[11] Those has molecules entered a nearly collision-free environment referred to as the zone of silence until the density of the expanding gases approaches that of the background. At this point, a shock zone referred to as the Mach disk is formed, where the gas particles are rapidly decelerated by collisions with background gases. The Mach disk's location is given by an equation involving the distance of the Mach disk from the source exit and the nozzle diameter.[12] Chen and coworkers confirmed that the gas pulse duration and flow velocity from a 4 cm long extension tube (the microreactor) versus that of a bare pulsed valve are essentially identical above 1.0 atm stagnation pressure.[7]

After being selected by a skimmer, the isolated molecular beam was intercepted by 118 nm VUV radiation in the photoionization region. The 118 nm radiation was generated by tripling the 355 nm radiation from a Nd:YAG laser in a xenon cell (with ~18 torr of xenon). The reactive intermediates, products, and unreacted reactants in the molecular beam were photoionized. The ions produced in the ionization region were extracted into the linear TOF mass spectrometer. The ion signals were then detected and recorded using a digital oscilloscope (Tektronix TDS3032) after averaging over 512 laser shots at each SiC microreactor temperature. The TOF spectra were then converted to the mass spectra.

2.2 Theoretical Calculations.

Quantum chemistry calculations were performed in addition to the experimental studies to investigate the energetics of the competing reactions. The energetics of the reactants, products, and transition states involved in the precursor pyrolysis were calculated. Density functional theory (DFT) calculations for geometry optimizations and zero-point energies were performed at appropriate level of theory based on the nature of the precursors, as it was recommended by Sirianni et al.[13, 14] The single-point energy calculations were carried out based on a certain calculated structure.

For the selection of calculation method for geometry optimizations, it is important to carefully select the appropriate method to carry out the calculations. The choice of the

DFT method and corresponding basis sets can significantly impact the accuracy and efficiency of geometry optimizations for gas-phase organic molecules. When selecting a DFT method, one should consider its reliability in describing the electronic structure of the molecule, the computational cost, and the limitations of the chosen method. Generally, one should aim for a balance between accuracy and computational cost, with more accurate methods requiring higher computational costs. Similarly, the choice of basis sets must also find a balance between the accuracy and computational cost. Large basis sets do not necessarily provide better accuracy, and the choice of the basis sets must depend on specific molecules and intermolecular interactions. A common rule of thumb is to use a DFT method and basis set that provide the highest possible accuracy while maintaining an acceptable computational cost.

Some works reported in this thesis used a different computational method aimed for better computational accuracy, as high-level single-point energy calculations may achieve better accuracy with relatively affordable computational cost. For the zero-point energy calculations, all the zero-point vibrational frequencies were calculated at the same level of theory as the geometry optimization method, and were scaled by a factor as recommended in literature to account for overestimations in the vibrational frequency calculations.[15] Furthermore, all transition states were verified using IRC calculations at the same level of theory as the geometry optimization method. All computations in this work were performed using the Gaussian 16 package.[16]

2.3 Transition State Theory Calculations.

While theoretical calculations can provide reasonable explanations for the relative competitiveness of the competing reaction pathways, they have certain limitations when it comes to explain certain competing reaction channels. For instance, a bond-dissociation reaction and a concerted reaction with a tight transition state are difficult to compare from a pure thermodynamic point of view. These two reactions exhibit a significant disparity in their pre-exponential factor and temperature dependence from a kinetic standpoint, which could result in a substantial difference in the reaction rate constant despite the energy barriers being similar. As a result, kinetic factors must be taken into consideration, and (Variational) Transition State Theory calculations should be utilized.

In the pyrolysis study of trimethylchlorosilane and tetraethylsilane, unimolecular reaction rate constants of the initiation reactions were calculated using transition state theory (TST). For the unimolecular dissociation reaction with a conventional transition state, the rate constant was calculated using TST with Wigner tunneling correction.[17-20] The single point energy and frequencies of reactants and transition states were obtained from the DFT calculations at the corresponding level of theory used in their computational studies.[16] For the bond homolysis (barrierless) reactions, variational transition state theory (VTST) with Wigner tunneling correction was applied.[17-21] A series of constrained optimizations along the reaction path were carried out, and at each optimized geometry ("trial transition state"), the potential energy and vibrational frequencies were calculated. The dividing surface for the barrierless reactions at different temperatures were determined by finding the maximum Gibbs free energy change $\Delta G^{\ominus}(T)$ of the "trail transition state" along the reaction pathway at the different temperatures.[21] All the rate constant calculations were performed using the KISTHELP program.[19, 22, 23]

REFERENCE

1. S. D. Chambreau, J. Zhang, J. C. Traeger and T. H. Morton, *International Journal of Mass Spectrometry*, 2000, **199**, 17-27.

2. S. D. Chambreau and J. Zhang, *Chemical Physics Letters*, 2001, **343**, 482-488.

3. K. Shao, X. Liu, P. J. Jones, G. Sun, M. Gomez, B. P. Riser and J. Zhang, *Physical Chemistry Chemical Physics*, 2021, **23**, 9804-9813.

4. X. Liu, J. Zhang, A. Vazquez, D. Wang and S. Li, *Physical Chemistry Chemical Physics*, 2018, **20**, 18782-18789.

5. K. Shao, Y. Tian and J. Zhang, *International Journal of Mass Spectrometry*, 2021, **460**, 116476.

6. P. J. Jones, B. Riser and J. Zhang, *The Journal of Physical Chemistry A*, 2017, **121**, 7846-7853.

7. D. W. Kohn, H. Clauberg and P. Chen, *Review of Scientific Instruments*, 1992, **63**, 4003-4005.

8. M. V. Zagidullin, R. I. Kaiser, D. P. Porfiriev, I. P. Zavershinskiy, M. Ahmed, V. N. Azyazov and A. M. Mebel, *The Journal of Physical Chemistry A*, 2018, **122**, 8819-8827.

9. Q. Guan, K. N. Urness, T. K. Ormond, D. E. David, G. Barney Ellison and J. W. Daily, *International Reviews in Physical Chemistry*, 2014, **33**, 447-487.

10. K. Shao, Y. Tian and J. Zhang, *The Journal of Physical Chemistry A*, 2022, **126**, 1085-1093.

11. G. Scoles, D. R. Miller, W. Gentry, H. Pauly, D. Bassi, U.Hefter, K. Bergman, M. Zen, J. Reuss, C. J. N. Meijdenberg, D. Abuerbach, M. Kappes, S. Leutwyler, U. Valbusa, U. Buck, Y. T. Lee, P. Dagdigian, S. Stolte, R. Düren and S. Iannotta, *Atomic and Molecular Beam Methods: Vol. 1*, 1998.

12. M. D. Morse, *Experimental Methods in The Physical Sciences*, 1996, **29**, 21-47.

13. M. Cypryk and B. Gostyński, *Journal of molecular modeling*, 2016, **22**, 35.

14. D. A. Sirianni, A. Alenaizan, D. L. Cheney and C. D. Sherrill, *Journal of Chemical Theory and Computation*, 2018, **14**, 3004-3013.

15. M. L. Laury, S. E. Boesch, I. Haken, P. Sinha, R. A. Wheeler and A. K. Wilson, *Journal of computational chemistry*, 2011, **32**, 2339-2347.

16. M. J. Frisch, G. W. Trucks, H. B. Schlegel, G. E. Scuseria, M. A. Robb, J. R. Cheeseman, G. Scalmani, V. Barone, G. A. Petersson, H. Nakatsuji, X. Li, M. Caricato, A. V. Marenich, J. Bloino, B. G. Janesko, R. Gomperts, B. Mennucci, H. P. Hratchian, J. V. Ortiz, A. F. Izmaylov, J. L. Sonnenberg, Williams, F. Ding, F. Lipparini, F. Egidi, J. Goings, B. Peng, A. Petrone, T. Henderson, D. Ranasinghe, V. G. Zakrzewski, J. Gao, N. Rega, G. Zheng, W. Liang, M. Hada, M. Ehara, K. Toyota, R. Fukuda, J. Hasegawa, M. Ishida, T. Nakajima, Y. Honda, O. Kitao, H. Nakai, T. Vreven, K. Throssell, J. A. Montgomery Jr., J. E. Peralta, F. Ogliaro, M. J. Bearpark, J. J. Heyd, E. N. Brothers, K. N. Kudin, V. N. Staroverov, T. A. Keith, R. Kobayashi, J. Normand, K. Raghavachari, A. P. Rendell, J. C. Burant, S. S. Iyengar, J. Tomasi, M. Cossi, J. M. Millam, M. Klene, C. Adamo, R. Cammi, J. W. Ochterski, R. L. Martin, K. Morokuma, O. Farkas, J. B. Foresman and D. J. Fox, *Gaussian 16 Rev. C.01*, (2016), Wallingford, CT.

17. D. G. Truhlar, B. C. Garrett and S. J. Klippenstein, *The Journal of Physical Chemistry*, 1996, **100**, 12771-12800.

18. E. Wigner, *Transactions of the Faraday Society*, 1938, **34**, 29-41.

19. S. Canneaux, F. Bohr and E. Henon, *Journal of computational chemistry*, 2014, **35**, 82-93.

20. A. W. Jasper, J. A. Miller and S. J. Klippenstein, *The Journal of Physical Chemistry A*, 2013, **117**, 12243-12255.

21. M. A. Ali, *Scientific Reports*, 2020, **10**, 10995.

22. S. Mohandas, R. O. Ramabhadran and S. S. Kumar, *The Journal of Physical Chemistry A*, 2020, **124**, 8373-8382.

23. S. Begum and R. Subramanian, *RSC Advances*, 2015, **5**, 39110-39121.

CHAPTER 3 Thermal decomposition mechanism of allyltrichlorosilane and allyltrimethylsilane

3.1 Introduction

SiC thin film has wide applications in material science and electronic engineering for its remarkable physical and chemical properties such as high thermal conductivity, exceptional hardness and high chemical inertness.[1, 2] Organosilicon compounds are commonly used as precursors in chemical vapor deposition (CVD) of SiC film. The gas phase pyrolysis studies of organosilicon precursors are useful for understanding SiC film productions.[3-5] As a potential precursor, a number of studies on the pyrolysis of allyltrimethylsilane have been carried out over the past several decades. In 1969, Bailey and Kaufmann first reported the retro-ene reaction (3.1) forming $Me_2Si{=}CH_2$ and C_3H_6 and that $Me_2Si{=}CH_2$ further reacted to form a silene dimer (reaction (3.2)).[6] Sakurai et al.[7] did the pyrolysis experiment at 500°C in a nitrogen steam environment, but failed to observe reaction (3.2) and instead considered $Me_2Si{=}CH_2$, $HSiMe_3$, and vinyltrimethylsilane as the major products of allyltrimethylsilane decomposition (reaction (3.3), (3.4) and (3.5)). They postulated the homolysis of Si-C bond (reaction (3.3)) producing trimethylsilyl radical ($Me_3Si\bullet$) and allyl radical ($\bullet C_3H_5$) as one of the initiation channels.

$$Me_3SiCH_2CH{=}CH_2 \rightarrow Me_2Si{=}CH_2 + C_3H_6 \tag{3.1}$$

$2Me_2Si{=}CH_2 \rightarrow$

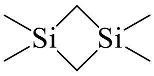

(3.2)

$$Me_3SiCH_2CH{=}CH_2 \rightarrow Me_3Si\bullet + \bullet C_3H_5 \tag{3.3}$$

$$2Me_3Si\bullet \rightarrow Me_2Si{=}CH_2 + HSiMe_3 \tag{3.4}$$

$$Me_3SiCH_2CH{=}CH_2 \xrightarrow{\text{3-member ring TS}} Me_3SiCH{=}CH_2 + :CH_2 \tag{3.5}$$

$$Me_3SiCH_2CH{=}CH_2 \rightarrow Me_2\dot{S}iCH_2CH{=}CH_2 + \bullet CH_3 \tag{3.6}$$

$$Me_2\dot{S}iCH_2CH{=}CH_2 \xrightarrow{\text{rearrangement}} Me_2\dot{C}H_2SiCH{=}CH_2 \tag{3.7}$$

$$Me_2\dot{C}H_2SiCH{=}CH_2 + \bullet H \xrightarrow{\text{H addition}} Me_3SiCH{=}CH_2 \tag{3.8}$$

$$Me_3Si\bullet \rightarrow Me_2Si{=}CH_2 + \bullet H \tag{3.9}$$

As for the formation mechanism of vinyltrimethylsilane, Sakurai et al.[7] believed that reaction (3.5) proceeded via a three-member carbon ring transition state leading to the vinyltrimethylsilane and carbene products. This mechanism was later challenged by Neider et al.[8], who examined the pyrolysis of allyltris(trideuteriomethyl)silane ($(CD_3)_3SiCH_2CH{=}CH_2$). They claimed that vinyltrimethylsilane was formed from a rearrangement of $Me_2\dot{S}iCH_2CH{=}CH_2$, which was produced from •CH_3 loss from the parent molecule (reaction (3.6), (3.7) and (3.8)). Davidson in 1980 argued that reactions (5)-(8) were not primary pyrolytic steps and the primary reaction was initiated by rupture of the Si-C (allyl) bond (reaction (3.3)), and the production of vinyltrimethylsilane was a bimolecular process.[9] Later, in 1984, Wood and co-workers investigated the decomposition of allyltrimethylsilane using low-pressure pyrolysis (LPP) technique, and proposed that reaction (3.3) was an important initiation pathway in the allyltrimethylsilane pyrolysis and confirmed the formation of trimethylsilyl radical by trapping it with CH_3Cl forming

Me_3SiCl.[10] In 1988, they further demonstrated that formation of vinyltrimethylsilane was strongly pressure dependent.[11]

In the above studies, the main thermolysis initiation steps were not clear due to the relatively long reaction time utilized (on the order of seconds). Also, direct observation of labile radicals and initial reactive intermediates (such as $Me_3Si\bullet$ and $\bullet C_3H_5$) were not presented. Recent work on the pyrolysis of tetramethylsilane reported by Zhang and co-workers[12,13] revealed that the trimethylsilyl radical could decompose via a H• loss channel to form $Me_2Si{=}CH_2$ (reaction (3.9)), and this channel, together with reaction (3.3), could compete with reaction (3.1). This work indicated that without the direct detection of radicals involved (such as $Me_3Si\bullet$ and $\bullet C_3H_5$), the mechanism of the primary reactions is still unclear, and more information of the competing initiation channels is needed. These facts motivate us to reconsider the initiation steps in the allyltrimethylsilane thermal decomposition.

At the same time, because of the complexity of the secondary reactions of the allyl radical in the allyltrimethylsilane pyrolysis,[14] it is helpful to isolate the $\bullet C_3H_5$ chemistry and clarify the reaction behavior of the allyl radical. For this purpose, allyltrichlorosilane is selected as an analog to allyltrimethylsilane and to separate the chemistry of the allyl and the Si-containing component. Since the typical bond dissociation energy of the Si-C bond (76.3 kcal/mol) is smaller than that of the Si-Cl bond (91.1 kcal/mol), the major decomposition products of allyltrichlorosilane are believed to be the allyl radical and trichlorosilyl radical ($\bullet SiCl_3$) (reaction (3.10)).

$$C_3H_5SiCl_3 \rightarrow \bullet C_3H_5 + \bullet SiCl_3 \tag{3.10}$$

$$C_3H_5SiCl_3 \rightarrow \bullet C_3H_5 + \bullet SiCl_3 \rightarrow \bullet C_3H_5 + :SiCl_2 + \bullet Cl \tag{3.11}$$

$$C_3H_5SiCl_3 \overset{TS}{\rightarrow} C_3H_5Cl + :SiCl_2 \rightarrow \bullet C_3H_5 + :SiCl_2 + \bullet Cl \tag{3.12}$$

$$C_3H_5SiCl_3 \rightarrow \bullet Cl + C_3H_5\dot{S}iCl_2 \rightarrow \bullet C_3H_5 + :SiCl_2 + \bullet Cl \tag{3.13}$$

Boganov et al. studied the pyrolysis of allyltrichlorosilane using matrix isolation coupled with infrared (IR) spectroscopy under 10^{-2} Torr and found $\bullet C_3H_5$, $:SiCl_2$, and Cl• as three major products.[15] They proposed three possible reactions pathways that led to those three products (reaction (3.11)-(3.13)), and considered that reaction (3.11) was the main decomposition pathway.[15] In their conclusions, thermal decompositions of the allyl radical and trichlorosilyl radical were independent from each other, which could provide with information on the isolation of $\bullet C_3H_5$ chemistry when compared with the allyltrimethylsilane pyrolysis.

Based on these motivations, thermal decomposition of allyltrimethylsilane and allyltrichlorosilane were performed in this chapter using flash pyrolysis coupled with vacuum ultraviolet single-photon ionization time-of-flight mass spectrometry (VUV-SPI-TOFMS).[12, 13] This experimental approach could provide with pyrolysis mass spectra of the products, intermediates and unreacted reactants from a short residence time (~ 100 µs) in the reaction zone. It allows direct detection of initial reactive intermediates and products for a better characterization of the *initial* thermal dissociation mechanisms. Quantum chemistry calculations were also employed to characterize the organosilicon species involved in this chapter, including the geometries and energies of reactants, transition states, reactive intermediates, and products.

3.2 Experimental and computational method

Allyltrimethylsilane (98%+) was obtained from Alfa Aesar, and allyltrichlorosilane (95%) was purchased from Sigma Aldrich. The liquid sample was placed in a glass bubbler immersed in a cold temperature bath and the sample vapor was diluted to ~ 1% in helium carrier gas. The density functional theory method was employed to carry out quantum chemistry calculation in this chapter. The geometries and single-point energies of the different species involved were calculated at the UB3LYP/6-311++g(d,p) level. Frequency calculations and zero-point-energy (ZPE) correction were made for each geometry at the same level of theory. Transition states were justified using intrinsic reaction coordinate (IRC) calculations. The energy barrier in this chapter was defined as the difference of the ZPE corrected electronic energies between geometries of interest at 0 K. All computational works were performed using the Gaussian 09 program.[16]

3.3 Results and discussions

(a) Pyrolysis of allyltrichlorosilane

The pyrolysis of allyltrichlorosilane was performed in the temperature range from 295 K to 1330 K. The pyrolysis mass spectra are shown in Figure 3.1 and 3.2. At room temperature (295 K), peaks at m/z = 174, 176, 178, and 180 were the parent peaks (with ^{35}Cl and ^{37}Cl). As the isotope natural abundance of ^{35}Cl and ^{37}Cl is 75.8:24.2, a combination of 3 Cl atoms gives rise to an intensity ratio of ~ 27:27:9:1 for the m/z = 174, 176, 178, and 180 peaks. The Si atom has an isotope natural abundance of ^{28}Si: ^{29}Si: ^{30}Si = 92.2: 4.7: 3.1.[17] Since the contributions of ^{29}Si and ^{30}Si are small, mainly the isotopes of the chlorine

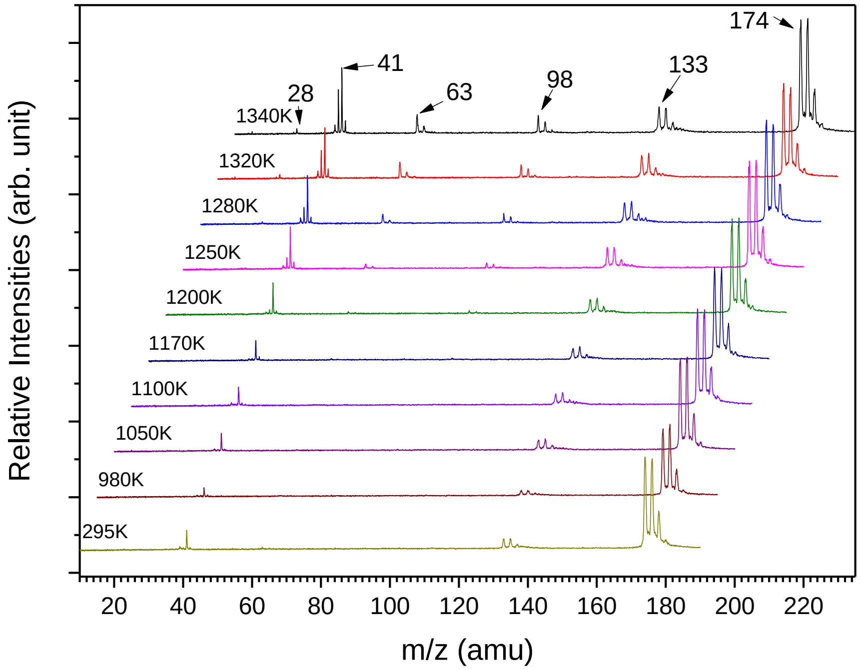

Figure 3.1 Mass spectra of the pyrolysis of allyltrichlorosilane (1% in He) at 295–1330K. The mass spectra are offset for clarity.

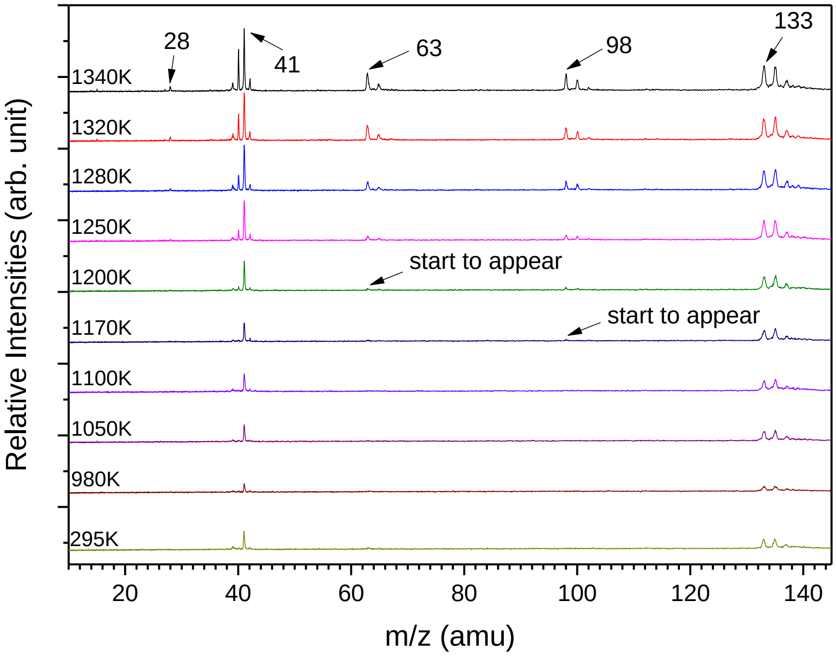

Figure 3.2 Mass spectra of the pyrolysis of allyltrichlorosilane (1% in He) at 295-1330K, with enlarged regions for the products.

atom are considered here. At 295 K, mass peak of m/z = 133, as well as its isotope peaks m/z = 135 and 137, corresponded to the $SiCl_3^+$ ion fragment from photoionization fragmentation of the parent molecule. They had a peak intensity ratio of ~ 27:27:9 that satisfied the isotope abundance of ^{35}Cl and ^{37}Cl (the m/z = 139 peak intensity was too low). At 295 K, m/z = 41, which corresponded to the $C_3H_5^+$ ion signal, was also caused by parent photoionization fragmentation.

As the temperature increased (above 980 K), the set of peaks at m/z = 133, 135 and 137 (with a ratio of ~ 3:3:1) increased above the photoionization fragmentation intensities at the room temperature, indicating production of neutral •$SiCl_3$ from thermal decomposition of allyltrichlorosilane (reaction (3.10)) and its photoionization. In order to characterize the onset of reaction (3.10), the peak area ratio of m/z = 133 (•$SiCl_3$ with ^{35}Cl) versus m/z = 174 (the parent molecule with ^{35}Cl) was obtained from the pyrolysis mass spectra and plotted as a function of temperature in Figure 3.3. The peak area ratio could be expressed by the formula in Equation (3.1). The increase of the ratio as a function of the pyrolysis temperature indicates thermal decomposition reactions. The expression is derived with the assumption that photoionization fragmentation of species cooled in the molecular beam is largely independent of the pyrolysis temperature, giving rise to a constant baseline of the peak area ratio curve, while the increase of the curve is an indication of thermal decomposition of the parent molecule. The detailed derivations could be found in the

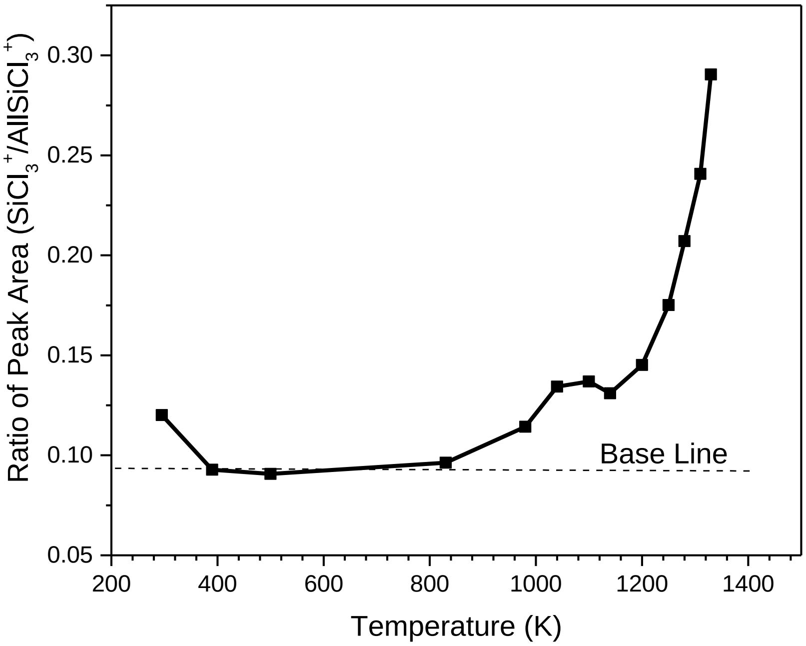

Figure 3.3 Ratio of peak area of m/z = 133 (trichlorosilyl) versus m/z = 174 (allyltrichlorosilane). The trend shows that the Si-C bond breaking (reaction (3.10)) was initiated at around 980 K.

$$\frac{S_{p_{ij}^{+}}(T)}{S_{R^{+}}(T)} = D \cdot X(T') \cdot \alpha_i(T) + D \cdot Y(T')$$

Equation 3.1 General expression for the ratio between peak area of the fragment peak ($S_{p_{ij}^{+}}(T)$, p_{ij} represents the *j-th* product in the *i-th* reaction channel) and peak area of the parent peak ($S_{R^{+}}(T)$). D is a constant for detection efficiency, $X(T')$ and $Y(T')$ are constants that depend on molecular beam temperature T' and are assumed to be largely independent of the pyrolysis temperature T, and $\alpha_i(T)$ is the thermal dissociation fraction of the *i-th* channel at temperature T.

Supplementary Materials. Figure 3.3 shows that at temperatures below 980 K, the m/z = 133 to 174 peak area ratio was nearly constant (supporting the assumption in Equation (3.1)). Note that the ratio at 295 K is slightly higher than the baseline, possibly caused by contribution from the parent molecule clusters in the beam. When the temperature reached to ~ 980 K, the ratio started to increase, indicating that the m/z = 133 signal was composed of not only photoionization fragmentation of the parent molecules, but also thermal decomposition of the parent molecule that started to take place. Although the •$SiCl_3$ radical was postulated as the initial reactive intermediate in the thermal decomposition of allyltrichlorosilane (reaction (3.11)) by Boganov et al.,[15] it was not directly observed in their matrix isolation IR spectroscopy experiment. This current work provides the first direct evidence and observation of this initial reactive intermediate from allyltrichlorosilane.

The m/z = 98 peak and its isotope peaks m/z = 100 and 102 were from $:SiCl_2$ with a relative intensity of ~ 9:6:1, and the m/z = 98 peak was chosen to represent the $:SiCl_2$ signals. At room temperature (298 K), the m/z = 98 peak was not observed. When the temperature increased, it started to appear at 1170 K. C_3H_5Cl (m/z = 76), the possible counterpart of $:SiCl_2$ in the elimination channel (reaction (3.12)) of allyltrichlorosilane, was not observed in this chapter, although C_3H_5Cl is detectable by the 10.5 eV photoionization radiation (the ionization potential of C_3H_5Cl is 10.05 eV[18]). This implied that reaction (3.12) was not significant and not a source of $:SiCl_2$. On the other hand, since the homolysis of Si-C bond (reaction (3.10)) was believed to take place at 980 K, the

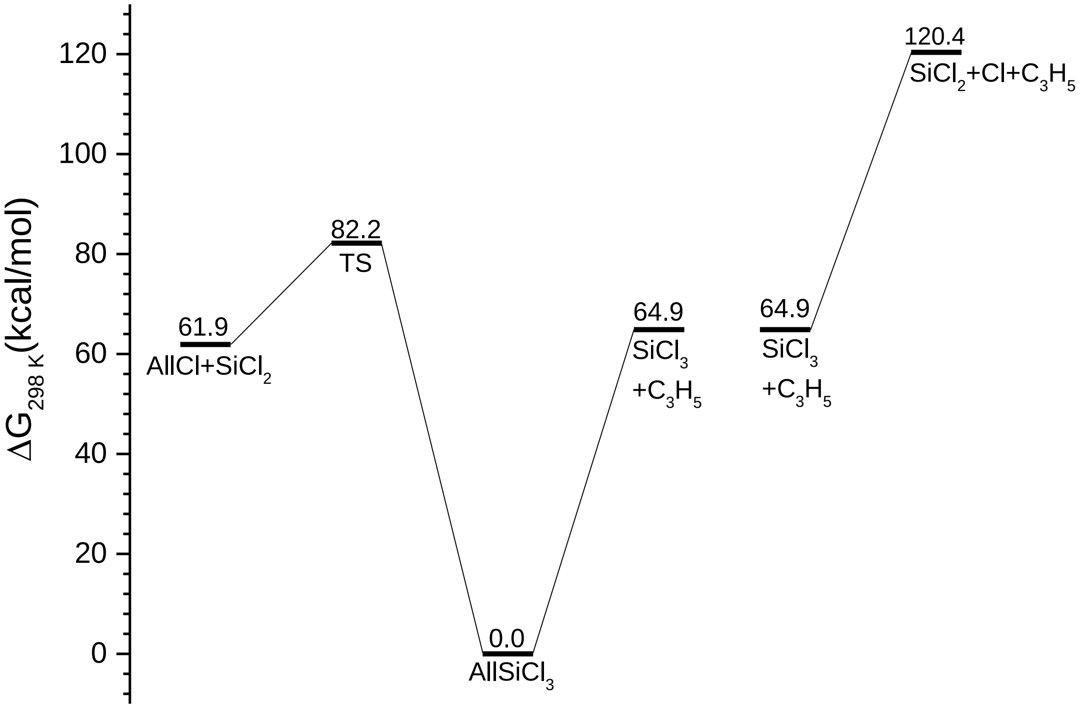

Figure 3.4 Gibbs free energy with zero-point energy correction of species during the pyrolysis of allyltrichlorosilane at 298 K at the G4(MP2) level of theory reported by Boganov et al.[15]

secondary dissociation of •$SiCl_3$ (reaction (3.14)) started to take place at higher temperatures (such as 1170 K), and the signal of m/z = 98 peak was attributed to :$SiCl_2$ by reaction (3.14). This observation was consistent with the conclusions by Boganov et al.[15] According to their calculations at the G4 (MP2) level of theory (as shown in Figure 3.4), the elimination channel forming :$SiCl_2$ + C_3H_5Cl (reaction (3.12)) need to overcome an 82.2 kcal/mol energy barrier, while that for the Si-C bond breaking (reaction (3.10)) is only 64.9 kcal/mol and therefore preferred. Note that Cl atom was the co-product of :$SiCl_2$ in reaction (3.14); however, since the ionization potential of chlorine atom is 12.97 eV,[19] it was not detected in the mass spectra in this chapter.

$$\bullet SiCl_3 \rightarrow :SiCl_2 + \bullet Cl \tag{3.14}$$

The intensity of m/z = 63 and 65 peaks had a ratio of 3:1, and they represented $Si^{35}Cl$ and $Si^{37}Cl$. As shown in Figure 3.2, the m/z = 63 and 65 peaks appeared at 1200 K and further increased as the temperature increased. As the :$SiCl_2$ peak (m/z = 98, 100, and 102) was first observed at 1170 K, it is reasonable to consider that SiCl was produced at higher temperatures via sequential Cl loss from :$SiCl_2$ (reaction (3.15)).

$$:SiCl_2 \rightarrow SiCl + Cl \tag{3.15}$$

At the higher temperature of 1320 K, the mass peak m/z = 28 appeared. This could be attributed to further decomposition of SiCl to Si and Cl, following reaction (3.15). The signal of Si (m/z = 28) was very weak, and the isotopic peak m/z = 29 and m/z = 30 could not be detected. Alternatively, the m/z = 28 peak could be attributed to C_2H_4, produced from secondary reactions of the allyl radical. However, the ionization potential of C_2H_4 (10.51 eV)[20] is slightly above the photon energy in this chapter (10.5 eV), suggesting that the detection of C_2H_4 was less likely.

The mass peak at m/z = 41 was due to the allyl radical $\bullet C_3H_5$, and m/z = 39, 40 and 42 corresponded to C_3H_3, C_3H_4, and C_3H_6. As shown in Figure 3.2, at room temperature the m/z = 41 peak was a photoionization fragment of the parent molecule. The m/z = 41 peak started to grow above ~ 1000 K and increased further when the temperature increased. This agrees with the observation of its co-product $\bullet SiCl_3$ at the onset temperature of ~ 980 K and supports reaction (3.10) as the primary initiation process. With further increase of the temperature, other peaks such as m/z = 39, 40, 42 started to show up, which suggested that secondary reactions of the allyl radical also took place. The mechanism of allyl radical dissociation has been investigated previously.[14, 21-23] It has been accepted that $\bullet C_3H_5$ undergoes H elimination and the main products are allene (m/z = 40) + H (reaction (3.16a)) or propyne (m/z = 40) + H (reaction (3.16b)). As the temperature increased, further H elimination reactions were observed. According to the calculations reported by Narendrapurapu et al,[14] propargyl (m/z = 39) was produced predominately by H-elimination from allene. These were consistent with the mass spectra in Figure 3.2, where m/z = 40 first appeared at 1200 K, and m/z = 39 was then recorded at 1250 K. A very minor mass peak at m/z = 15 started to appear at 1320 K. The methyl radical could be produced by $\bullet CH_3$ elimination following isomerization of allyl to 1-propenyl (CH_3CHCH) (reaction (3.17)). The small mass peak of m/z = 42 at high temperatures suggested a minor secondary reaction in which H combined with an allyl radical (reaction (3.18)). The mass peak of m/z = 42 did not appear until the temperature reached 1250 K; therefore, at the temperatures below 1250 K, the secondary reaction of allyl radical (•C_3H_5) producing C_3H_6 was insignificant.

$$\bullet C_3H_5\ (\text{allyl}) \xrightarrow{-H} CH_2{=}C{=}CH_2 \xrightarrow{-H} C_3H_3 \tag{3.16a}$$

$$\bullet C_3H_5\ (\text{allyl}) \xrightarrow{-H} CH_3C{\equiv}CH \xrightarrow{-H} C_3H_3 \tag{3.16b}$$

$$\bullet C_3H_5\ (\text{allyl}) \xrightarrow{\text{isomerization}} CH_3CH{=}CH\bullet \rightarrow \bullet CH_3 + HCCH \tag{3.17}$$

$$\bullet C_3H_5\ (\text{allyl}) + H \rightarrow CH_3CH{=}CH_2 \tag{3.18}$$

(b) Pyrolysis of allyltrimethylsilane

The thermal decomposition of allyltrimethylsilane was carried out at temperatures from 295 K to 1360 K. The pyrolysis mass spectra are displayed in Figure 3.5 and 3.6. The mass peaks at room temperature corresponded to the photoionization fragmentation background. The growths of these peaks at the elevated temperatures would indicate the production of neutral species from thermal decomposition. As shown in Figure 3.5, m/z = 114, 115 and 116 corresponded to the allyltrimethylsilane parent peaks with ^{28}Si, ^{29}Si and ^{30}Si, respectively. The mass peaks at m/z = 73, 74 and 75 represented $Me_3{}^{28}Si\bullet$ and its isotope peaks $Me_3{}^{29}Si\bullet$ and $Me_3{}^{30}Si\bullet$. The m/z = 99 peak corresponded to $Me_2\dot{S}iCH_2CH{=}CH_2$. The signals of m/z = 40, 41 and 42 corresponded to C_3H_4, C_3H_5 and C_3H_6.

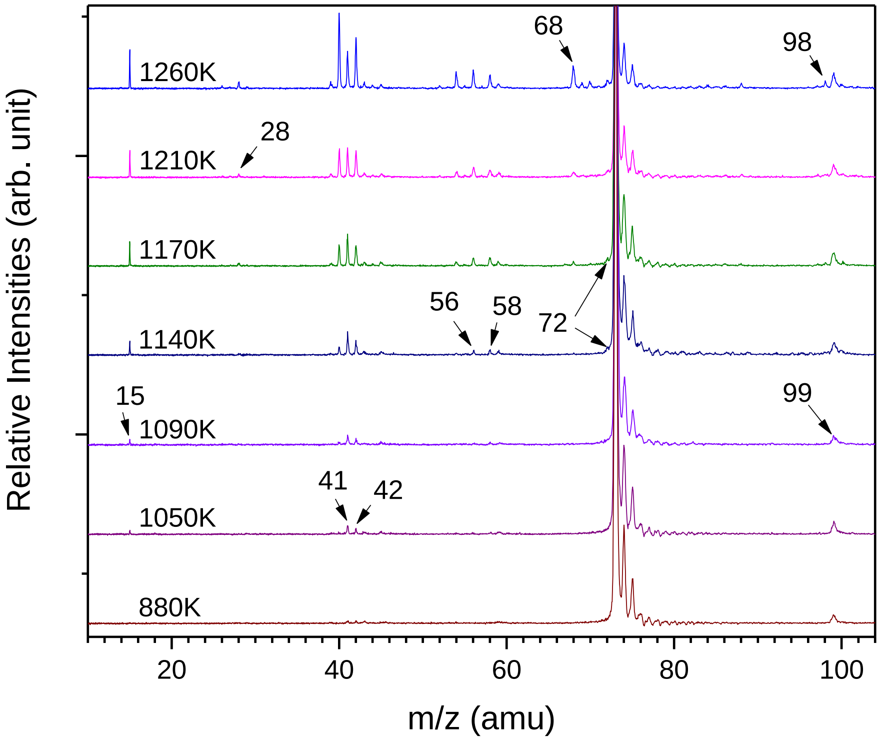

Figure 3.6 Mass spectra of the pyrolysis of allyltrimethylsilane (1% in He) at 880–1260 K, with enlarged regions to show the initiation steps and product masses. The spectra are offset for clarity.

As shown in Figure 3.5 and 3.6, both m/z = 41 and 42 peaks appeared at around 1050 K. The appearance of m/z = 41 peak indicated the Si-C homolytic reaction (3.3), and it will be discussed in the following section. The peak area ratio of m/z = 42 vs 114 is plotted in Figure 3.7 and implied that reaction (3.1) started to take place at around 1050 K. This observation was in contrast with what was observed in the allyltrichlorosilane pyrolysis, where the m/z = 41 peak started to be produced at around 980 K while the m/z = 42 peak was not observed until at much higher temperature (~ 1250 K) as a secondary product of the allyl radical. This difference indicated that the production of C_3H_6 (m/z = 42) from allyltrimethylsilane near the onset temperature of ~ 1050 K followed a different formation mechanism. Unlike in the thermal decomposition of allyltrichlorosilane where the C_3H_6 (m/z = 42) peak was produced via the secondary H-addition reaction (reaction (3.18)) at high temperatures, the early production of the m/z = 42 peak (C_3H_6) in the allyltrimethylsilane pyrolysis at ~ 1050 K proceeded via a direct, primary initiation reaction, consistent with the molecular elimination reaction (3.1). This mechanism was also supported by the growth trend and significant intensity of the m/z = 42 peak at temperatures

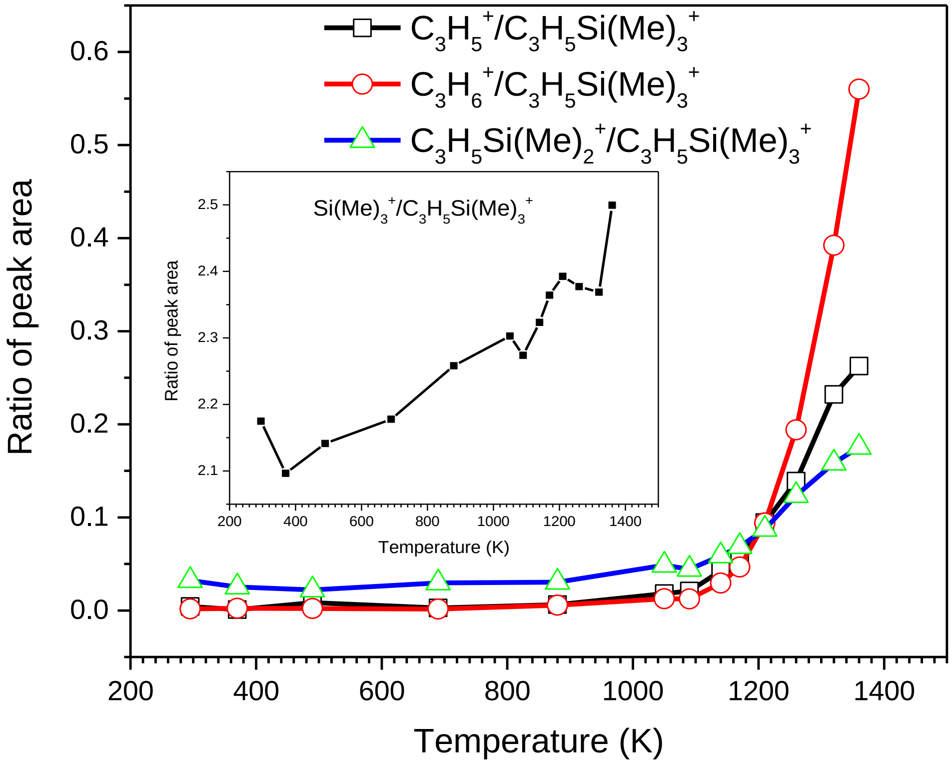

Figure 3.7 Peak area ratios of m/z = 41, 42 and 99 versus m/z =114 (allyltrimethylsilane). The reaction (3.1), (3.3) and (3.6) were initiated around 1100 K. The inserted figure is the peak area ratio of trimethylsilyl versus allyltrimethylsilane.

> 1140 K, which were different and much higher than in the allyltrichlorosilane pyrolysis. At higher temperatures, there might be a minor contribution to m/z = 42 from $:Si=CH_2$, as a secondary product of $\bullet SiMe_3$ and $:SiMe_2$ (as discussed in Section 3). However, the previous study indicated that this contribution was negligible below ~ 1200 K and insignificant at ~ 1280 K.[13]

In addition, as the co-product of C_3H_6 in reaction (3.1), m/z = 72 ($Me_2Si=CH_2$) was identified. In Figure 3.6, m/z = 72 peak started to appear at 1140 K. It was not simultaneously captured with the m/z = 42 peak at ~ 1050 K, possibly due to the fact that the intensity of m/z = 72 peak was relatively low and it was located next to the shoulder of the intense m/z = 73 peak, which overwhelmed the weak m/z = 72 peak. This was consistent with the previous studies showing that it was difficult to trace the m/z = 72 peak.[13] The consideration of reaction (3.1) as a primary initiation reaction was also supported by quantum chemistry calculations (Figure 3.8). The reaction (3.1) has the lowest energy barrier of 55.9 kcal/mol (via TS2) and is therefore kinetically favored. Therefore, the reaction (3.1), which was initiated at around 1050 K, was considered as the major contributor of the m/z = 72 peak. Another possible source of the mass peak m/z = 72 could be H-loss secondary decomposition of the trimethylsilyl radical (reaction (3.9)), following the Si-C bond fission (reaction (3.3)) of the parent molecule. The reaction (3.3) has a 64.3 kcal/mol energy threshold, and as discussed in the following, it could be significant at higher temperatures. Furthermore, our previous studies have shown that H loss from trimethylsilyl forming $Me_2Si=CH_2$ (m/z = 72) is possible.[13]

The mass peak m/z = 41 (•C_3H_5), was first detected at ~ 1050 K, and the intensity increased as the temperature increased. This trend was revealed in the peak area ratio depicted in Figure 3.7. It showed that the peak area ratio of m/z = 41 vs. m/z = 114 started to increase at around 1050 K. Based on the discussion from the previous section, C_3H_6 was also produced at around 1050 K. However, it was unlikely for •C_3H_5 to be produced from secondary dissociation of propene C_3H_6 via a H atom loss at that temperature, as the energy required to break a C-H bond in propene is ~ 86.8 kcal/mol[24] (consistent with the value of

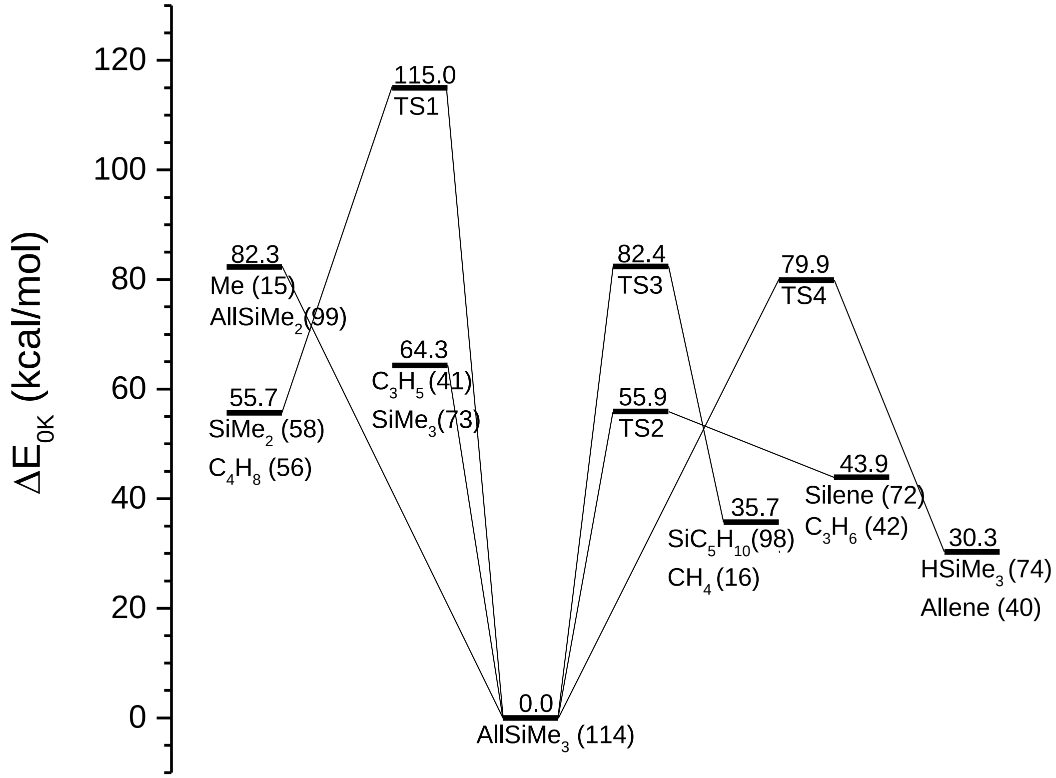

Figure 3.8 Potential energy diagram of pyrolysis pathways of allyltrimethyisilane. The geometry optimization and the energy (0 K) of each species were performed at UB3LYP/6-311++G(d,p) level, with ZPE correction. The mass to charge ratio (m/z) of some species were shown in the brackets. More information is provided in the Supplementary Materials.

82.6 kcal/mol (at 0 K) in our calculation), which is almost 20 kcal/mol higher than the energy required for reaction (3.3). Hence, C_3H_5 was produced via reaction (3.3) as a primary dissociation channel, instead of via secondary reactions of C_3H_6 from reaction (3.1), and the increase of peak intensity of m/z = 41 was mostly due to reaction (3.3).

It is also important to discuss the counterpart of •C_3H_5 in reaction (3.3), Me_3Si• (m/z =73). As shown in Figure 3.5 and 3.6, since the m/z = 73 peak was overwhelmed by the parent ion fragmentation, the ratio of peak areas was hence inspected. The inset in Figure 3.7 shows that the ratio of peak areas of Me_3Si• against the parent $C_3H_5SiMe_3$. It indicated that as temperature increased, the relative intensity of Me_3Si• over $C_3H_5SiMe_3$ increased. This ratio started a sharp increase at ~ 1100 K, implying the onset of thermal decompostion. However, unlike in other peak area ratio curves, the baseline prior to the sharp rise was not constant. The possible reason was that the photoionization fragmentation contribution $Y(T')$ (see Equation (3.1)) was relatively large, and its change with the temperature change ($\Delta T'$) within the molecular beam could not be omitted. Nevertheless, it is resonable to consider that reaction (3.3) contributed to the production of m/z = 73 because the trend in the ratio of peak areas increased with the increasing temperatures, with the onset of this reaction being around 1100 K. Therefore, as a competing reaction with reaction (3.1), reaction (3.3) also took place.

The m/z = 40 peak was first observed at ~ 1090 K, as shown in Figure 3.6, and it increased as the temperature increased and became higher than the m/z = 41 peak above 1210 K. Near the onset temperature of 1090 K, the m/z = 40 peak was not likely produced from secondary reactions of the allyl radical or propene which started to be produced at

~1050 K. Figure 3.2 shows that in the allyltrichlorosilane pyrolysis, in which m/z = 40 peak could only be produced from secondary decomposition of the allyl radical, the m/z = 40 peak was not observed until the temperature reached around 1200 K, and in addition it stayed in a lower intensity than the m/z = 41 peak when the temperature further increased. These comparisons suggested that in allyltrimethylsilane the appearance of the m/z = 40 peak near the onset temperature of 1090 K was not due to secondary dissociation of the allyl radical (although it could contribute to m/z = 40 at higher temperatures) and was from a different pathway. According to the energetics displayed in Figure 3.8, the direct dissociation reaction from allyltrimethylsilane to form $CH_2=C=CH_2$ (m/z = 40) and $HSiMe_3$ (reaction (3.19)) would require a 79.9 kcal/mol threshold energy, which suggested that reaction (3.19) could be competitive in the m/z = 40 formation.

$$Me_3SiCH_2CH=CH_2 \rightarrow HSiMe_3 + CH_2=C=CH_2 \tag{3.19}$$

Since the signal of the co-product $HSiMe_3$ (m/z = 74) overlapped with one of the isotope peaks of the major fragment $Me_3Si\bullet$, it was difficult to establish the ratio of peak areas from the mass spectra. However, there could be other indirect evidence (in addition to the m/z 40 peak) for the formation of $HSiMe_3$ via reaction (3.19). The production of $HSiMe_3$ could be suggested by the appearance of m/z = 59 peak which was first observed at 1140 K. Previous study has shown that $HSiMe_2$ (m/z = 59) was a major thermal decomposition product of $HSiMe_3$.[25] At 1140 K, the m/z = 59 peak was observed simultaneously with the m/z = 40 peak (C_3H_4, the co-product of $HSiMe_3$ in reaction (3.19)), possibly as a secondary decomposition product of $HSiMe_3$. Meanwhile, the formation of m/z = 59 could not be readily explained by any other sources; for example, as discussed later in Section 3 and 4, secondary decomposition of the main primary products, $Me_2Si=CH_2$, $Me_3Si•$, and $Me_2\dot{S}iCH_2CH=CH_2$, did not lead to a product at m/z = 59.[13] It is therefore plausible that $HSiMe_3$ was produced via the C_3H_4 elimination reaction from allyltrimethylsilane (reaction (3.19)), based on the computational calculations and the indirect suggestions, and the onset temperature was around or above 1090 K.

Since the m/z = 99 peak could be produced by photoionization fragmentation of the parent molecule, the ratio of peak areas between the $Me_2\dot{S}iCH_2CH=CH_2$ (m/z = 99) peak and the parent peak is plotted in Figure 3.7, in order to identify the onset of the thermal decomposition reaction (3.6). It showed that when the temperature reached ~ 1100 K, the curve started to increase. $•CH_3$ was the co-product of $Me_2\dot{S}iCH_2CH=CH_2$ in reaction (3.6), and in Figure 3.6, the lowest temperature that m/z = 15 signal appeared was 1090 K, in agreement with the appearance of the $Me_2\dot{S}iCH_2CH=CH_2$ co-product (m/z = 99). Although secondary reactions of other primary hydrocarbon products such as C_3H_6 could produce $•CH_3$,[25] they were considered to be less likely at this temperature. Based on the quantum chemistry calculations shown in Figure 3.8, the methyl loss channel from allyltrimethylsilane (reaction (3.6)) has an energy threshold of 82.3 kcal/mol, while the methyl loss energy from propene is 95.9 kcal/mol.[25] Therefore, it is more likely that reaction (3.6) was initiated at around 1100 K and led to the formation of m/z = 15 peak and the increase of peak intensity of m/z = 99 ($Me_2\dot{S}iCH_2CH=CH_2$) above the photoionization fragmentation.

The m/z = 98 peak was first observed at 1260 K, and the signal did not increase significantly as the temperature increased. There were two possible reaction pathways leading to its appearance. The first possible mechanism was direct elimination of CH_4 from the parent molecule. According to Figure 3.8, the parent molecule could decompose to $Me_2Si=CHCH=CH_2$ and CH_4 directly through a transition state (TS3). The energy barrier was calculated to be 82.4 kcal/mol, which is almost as high as the energy required in the formation of $\bullet CH_3$ and $Me_2\dot{S}iCH_2CH=CH_2$ (reaction (3.6)). CH_4 is the counterpart of $Me_2Si=CHCH=CH_2$ in this elimination reaction; however, CH_4 was not detected as its ionization potential is higher than the 10.5 eV VUV radiation used in this chapter. Another possible reaction route leading to the m/z = 98 peak was H-loss channel from

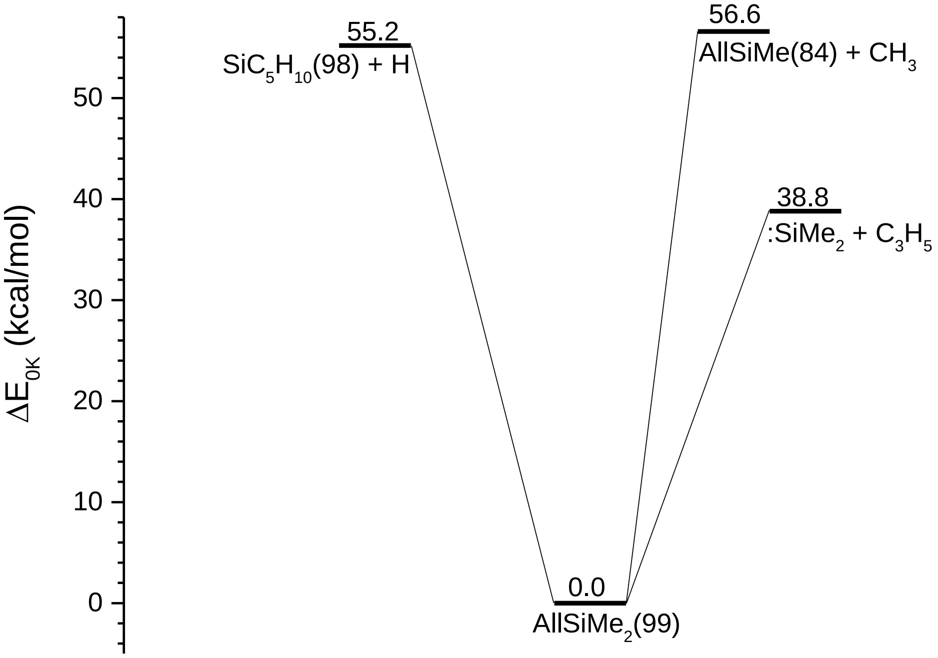

Figure 3.9 Potential energy diagram of secondary reaction pathways of $AllSiMe_2$ ($Me_2\dot{S}iCH_2CH=CH_2$). The energy (0 K) of each species were calculated at UB3LYP/6-311++G(d,p) level, with ZPE corrections.

$Me_2\dot{S}iCH_2CH{=}CH_2$ (m/z = 99). The m/z = 98 peak seemed to follow m/z = 99 and appeared at higher temperatures after m/z = 99 was produced. As indicated by the quantum chemistry calculations in Figure 3.9, $Me_2\dot{S}iCH_2CH{=}CH_2$ could undergo secondary dissociation to H + $Me_2Si{=}CHCH{=}CH_2$ (m/z = 98), which was activated by additional collisions, over a 55.2 kcal/mol energy barrier.

In Figure 3.5, the signal at m/z = 100 was not found at any elevated temperatures. This is consistent with the previous studies, where vinyltrimethylsilane was produced mainly by bimolecular mechanisms.[9, 11] Due to the short reaction time and low concentration of the precursor in this chapter, bimolecular reactions were minimized, and thus no vinyltrimethylsilane was produced.

(c) Secondary reactions of $Me_2Si{=}CH_2$ and Me_3Si•

SiC_3H_4 (m/z = 68) has been found as a major product among thermal decomposition of organosilicons and its structure and isomers have been reported.[26, 27] In this chapter, the m/z = 68 product was observed and considered to be produced via sequential H_2 lost channels initiated from $Me_2Si{=}CH_2$. This mechanism has been reported by Liu et al. (reaction (3.20)).[13]

$$Me_2Si{=}CH_2 \rightarrow :Si(H)C_3H_7 \rightarrow :Si{=}CHCH_2CH_3 + H_2 \rightarrow :Si(H)CH_2CH{=}CH_2 + H_2 \rightarrow :Si{=}CHCH{=}CH_2 + 2H_2 \qquad (3.20)$$

The m/z = 54 – 58 peaks were produced by secondary reactions of $Me_3Si•$. Although their production from direct elimination reactions of the parent molecule was considered theoretically (Figure 3.8), the energy required for TS1 (115.0 kcal/mol) to the target molecules was too high compared to other reaction pathways. The secondary reaction pathways of $Me_3Si•$ were summarized by Liu et al.[13] It was proposed that $Me_3Si•$ went through a $•CH_3$ loss channel (reaction (3.21)) forming $:SiMe_2$ (m/z = 58), and $:SiMe_2$ further underwent H_2 elimination channels (reaction (3.22)), leading to m/z = 56 products such as $:Si{=}CHCH_3$ and m/z = 54 products such as $:Si{=}C{=}CH_2$.[13] $:SiMe_2$ could also lose a methyl group forming SiMe (m/z = 43) and a methane forming $:Si{=}CH_2$.[12, 13] However, these contributions to m/z = 43 and 42 were considered to be small.[12, 13]

$$Me_3Si• \rightarrow :SiMe_2 + •CH_3 \tag{3.21}$$

$$:SiMe_2 \rightarrow :Si{=}CHCH_3 + H_2 \rightarrow :Si{=}C{=}CH_2 + 2H_2 \tag{3.22}$$

A minor peak at m/z = 28 was observed at temperatures ≥ ~ 1200 K. This might be attributed to the production of the Si atom, following isomerization and decomposition of $Me_2Si{=}CH_2$.[13] Alternatively, it could correspond to C_2H_4, which was produced from secondary reactions of the C_3H_5 or C_3H_6 species.

(d) Secondary reactions of $Me_2\dot{S}iCH_2CH{=}CH_2$

As described previously, at around 1100 K, the mass peak of m/z = 99 became obvious compared to the intensity of the parent peak, which suggested the formation of

$Me_2\dot{S}iCH_2CH=CH_2$. The theoretical calculations suggested that there were three possible decomposition pathways of $Me_2\dot{S}iCH_2CH=CH_2$ (m/z = 99), as shown in Figure 3.9. It could form $:SiMe_2$ by losing an allyl group, with an energy threshold of 38.8 kcal/mol. However, this reaction pathway could not be clearly determined from the mass spectra, since $:SiMe_2$ could also be produced from the secondary reaction of $Me_3Si\bullet$ (reaction (3.21)) and the allyl radical from the primary decomposition of the parent molecule (reaction (3.3)). $Me_2\dot{S}iCH_2CH=CH_2$ could lose an additional methyl group to form $MeSiCH_2CH=CH_2$ (m/z = 84) with a threshold energy of 56.6 kcal/mol, and this was observed as a very minor channel at temperatures higher than 1260 K. The H-loss channel forming $Me_2Si=CHCH=CH_2$ (m/z = 98), as discussed previously, was also possible, with a 55.2 kcal/mol energy threshold.

3.4 Conclusion

The thermal decomposition of allyltrichlorosilane and allyltrimethylsilane were examined experimentally by flash pyrolysis mass spectrometry and theoretically by DFT method. The main decomposition pathways are summarized in Scheme 3.1 and 3.2. The initial step in the decomposition of allyltrichlorosilane was the Si-C bond cleavage producing $\bullet SiCl_3$ and $\bullet C_3H_5$. $\bullet SiCl_3$ then decomposed via sequential Cl losses forming $:SiCl_2$, SiCl and Si. The C_3H_5 radical went through secondary decompositions, and the main product were C_3H_4 (m/z = 40) + H. As the temperature increased, further H elimination reactions took place.

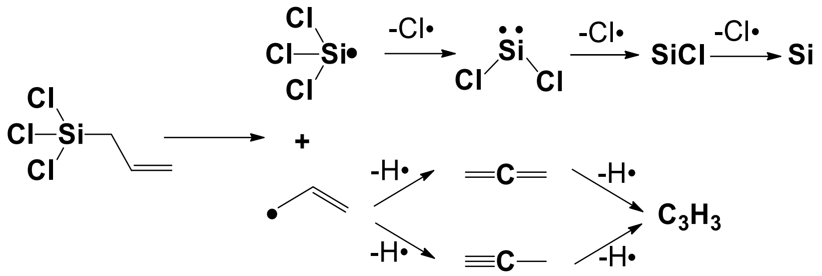

Scheme 3.1 Main decomposition mechanisms of allyltrichlorosilane.

In the pyrolysis of allyltrimethylsilane, $Me_2Si=CH_2$, $Me_3Si\bullet$ and $Me_2\dot{S}iCH_2CH=CH_2$ were considered as three main initial reaction products. Our investigations showed that starting around 1050 K, $Me_2Si=CH_2$ and C_3H_6 were produced via reaction (3.1) and $Me_3Si\bullet$ and $\bullet C_3H_5$ via reaction (3.3). The methyl-loss channel of allyltrimethylsilane leading to the formation of $Me_2\dot{S}iCH_2CH=CH_2$ and $\bullet CH_3$ started at around 1100 K. The yield of $HSiMe_3$ and C_3H_4 from the parent molecule was also found to be possible at or above ~ 1090 K. Secondary reactions of these primary products were also examined. Vinyltrimethylsilane was not identified as a product.

In comparison, allyltrichlorosilane decomposed primarily via the Si-C bond homolysis, and the subsequent reactions of the allyl and trichlorosilyl radical were isolated and proceeded independently. Allyltrimethylsilane, with the availability of the methyl groups, decomposed via both molecular eliminations and Si-C bond fissions. The study on the isolated allyl reactions in allyltricholorosilane helped to unravel the complex decomposition mechanism of allyltrimethylsilane.

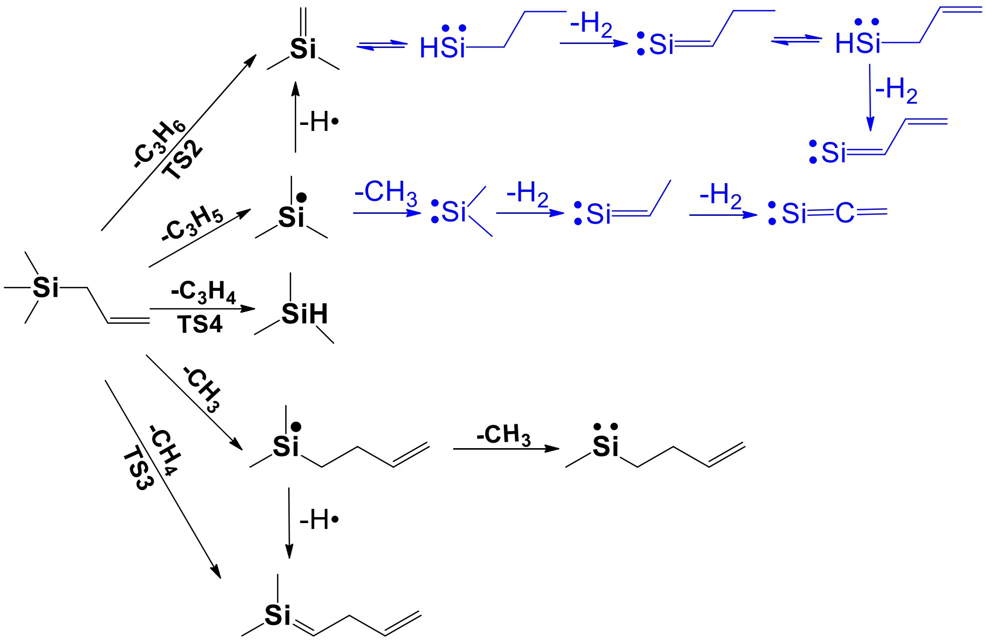

Scheme 3.2 Main decomposition mechanism of allyltrimethylsilane. The secondary reactions displayed in blue color have been reported by Liu et al.[13]

REFERENCE

1. D. Hotza, M. Di Luccio, M. Wilhelm, Y. Iwamoto, S. Bernard and J. C. Diniz da Costa, *Journal of Membrane Science*, 2020, **610**, 118193.

2. R. F. Davis, in *Reference Module in Materials Science and Materials Engineering*, Elsevier, 2017.

3. S. W. Rynders, A. Scheeline and P. W. Bohn, *Journal of Applied Physics*, 1991, **69**, 2951-2960.

4. A. D. Johnson, J. Perrin, J. A. Mucha and D. E. Ibbotson, *The Journal of Physical Chemistry*, 1993, **97**, 12937-12948.

5. Y. Shi, *Accounts of Chemical Research*, 2015, **48**, 163-173.

6. W. J. Bailey and M. S. Kaufmann, 157th. Nat. Meeting of Am. Chem. Soc., Minneapolis, 1969.

7. H. Sakurai, A. Hosomi and M. J. Kumada, *Chem. Soc., Chem. Commun.*, 1970, **767**.

8. S. M. Neider, G. R. Chambers and M. Jones, Jr. , *Tetrahedron Lett.*, 1979, **40**.

9. I. M. T. Davidson and I. T. Wood, *Journal of Organometallic Chemistry*, 1980, **202**, C65-C67.

10. T. J. Barton, S. A. Burns, I. M. T. Davidson, S. Ijadi-Maghsoodi and I. T. Wood, *Journal of the American Chemical Society*, 1984, **106**, 6367-6372.

11. I. M. T. Davidson, *Journal of Organometallic Chemistry*, 1988, **341**, 255-265.

12. J. M. Lemieux and J. Zhang, *International Journal of Mass Spectrometry*, 2014, **373**, 50-55.

13. X. Liu, J. Zhang, A. Vazquez, D. Wang and S. Li, *Physical Chemistry Chemical Physics*, 2018, **20**, 18782-18789.

14. B. S. Narendrapurapu, A. C. Simmonett, H. F. Schaefer, J. A. Miller and S. J. Klippenstein, *The Journal of Physical Chemistry A*, 2011, **115**, 14209-14214.

15. S. E. Boganov, V. M. Promyslov, I. V. Krylova, G. S. Zaitseva and M. P. Egorov, *Russian Chemical Bulletin*, 2016, **65**, 1216-1224.

16. M. Frisch, G. Trucks, H. B. Schlegel, G. E. Scuseria, M. A. Robb, J. R. Cheeseman, G. Scalmani, V. Barone, B. Mennucci and G. Petersson, *Inc., Wallingford, CT*, 2009, **200**.

17. M. Wang, G. Audi, F. G. Kondev, W. J. Huang, S. Naimi and X. Xu, *Chinese Physics C*, 2017, **41**, 030003.

18. J. C. Traeger, *International Journal of Mass Spectrometry and Ion Processes*, 1984, **58**, 259-271.

19. K. Kimura, T. Yamazaki and Y. Achiba, *Chemical Physics Letters*, 1978, **58**, 104-107.

20. K. Ohno, K. Okamura, H. Yamakado, S. Hoshino, T. Takami and M. Yamauchi, *The Journal of Physical Chemistry*, 1995, **99**, 14247-14253.

21. S. G. Davis, C. K. Law and H. Wang, *The Journal of Physical Chemistry A*, 1999, **103**, 5889-5899.

22. C. Chen, B. Braams, D. Y. Lee, J. M. Bowman, P. L. Houston and D. Stranges, *The Journal of Physical Chemistry A*, 2011, **115**, 6797-6804.

23. Y. Song, M. Lucas, M. Alcaraz, J. Zhang and C. Brazier, *The Journal of Physical Chemistry A*, 2015, **119**, 12318-12328.

24. W. Tsang, *Journal of Physical and Chemical Reference Data*, 1991, **20**, 221-273.

25. R. C. Sharma and M. Koshi, *Spectrochim Acta A Mol Biomol Spectrosc*, 2006, **65**, 787-791.

26. G. W. Schriver, M. J. Fink and M. S. Gordon, *Organometallics*, 1987, **6**, 1977-1984.

27. G. Maier, H. P. Reisenauer, J. Jung, H. Pacl and H. Egenolf, *European Journal of Organic Chemistry*, 1998, **1998**, 1297-1305.

CHAPTER 4 Mechanistic study of thermal decomposition of 1,1,2,2-tetramethyldisilane

4.1 Introduction

Tetramethyldisilane ($Me_2HSi\text{-}SiHMe_2$), for its thermodynamically weak Si-Si bond and more stable Si-C bond, has been considered as a good decomposable precursor for chemical vapor decomposition (CVD) of silicon carbide (SiC). Its application in producing amorphous silicon carbide (a-SiC:H) has been reported by Koinuma et al.[1] and Yoshida et al.[2] Because silanes could be activated by several transition-metal complexes,[3-6] interest in synthesizing alkenylsilanes from disilane and corresponding alkynes has increased, and investigations using tetramethyldisilane as reactants in the presence of gold and palladium catalysts have been reported.[7-9] Recently, efforts have been made by scientists to obtain stable substances containing sp^2-hybridized Si atoms;[10-12] however, the fundamental property of the Si=Si bond especially its reactivity in the gas phase is less known. Therefore, 1,1,2,2-tetramethyldisilane, besides its wide applications in industrial production and synthesis chemistry, is a potentially important precursor leading to the formation of a highly reactive intermediate tetramethyldisilene ($Me_2Si{=}SiMe_2$), and is an ideal candidate for exploring the fundamental property of the Si=Si double bond in the gas phase pyrolysis regime.

Tetramethyldisilene was first recognized as a labile intermediate in the reaction of 7,8-disilabicyclo[2.2.2]octa-2,5-dienes by Roark et al. in 1972.[13] A few years later, Barton and co-workers proposed that tetramethyldisilene could isomerize to trimethylsilylmethylsilylene followed by the formation of disilacyclopropane (reaction (4.1)) in the study of the gas-phase vacuum-flow pyrolysis of 2-chloroheptamethyltrisilane at 700 °C (0.15 Torr). Disilacyclopropane would further isomerize to two four-member ring isomers through silylene intermediates (reaction (4.2) and (4.3)).[14] Several theoretical chemistry investigations have also discussed the possibilities of those reaction channels.[15-18]

$Me_2Si{=}SiMe_2 \xrightarrow{\text{isomerization}} Me\ddot{Si}\text{-}SiMe_3 \rightarrow$ 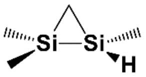 (4.1)

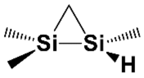 $\rightarrow Me_2HSiCH_2\text{-}\ddot{Si}Me \rightarrow$  (4.2)

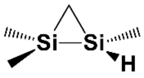 $\rightarrow Me_3SiCH_2\text{-}\ddot{Si}H \rightarrow$  (4.3)

There are only a limited number of investigations on the pyrolysis of 1,1,2,2-tetramethyldisilane.[19, 20] O’Neal and co-workers studied its thermal decomposition mechanism using the static methods, and they argued that the thermal dissociation of 1,1,2,2-tetramethyldisilane primarily proceeded via reaction (4.4) under the pressure from 50 - 200 Torr and at a temperature of 573 - 650 K in 90% argon diluent. They also argued that, unlike other disilanes, the elimination of H_2 (reaction (4.5)) was not identified as an initial step in 1,1,2,2-tetramethyldisilane pyrolysis, as D_2 was not detected in the thermolysis of 1,2-dideuterated tetramethyldisilane ($Me_2DSi\text{-}SiDMe_2$). An alternative explanation (a bimolecular reaction model) for the formation of $Me_2Si=SiMe_2$ was therefore raised (reaction (4.6) and (4.7)).[19]

$$Me_2HSi\text{-}SiHMe_2 \rightarrow Me_2SiH_2 + Me_2Si: \tag{4.4}$$

$$Me_2HSi\text{-}SiHMe_2 \rightarrow Me_2Si=SiMe_2 + H_2 \tag{4.5}$$

$$Me_2HSi\text{-}SiHMe_2 + Me_2Si: \rightarrow Me_2HSi\text{-}SiMe_2SiHMe_2 \tag{4.6}$$

$$Me_2HSi\text{-}SiMe_2SiHMe_2 \rightarrow Me_2SiH_2 + Me_2Si=SiMe_2 \tag{4.7}$$

Understanding the unimolecular decomposition mechanism of 1,1,2,2-tetramethyldislane is not only useful for better CVD processes, but also has the potential of elucidating the Si=Si double bond chemistry, whose relevant studies have been limited. Based on these motivations, the thermal decomposition of 1,1,2,2-tetramethyldisilane was performed experimentally using flash pyrolysis coupled with vacuum ultraviolet photoionization time-of-flight mass spectrometry (VUV-PI-TOF-MS). This experiment allowed the detection of reactive intermediates during the early stage of thermal decomposition. Computational studies regarding the decomposition pathways and their energetics were also carried out. Initiation steps in the 1,1,2,2-tetramethyldisilane pyrolysis, as well as important secondary reactions including the secondary reactions involving $Me_2Si=SiMe_2$, were identified and reported in this chapter. A more comprehensive decomposition mechanism of 1,1,2,2-tetramethyldisilane was developed.

4.2 Experimental and Computational methods

The 1,1,2,2-tetramethylsilane sample was purchased from Alfa Aesar (98+ %) and was diluted to ~1-2 % in the helium carrier gas. The precursor was introduced in the apparatus by bubbling the helium gas through the liquid sample. The experimental method was similar to what have been discussed in the previous chapters. Theoretical calculations on the geometries and energetics of corresponding transition states, intermediates, products, and reactants were performed using the Gaussian 09 program.[21] All geometries including transition states were optimized using the UB3LYP density functional theory (DFT) method[22, 23] under 6-311++G(d,p) basis sets.[24] Energies and vibrational frequencies for each species were obtained at the same level of theory, and zero-point energy corrections were made for all species involved. Transition states with only one imaginary frequency were tested using IRC calculations under the same level. All results are displayed with relative energies at 0 Kelvin (ΔE_{0K}).

4.3 Results and discussions

(a) Initiation steps of the thermal decomposition reactions

The pyrolysis mass spectra of 1,1,2,2-tetramethyldisilane thermal decomposition are shown in Figure 4.1. At room temperature (295 K), the peak at m/z = 118 corresponded to the parent molecule; smaller peaks, such as m/z = 119 and 120, were caused by the isotopes of Si and C (^{29}Si, ^{30}Si, and ^{13}C). The fragment signals at m/z = 43, 58, 59, 60, 73, 102, 103, and 116 were caused by dissociative photoionization of the parent molecule, not by the corresponding neutral fragments at 295 K. Unlike other fragmentation peaks, the

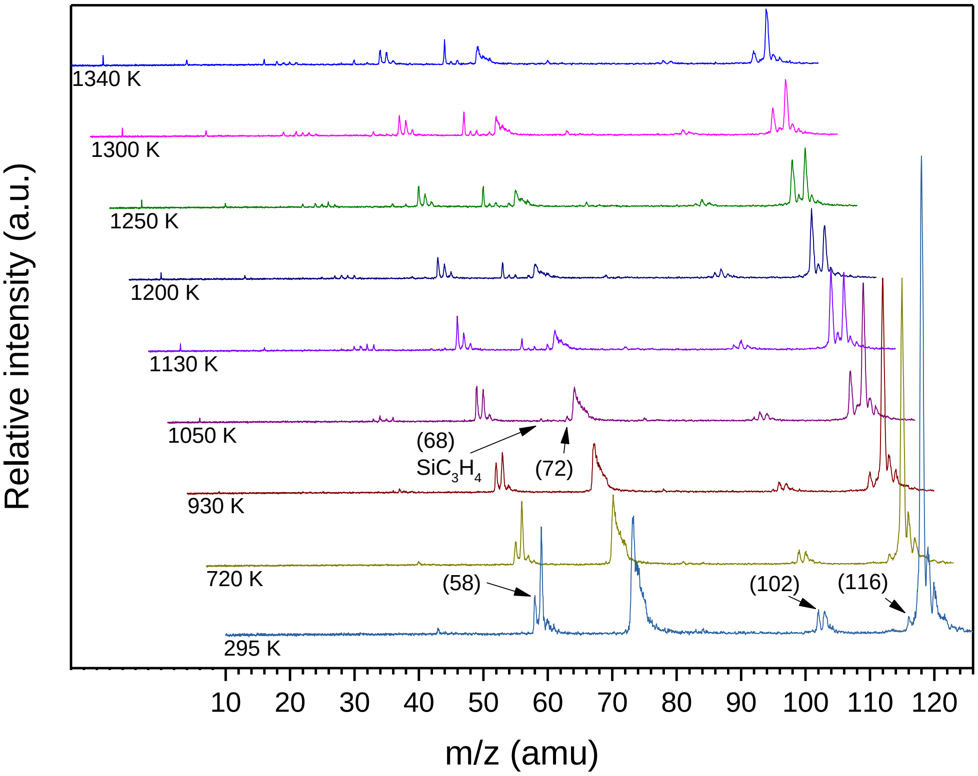

Figure 4.1 Mass spectra for the 1,1,2,2-tetramethyldisilane pyrolysis at 295 K to 1340 K. Two mass spectra at temperature between 410 K and 550 K were identical to that at 720 K and were omitted. The mass spectra are offset horizontally for clarity.

shape of m/z = 73 showed a tailing feature, which was caused by the metastable nature of the trimethylsilyl ion.[25, 26]

Figure 4.2 (the enlarged graph of Figure 4.1) shows that, at 930 K, the signal of m/z = 116 started to increase, and at 1050 K, the increase became significant. The intensity of the m/z = 116 peak further increased until 1200 K, and then gradually decreased. Meanwhile, the signal of the parent molecule decreased significantly with the increasing temperature. As the signal of fragments could be composed of the parent dissociative photoionization and direct photoionization of the corresponding neural thermal decomposition products, the ratio of the peak area of the fragment peak to that of the parent molecule as a function of the increasing temperature could be examined to elucidate the

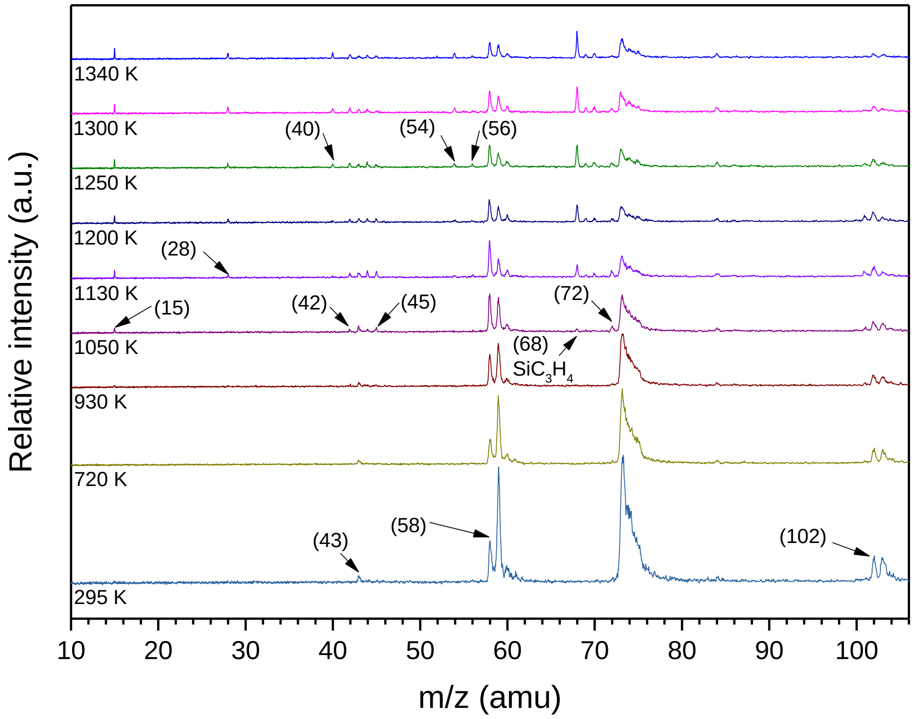

Figure 4.2 The enlarged graph of Figure 4.1 showing the signals of smaller peaks.

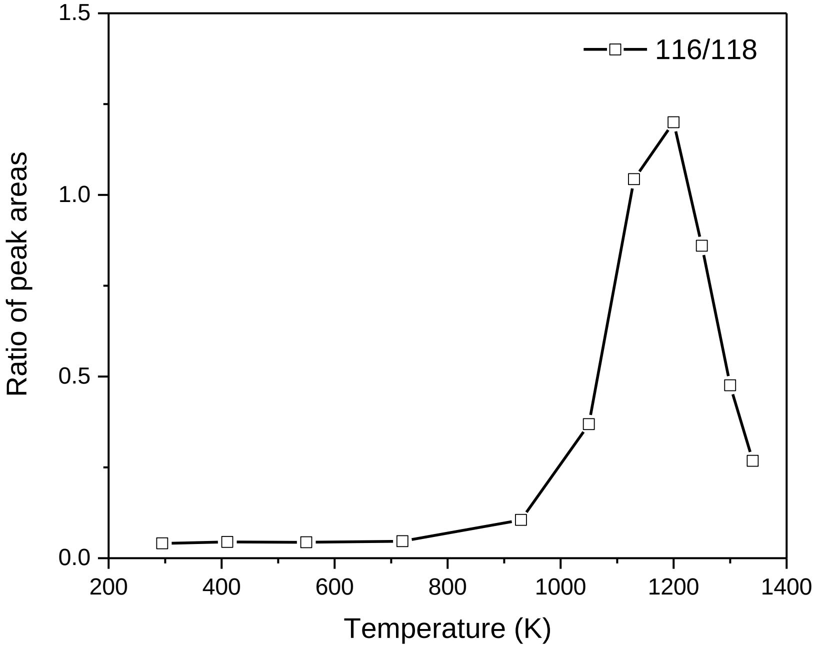

Figure 4.3 Peak area ratio of m/z = 116 to m/z = 118 in the temperature range of 295 K to 1340 K.

dissociation process at elevated temperatures.[27] Figure 4.3 shows that the ratio of the peak area of m/z = 116 over m/z = 118 which provides evidence that around 930 K, neutral species with m/z = 116 started to be produced. The ratio of the peak areas increased with the increase of temperature until ~ 1200 K, and then the ratio started to decrease, which is likely due to the faster consumptions of the m/z = 116 species than its production from the primary initiation reactions at high temperatures.

In Figure 4.4, the DFT calculations regarding the initiation reaction pathways of the parent molecule are presented. The H_2 elimination reaction (4.5) via TS2 has an energy barrier of 82.6 kcal/mol which is higher compared to other possible initiation channels but is still feasible. Although Nag et al.[15] and Boo et al.,[17] have demonstrated that multiple isomerization processes could form different isomers at m/z = 116 (reaction (4.1) - (4.3)), it is still considered that the m/z = 116 species was initially produced as tetramethyldisilene ($Me_2Si{=}SiMe_2$) at around 930 K because tetramethyldisilene was the most likely isomer of m/z = 116 initially evolved from 1,1,2,2-tetramethyldisilane.

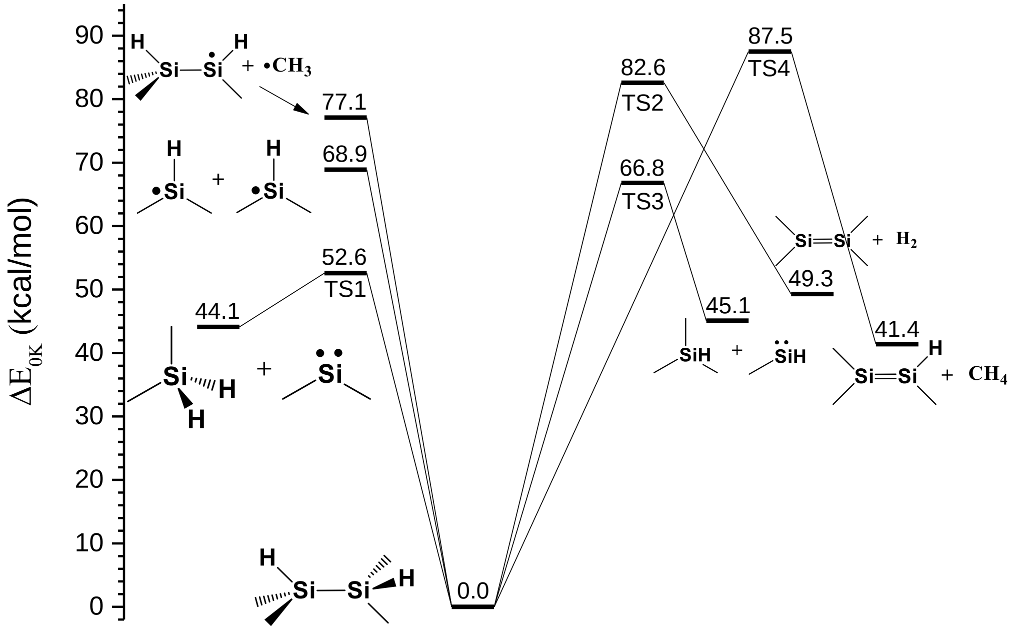

Figure 4.4 Potential energy diagram of the initiation steps in the pyrolysis of 1,1,2,2-tetramethyldisilane. The energy (0 K) of each species were calculated at UB3LYP/6-311++G(d,p) level, with ZPE correction.

Evidence for the occurrence of reaction (4.4) was found. As shown in Figure 4.1 and 4.2, the signal at m/z = 58 (Me_2Si:) increased at around 930 K. The signal remained constant when the temperature further increased, and when the temperature reached higher than 1200 K, the peak intensity started to decrease, probably due to secondary decomposition reactions that became more significant as the temperature built up. The ratio of peak areas for fragment signals against that of the parent molecule are depicted in Figure 4.5 to clarify the contributions from the thermal decompositions. It shows that at around 930 K, the curve of m/z 58/118 started increasing, and when the temperature reached around 1130 K, the ratio of m/z 58/118 started to decrease all the way to the highest temperature of 1340 K. Also, Figure 4.5 shows that the m/z 60/118 curve started to increase at around 1000 K, and then decreased when it reached its highest value at 1200 K. The m/z 60 peak could represent the signal of Me_2SiH_2 from thermal decomposition reaction (4.4).

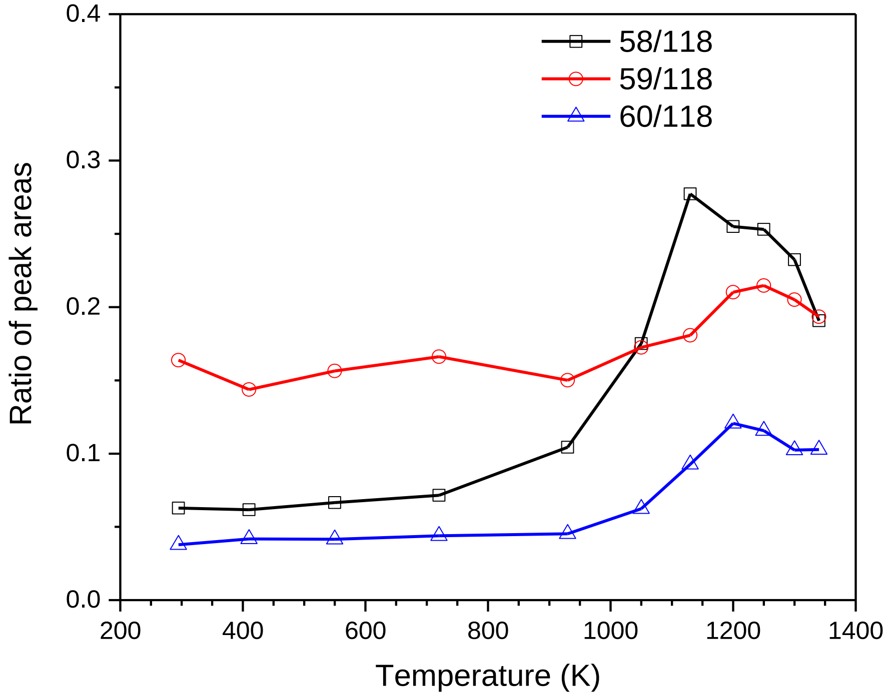

Figure 4.5 Plots of the m/z = 58, 59 and 60 peak area over m/z = 118 peak area at temperatures ranging from 295 K to 1340 K.

Although m/z 58 and m/z 59 peaks could have a small isotope peak at m/z 60 (due to natural isotope abundance of Si, ^{28}Si:^{29}Si:^{30}Si = 0.92:0.05:0.03), the intensity of the observed m/z 60 peak was significantly higher than that expected from the +1 and/or +2 isotope peaks of the m/z = 59 and 58 species, indicating small contributions from the isotope peaks of the m/z = 59 and 58 species and main contribution from the thermal decomposition reaction (4.4). The decrease in the ratio of the peak area value of m/z 58/118 and 60/118 was possibly caused by the secondary decomposition reactions of these two intermediates. The m/z 60/118 curve was not found to increase simultaneously as the m/z 58/118 curve at around 930 K, probably due to its smaller ionization cross section value and/or significant dissociative photoionization,[28] thus, making the detection of the m/z 60 signal difficult. Note that as the dissociative photoionization of Me_2SiH_2 at m/z 60 could produce a significant amount of m/z 58 fragment ions,[28] the peak m/z 58 could also be an indication of Me_2SiH_2. As Me_2SiH_2 at m/z 60 and Me_2Si: at m/z 58 were co-products of the dissociation reaction (4.4). the m/z 58 Me_2Si: peak thus can have two components from the same reaction (4.4), thermal dissociation of the parent and dissociative photoionization of its co-product Me_2SiH_2. Therefore, the increase of m/z 58/118 was used to determine the onset temperature for reaction (4.4), which was around 930 K. According to Figure 4.4, the thermal decomposition of 1,1,2,2-tetramethyldisilane to Me_2Si: and Me_2SiH_2 via reaction (4.4) through a transition state (TS1) has the lowest energy barrier (52.6 kcal/mol) among all the initiation reaction channels, and this supports the arguments above.

The Si-Si single bond homolysis forming dimethylsilyl radicals (reaction (4.8)) was also observed in this chapter. As mentioned earlier, at 295 K, the m/z = 59 signal was produced from the dissociative photoionization of the parent molecule. The signal for m/z = 59 started to decrease as the temperature gradually built up. Instead, the ratio of the peak areas for m/z 59/118 is more informative showing the growth of m/z = 59 peak with respect to the parent (see Figure 4.5). It indicates that the ratio for m/z 59/118 increased around 1000 K, while it was nearly constant below 1000 K. The baseline for the m/z 59/118 curve at low temperatures was not well defined, making it difficult to determine the onset temperature of reaction (4.8). The possible reason is that the contribution of the dissociative photoionization of the parent molecule to the m/z = 59 peak was large, so the overall intensity of m/z = 59 decreased with decreasing parent intensity when temperature built up, and the growth of the neutral fragment at m/z = 59 can only be detected by the ratio of peak areas.[27] The possibility of the secondary reactions that occurred between m/z = 58 – 60 species also made the determination of the initiation reactions complicated. According to Toukabri et al.,[28] dimethylsilane could lose H_2 to form dimethylsilylene or methylsilene ($MeHSi{=}CH_2$), and it could also decompose into dimethylsilyl radical by losing one H atom (reaction (4.9) - (4.11)). The isotope peak (+1) of m/z = 58 could also contribute to the signal of the m/z = 59 peak; however, this contribution should be very small based on the isotope abundance of Si. Figure 4.4 shows that reaction (4.8) requires an energy threshold of 68.9 kcal/mol which is 16.3 kcal/mol higher than that of reaction (4.4) and lower than any other competing pathways. This indicated that reaction (4.8) was also one of the main decomposition channels in the 1,1,2,2-tetramethyldisilane pyrolysis. The reaction (4.11) was believed to contribute little to the m/z = 59 peak, because this first required Me_2SiH_2 production from reaction (4.4) and furthermore the S-H bond in

Me_2SiH_2 is 89.9 kcal/mol, higher than the energy threshold for reaction (4.8). Therefore, it is considered that the m/z = 59 peak was primarily produced by reaction (4.8) at around 1000 K.

$$Me_2HSi\text{-}SiHMe_2 \rightarrow 2\ Me_2HSi\bullet \tag{4.8}$$

$$Me_2SiH_2 \rightarrow Me_2Si: + H_2 \tag{4.9}$$

$$Me_2SiH_2 \rightarrow MeHSi{=}CH_2 + H_2 \tag{4.10}$$

$$Me_2SiH_2 \rightarrow Me_2SiH\bullet + H\bullet \tag{4.11}$$

In addition, evidence for the production of Me_3SiH and :SiHMe (reaction (4.12)) was identified. As shown in Figure 4.2, the m/z = 73 peaks were caused by dissociative photoionization of the parent molecule at 295 K. When the temperature increased, the signal of the m/z = 73 peak started to decrease. The ratio of the peak area of m/z = 73 vs m/z = 118 as a function of temperature is plotted in Figure 4.6. The tail of the m/z = 73 peaks was included in the peak area integration. It shows that at around 1050 K, the curve started to increase, which might suggest that the neutral trimethylsilyl radical was produced from the thermal decomposition reaction, or from the dissociative photoionization of Me_3SiH. According to theoretical calculations in this chapter, the isomerization of 1,1,2,2-

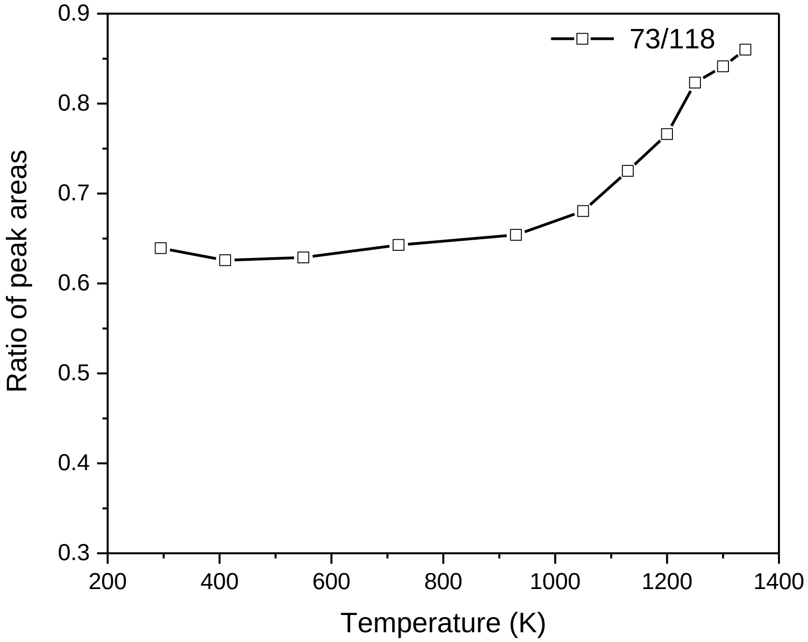

Figure 4.6 Peak area ratio of m/z = 73 to m/z = 118 in the temperature range of 295 K to 1340 K.

tetramethyldisilane to 1,1,1,2-tetramethyldisilane leading to the formation of the trimethylsilyl radical was unlikely to occur; instead, 1,1,2,2-tetramethyldisilane decomposed into Me_3SiH + :SiHMe reaction (4.12)), and Me_3SiH then readily lost one H producing trimethylsilyl radical (reaction (4.13)). The energy barrier for reaction (4.12) was determined to be 66.8 kcal/mol via TS3, as shown in Figure 4.4. Figure 4.1 and 4.2 show that the m/z = 74 peaks overlapped with the tail of the m/z = 73 peaks, making its direct observation difficult. As the counter-product of Me_3SiH in reaction (4.12), :SiHMe (m/z = 44) was first observed at 1050 K, suggesting that the onset temperature for reaction (4.12) was probably around 1050 K. This is consistent with Figure 4.6, which showed that Me_3SiH was formed via reaction (4.12) at around 1050 K and it might readily decompose into $•SiMe_3$ (reaction (4.13)). This also agreed with the appearance temperature of the m/z = 72 peak at 1050 K, as the m/z = 72 species ($Me_2Si{=}CH_2$) could be produced from H-atom loss reaction from the trimethylsilyl radical (reaction (4.14)) according to previous studies.[27, 29] Although the signal of Me_3SiH could not be observed directly, the appearance of its counter-product (:SiHMe) and the relatively low energy barrier according to Figure 4.4 suggested that reaction (4.12) could also be considered as a major initiation reaction channel of 1,1,2,2-tetramethyldisilane. An alternative source or additional contribution to the increase of m/z 73 peak at and above ~1050 K (as shown in the m/z 73/118 ratio curve in Figure 4.6) could be dissociative ionization of Me_3SiH from reaction (4.12). It is known that photoionization of Me_3SiH at 10.49 eV produces a significant amount of m/z 73 ion fragment.[30] Nevertheless, this contribution to m/z 73 also supported that Me_3SiH was produced from reaction (4.12).

$$Me_2HSi\text{-}SiHMe_2 \rightarrow Me_3SiH + MeHSi: \tag{4.12}$$

$$Me_3SiH \xrightarrow{-H} Me_3Si\bullet \tag{4.13}$$

$$Me_3Si\bullet \xrightarrow{-H} Me_2Si{=}CH_2 \tag{4.14}$$

In addition to the initiation reaction channels discussed above, the methyl-loss channel (reaction (4.15)) and CH_4 elimination channel (reaction (4.16)) of the parent molecule were also identified in this chapter. As shown in Figure 4.1 and 4.2, the m/z = 102 ($Me_2Si{=}SiHMe$) and m/z = 103 ($Me_2HSi\text{-}SiHMe$) peaks were detected at 295 K as dissociative photoionization peaks. The intensities of these two peaks decreased as the temperature gradually increased. The ratio of the peak area against the parent peak for these two peaks are presented in Figure 4.7. An increase was observed in Figure 4.7 for both

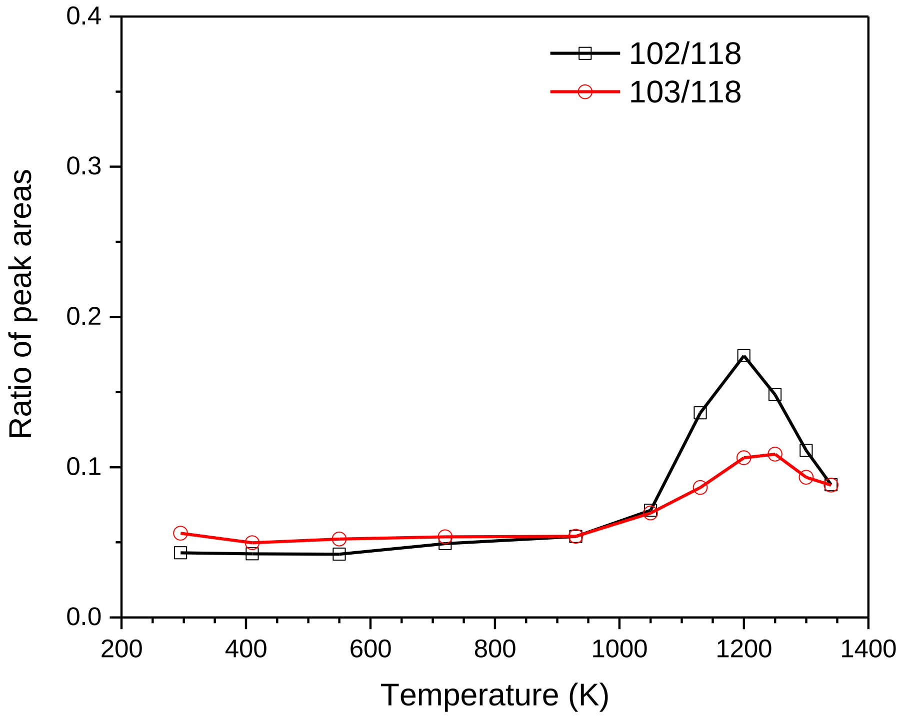

Figure 4.7 The plot of the m/z = 102, 103 peak area over m/z = 118 peak area under temperature ranging from 295 K to 1340 K.

curves at around 1050 K, and it suggests that the onset temperatures for reaction (4.15) and reaction (4.16) were likely to be around 1050 K. The energetics for these two reactions were calculated and displayed in Figure 4.4. It showed that reaction (4.15) has an energy threshold of 77.1 kcal/mol while the energy barrier for reaction (4.16) is 87.5 kcal/mol via transition state TS4. $Me_2Si=SiHMe$ could also be produced from the H loss channel of $Me_2HSi\text{-}\dot{S}iHMe$ (reaction (17)). However, since the intensities for both peaks were small, reaction (4.15) – (4.17) were considered minor.

$$Me_2HSi\text{-}SiHMe_2 \rightarrow Me_2HSi\text{-}\dot{S}iHMe + \bullet CH_3 \tag{4.15}$$

$$Me_2HSi\text{-}SiHMe_2 \rightarrow Me_2Si=SiHMe + CH_4 \tag{4.16}$$

$$\mathrm{Me_2HSi\text{-}\dot{S}iHMe} \rightarrow \mathrm{Me_2Si{=}SiHMe} + {\bullet}\mathrm{H} \tag{4.17}$$

(b) Secondary reactions of 1,1,2,2-tetramethyldisilene

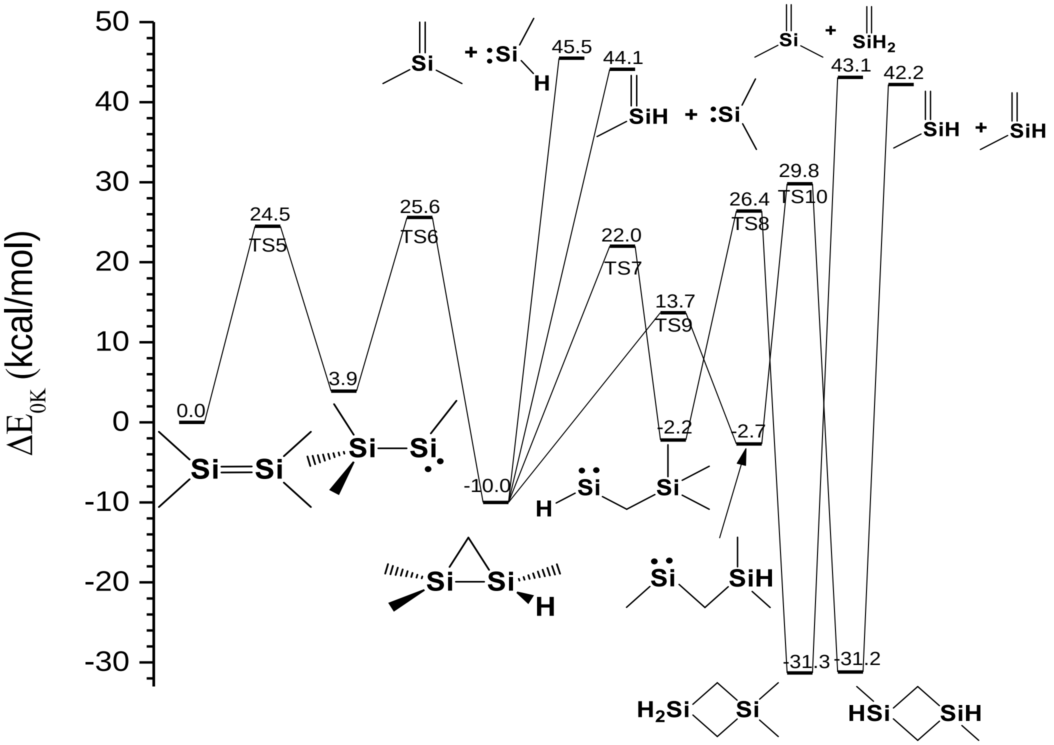

Figure 4.8 Potential energy diagram of secondary reactions of tetramethyldisilene. The energy (0 K) of each species were calculated at UB3LYP/6-311++G(d,p) level, with ZPE correction.

The secondary reactions of $Me_2Si=SiMe_2$ were also considered. The chemistry of tetramethyldisilene (m/z = 116) has been focused on in several earlier studies.[13-15, 17] Isomerization of disilene to silylsilylene has been accepted as one of the initiation steps in disilene chemistry. According to Nag et al.[15] and Boo et al.,[17] silylsilene will further rearrange to disilacyclopropane (reaction (4.1)). And according to Auner et al.,[31] disilacyclopropane could decompose into two smaller fragments (reaction (4.18a) and (4.18b)) in the thermolysis study of 1,3-dimethyl-1,3-disilacyclobutane. Here, reaction (4.18a) provides an alternative way of explaining $Me_2Si=CH_2$ (m/z = 72) via the secondary reactions of 1,1,2,2-tetramthyldisilene ($Me_2Si=SiMe_2$). Similarly, reaction (4.18b) provides another possible explanation for the formation of the m/z = 58 species. In the current work, the dissociation mechanism of tetramethyldisilene was proposed, and its energetics were calculated and displayed in Figure 4.8. $Me_2Si=SiMe_2$ (1,1,2,2-tetramethyldisilene), which was produced from reaction (4.5), first isomerizes to $Me\ddot{S}i\text{-}SiMe_3$ with an energy barrier of 24.5 kcal/mol (TS5), and then $Me\ddot{S}i\text{-}SiMe_3$ further isomerizes to disilacyclopropane via TS6 with an energy barrier of 21.7 kcal/mol (reaction (4.1)). After that, the decomposition of disilacyclopropane can lead to the formation of $Me_2Si=CH_2$ and :SiHMe (reaction (4.18a)) or $HMeSi=CH_2$ and $:SiMe_2$ (reaction (4.18b)). The overall energy thresholds for these two channels were determined to be 45.5 and 44.1 kcal/mol relative to 1,1,2,2-tetramethyldisilene, respectively. $Me_2Si=CH_2$ then undergoes a series of secondary reactions which leads to the formation of the m/z = 68 species (reaction (4.19)), as studied previously.[24, 27, 29, 32-34]

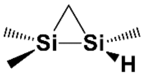

$\rightarrow \mathrm{Me_2Si{=}CH_2} + \mathrm{:SiHMe}$ (4.18a)

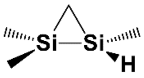

$\rightarrow \mathrm{HMeSi{=}CH_2} + \mathrm{:SiMe_2}$ (4.18b)

$$\mathrm{Me_2Si{=}CH_2} \leftrightarrow \mathrm{:Si(H)Pr} \rightarrow \mathrm{:Si{=}CHCH_2CH_3{+}H_2} \leftrightarrow \mathrm{:Si(H)CH_2CH{=}CH_2{+}H_2}$$
$$\rightarrow \mathrm{:Si{=}CHCH{=}CH_2} + 2\mathrm{H_2} \quad (4.19)$$

The possible reaction channels which lead to the production of 1,3-dimethyl-1,3-disilacyclobutane or 1,1-dimethyl-1,3-disilacyclobutane were also calculated and are shown in Figure 8. Both could be evolved from the secondary reactions of disilacyclopropane by overcoming two transition states. The potential energies of these two species are ~ 30 kcal/mol lower than that of tetramethyldisilene which indicates that they are thermodynamically more stable than tetramethyldisilene. The existence of those two species was suggested by the appearance of the m/z = 101 peak from 930 K to 1200 K, as the m/z = 101 peak was likely to be the CH_3-loss dissociative photoionization signal of 1,3-dimethyl-1,3-disilacyclobutane or 1,1-dimethyl-1,3-disilacyclobutane, similar to the CH_3-loss channel in the dissociative ionization of an analogous compound 1,1,3,3-tetramethyl-1,3-disilacyclobutane.[35]

In addition to the reaction pathways mentioned above involving the formation of dimethylsilene from disilacyclopropane, the cycloreversion reactions of 1,1-dimethyl-1,3-disilacyclobutane could also lead to dimethylsilene ($Me_2Si{=}CH_2$). The ring-opening mechanism of 1,3-disilacyclobutane and its derivatives were reported previously.[36-39] There were two pathways reported for the further reactions of 1,3-disilacyclobutane and its derivatives that could be responsible for the formation of $Me_2Si=CH_2$; one was stepwise 2+2 cycloreversion and the other was concerted 2+2 cycloreversion. The possible reaction pathways for 1,1-dimethyl-1,3-disilacyclobutane applying those mechanisms were depicted in Scheme 4.1. As shown in Scheme 4.1, 1,1-dimethyl-1,3-disilacyclobutane could decompose into $Me_2Si=CH_2$ and $H_2Si=CH_2$ directly via the concerted 2+2 cycloreversion pathway, or the stepwise 2+2 cycloreversion pathway through a diradical intermediate. According to the theoretical investigations of 1,3-disilacyclobutane reported by Badran et al.,[38] the two 2+2 cycloreversion pathways were less kinetically favored. Also, the formation of 1,1-dimethyl-1,3-disilacyclobutane, although it has slightly lower energy barrier than reaction (4.18a), required the formation of disilacyclopropane as an intermediate, and disilacyclopropane has been considered as a key intermediate for the formation of $Me_2Si=CH_2$. Therefore, the contributions of those two 2+2 cycloreversion channels of 1,1-dimethyl-1,3-disilacyclobutane (reaction (4.20)) were considered possible but not significant in the formation of dimethylsilene. Similarly, the cycloreversion reaction of 1,3-dimethyl-1,3-disilacyclobutane producing $MeHSi=CH_2$ and $MeHSi=CH_2$ (reaction (4.21)) were also considered to be minor.

$$\rightarrow Me_2Si=CH_2 + H_2Si=CH_2 \qquad (4.20)$$

$$\rightarrow MeHSi=CH_2 + MeHSi=CH_2 \qquad (4.21)$$

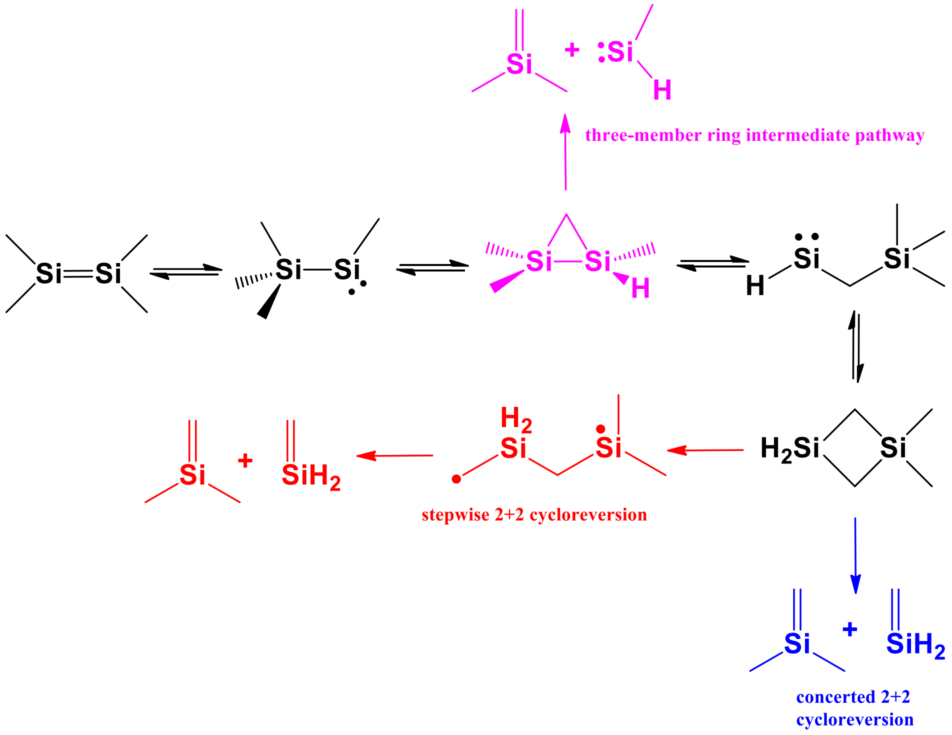

Scheme 4.1 Possible reaction pathways for the dimethylsilene formation from 1,1-dimethyl-1,3-disilacyclobutane.

(c) Analysis of other secondary reactions

As discussed earlier, the m/z = 72 species $Me_2Si=CH_2$ could be produced from two major pathways, from secondary decomposition (reaction (4.18a) and (4.20)) of tetramethyldisilene produced in reaction (4.5), and from secondary reactions of trimethylsilane that was produced in reaction (4.12) via sequential H loss (reaction (4.13) and (4.14)) or H_2 elimination (reaction (4.22)). According to the theoretical calculations, the threshold energy for the H-loss channel producing $\bullet SiMe_3$ (reaction (4.13)) and the H_2 elimination channel (reaction (4.22)) forming $Me_2Si=CH_2$ are 90.4 kcal/mol and 95.1 kcal/mol, respectively. Combined with Figure 4.4 and 4.8, the overall energy barrier to produce $Me_2Si=CH_2$ from Me_3SiH via reaction (4.22) was around 140 kcal/mol, while the corresponding energy barrier of the tetramethyldisilene channels was around 95 kcal/mol. Therefore, compared to the tetramethyldisilene channels, the secondary reactions of trimethylsilane producing $Me_2Si=CH_2$ were less favored. The secondary reaction of trimethylsilane could also lead to $\bullet SiHMe_2$ at m/z 59 (reaction (4.23)). Although the product signal overlapped with one of the major initiation channels (reaction (4.8)), theoretical calculations indicated that the energy barrier for reaction (4.23) is 82.1 kcal/mol, which is lower than the threshold energy of the H-loss channel. Therefore, this secondary reaction pathway was considered possible.

$$Me_3SiH \xrightarrow{-H_2} Me_2Si=CH_2 \tag{4.22}$$

$$Me_3SiH \xrightarrow{-CH_3} \bullet SiHMe_2 \tag{4.23}$$

The m/z = 54 and 56 peaks were produced by sequential H_2 loss from dimethylsilylene (Me_2Si:). As shown in Figure 4.1, these two peaks started to show up at around 1250 K, which was consistent with the study by Liu et al (1280 K).[29] According to the earlier work, Me_2Si: first isomerized to $MeSi(H)=CH_2$ with an energy barrier of 36.1 kcal/mol, and then converted to :Si(H)Et by 1,2-methyl shift with an energy barrier of 48.0 kcal/mol, and further lost one H_2 leading to $:Si=CHCH_3$. $:Si=CHCH_3$ then isomerized to $:Si(H)CH=CH_2$ with an energy barrier of 27.7 kcal/mol, followed by another H_2 lost forming $:Si=C=CH_2$ (reaction (4.24)).[29]

$$\mathrm{Me_2Si{:}} \leftrightarrow \mathrm{MeSi(H){=}CH_2} \leftrightarrow \mathrm{{:}Si(H)Et} \xrightarrow{-\mathrm{H_2}} \mathrm{{:}Si{=}CHCH_3} \rightarrow \mathrm{{:}Si(H)CH{=}CH_2} \xrightarrow{-\mathrm{H_2}} \mathrm{{:}Si{=}C{=}CH_2} \tag{4.24}$$

The mass peak of m/z = 45 was first observed at 1050 K, and its intensity remained nearly constant as the temperature increased. The appearance of the m/z = 45 peak could also be caused by the methyl loss reaction of dimethylsilane (m/z = 60), which was produced in reaction (4.4). The chemistry involving the species with m/z = 40-44 could be complicated because they could have multiple sources in the overall reactions. The m/z = 44 peak (:Si(H)-CH_3) could be the direct products of reaction (4.12) and (4.18a). Its possible reaction pathways and corresponding energetics were calculated and are presented in Figure 4.9. Methylsilylene (:Si(H)-CH_3) could directly decompose to $SiCH_3$ with one H

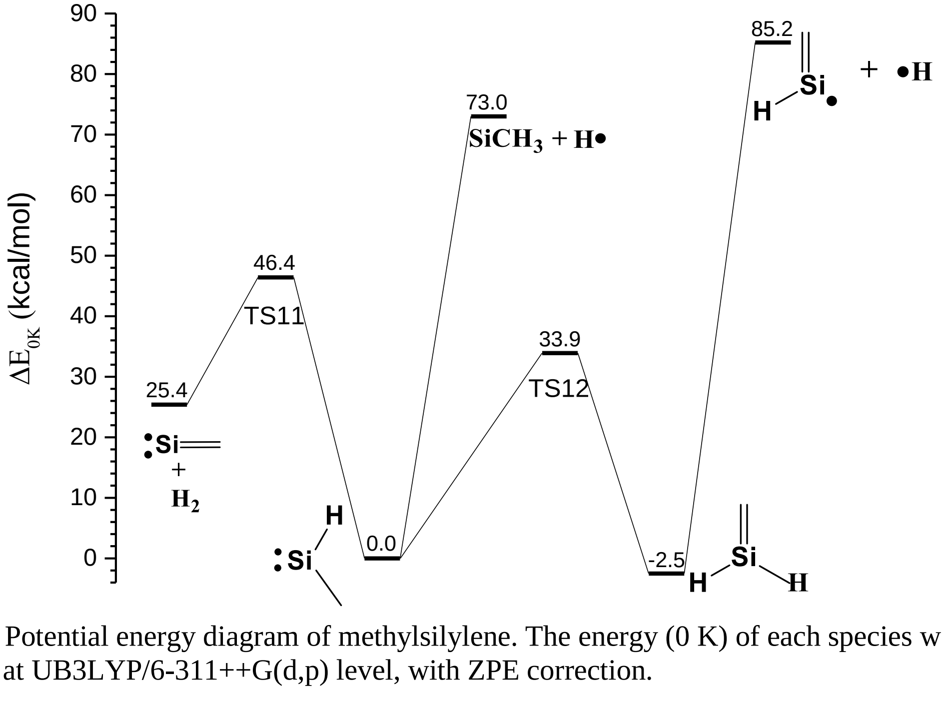

Figure 4.9 Potential energy diagram of methylsilylene. The energy (0 K) of each species were calculated at UB3LYP/6-311++G(d,p) level, with ZPE correction.

loss or isomerize to silene with a 33.9 kcal/mol energy barrier (TS12) followed by H loss with a 87.7 kcal/mol threshold energy. Methylsilylene could also decompose into $:Si=CH_2$ and H_2 over a 46.4 kcal/mol energy barrier. Some previous studies have shown that $:Si=CH_2$ could also be produced by a methane elimination from dimethylsilylene ($:SiMe_2$) with an energy barrier of 56.6 kcal/mol.[29, 40] The m/z = 40 peak did not show up until the temperature reached 1250 K, and it could correspond to SiC which was evolved from an H_2 elimination from $:Si=CH_2$. The sequential H_2 loss from propane (m/z = 44) which was produced from the propane elimination of :Si(H)Pr could also contribute to the signal from m/z = 40-44.[24, 27, 29] The observations of the m/z = 28 peak at 1130 K indicated the formation of Si atom, and it could be produced from the further reaction of SiC.[27, 29]

4.4 Conclusion

The flash pyrolysis of 1,1,2,2-tetramethyldisilane was performed at the temperature ranging from 295 K to 1340 K coupled with molecular beam sampling and VUV-PI-TOF-MS. DFT regarding the energetics of important reactants, transition states, and products were performed at the UB3LYP/6-311++G(d,p) level to support the experimental observations. The four major initiation steps of 1,1,2,2-tetramethyldisilane were the molecular elimination reaction channel leading to dimethylsilane and dimethylsilylene (reaction (4.4)), the Si-Si bond fission producing dimethylsilyl (reaction (4.8)), the production of tetramethyldisilene produced by H_2 elimination (reaction (4.5)), and the decomposition to trimethylsilane and methylsilylene (reaction (4.12)). Theoretical calculations revealed that reaction (4.4) was the most kinetically favored reaction channel among all initiation reactions. Possible isomerization and dissociation channels of tetramethyldisilene were examined theoretically and considered as the source of the

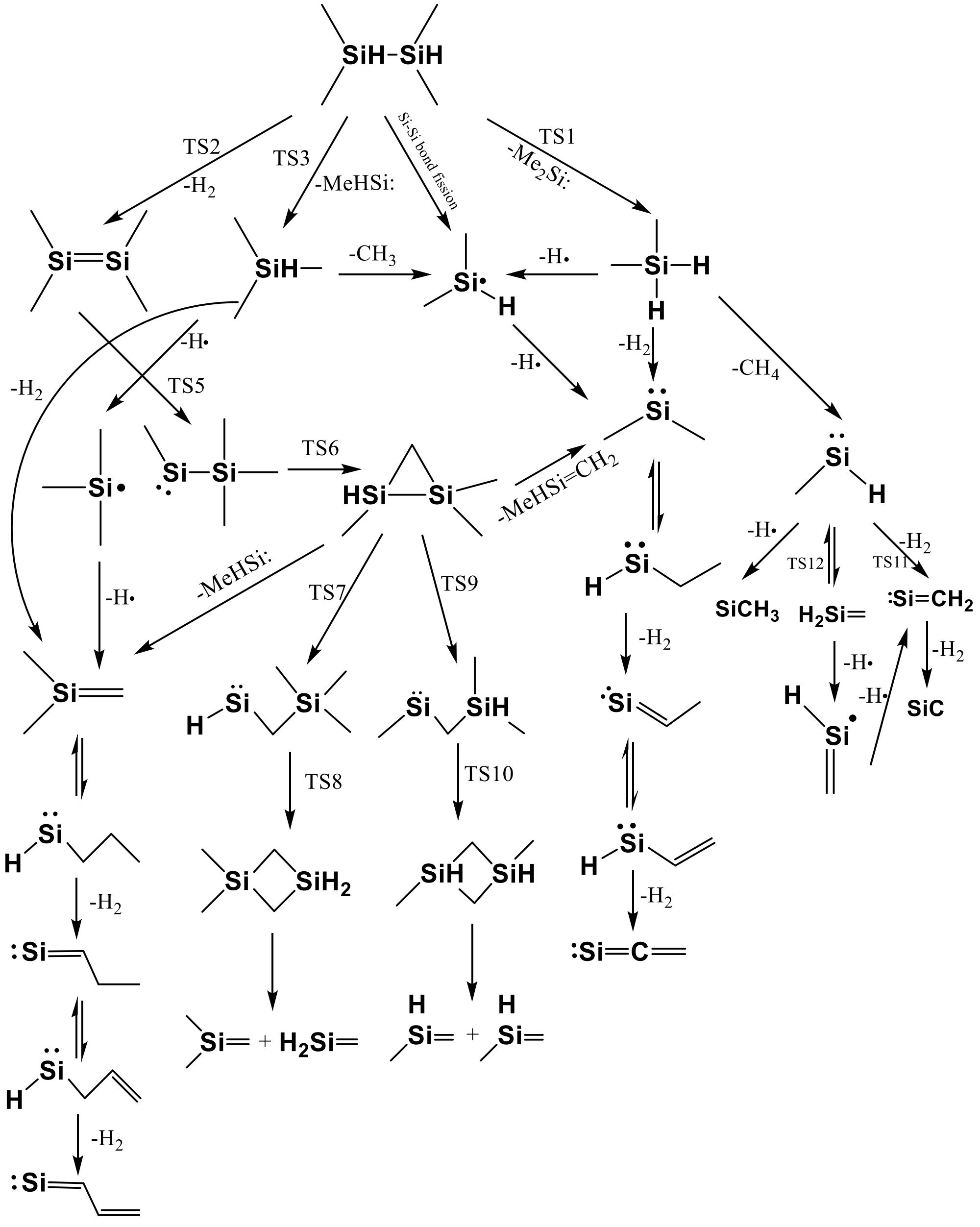

Scheme 4.2 Main reaction mechanism of the pyrolysis of 1,1,2,2-tetramethyldisilane and the corresponding secondary reactions.

observed $Me_2Si=CH_2$ (m/z = 72) and SiC_3H_4 (m/z = 68) mass peaks. The direct dissociation of disilacyclopropane, which was produced by the isomerization of tetramethyldisilene via two transition states, was considered as the major reaction channel for the formation of $Me_2Si=CH_2$ (m/z = 72) and SiC_3H_4 (m/z = 68), while the two 2+2 cycloreversion channels of 1,1-dimethyl-1,3-disilacyclobutane were considered less important. Other secondary reactions, for example, decomposition reactions of trimethylsilane, dimethylsilane and the dimethylsilyl radical, were found, and the results agreed with the previous studies. The overall mechanism of 1,1,2,2-tetramethyldisilane pyrolysis was summarized in Scheme 4.2.

REFERENCE

1. H. Koinuma, M. Funabashi, K. Kishio, M. Kawasaki, T. Hirano and K. Fueki, *Jpn. J. Appl. Phys.*, 1986, **25**, 1811-1814.

2. A. Yoshida, Y. Yamada, T. Nakamura and H. Yonezu, *Thin Solid Films*, 1988, **164**, 213-216.

3. Y. Zhang, X. Cui, F. Shi and Y. Deng, *Chem. Rev.*, 2012, **112**, 2467-2505.

4. M. Suginome and Y. Ito, *J. Am. Chem. Soc.* , 1998, 1925-1934.

5. M. Tobisu, Y. Kita and N. Chatani, *J. Am. Chem. Soc.* , 2006, **128**, 8152-8153.

6. H. Saito, K. Nogi and H. Yorimitsu, *Angew. Chem. Int. Ed.*, 2018, **57**, 11030-11034.

7. I. Titilas, M. Kidonakis, C. Gryparis and M. Stratakis, *Organometallics*, 2015, **34**, 1597-1600.

8. T. Ahrens, T. Braun and B. Braun, *Z. Anorg. Allg. Chem.*, 2014, **640**, 93-99.

9. T. Sanji, H. Ishiwata, T. Kaizuka, M. Tanaka, H. Sakurai, R. Nagahata and K. Takeuchi, *Can. J. Chem.*, 2005, **83**, 646-651.

10. T. Matsuo and N. Hayakawa, *Sci. Technol. Adv. Mater.*, 2018, **19**, 108-129.

11. S. Marutheeswaran, P. D. Pancharatna and M. M. Balakrishnarajan, *Phys. Chem. Chem. Phys.*, 2014, **16**, 11186-11190.

12. Y. Wang, Y. Xie, P. Wei, R. B. King, H. F. Schaefer, P. von R. Schleyer and G. H. Robinson, *Science*, 2008, **321**, 1069-1071.

13. D. N. Roark and G. J. D. Peddle, *J. Am. Chem. Soc.* , 1972, **94**, 5837-5841.

14. W. D. Wulff, W. F. Goure and T. J. Barton, *J. Am. Chem. Soc.* , 1978, **100**, 6236-6238.

15. M. Nag and P. P. Gaspar, *Chem. Eur. J.*, 2009, **15**, 8526-8532.

16. K. Krogh-Jespersen, *J. Am. Chem. Soc.* , 1985, **107**, 537-543.

17. B. H. Boo, S. Im, S. Park and S. Lee, *Organometallics*, 2008, **27**, 2123-2127.

18. M. C. McCarthy, Z. Yu, L. Sari, H. F. Schaefer and P. Thaddeus, *J. Chem. Phys.*, 2006, **124**, 074303 074301-074307

19. K. E. Nares, M. E. Harris, M. A. Ring and H. E. O'Neal, *Organometallics*, 1989, **8**, 1964-1967.

20. R. Walsh, *Organometallics*, 1988, **7**, 75-77.

21. G. W. T. M. J. Frisch, H. B. Schlegel, G. E. Scuseria, M. A. Robb, J. R. Cheeseman, G. Scalmani, V. Barone, B. Mennucci, G. A. Petersson, et al., *Gaussian 09*, (2009), Wallingford, CT.

22. K. Kim and K. D. Jordan, *J. Phys. Chem. A*, 1994, **98**, 10089-10094.

23. P. J. Stephens, F. J. Devlin, C. F. Chabalowski and M. J. Frisch, *J. Phys. Chem. A*, 1994, **98**, 11623-11627.

24. X. Liu, J. Zhang, A. Vazquez, D. Wang and S. Li, *The Journal of Physical Chemistry A*, 2019, **123**, 10520-10528.

25. S. Tajima, D. Watanabe, S. Nakajima, O. Sekiguchi and N. M. M. Nibbering, *J. Mass Spectrom.*, 2002, **37**, 299-304.

26. L. Szepes and T. Baer, *J. Am. Chem. Soc.* , 1984, **106**, 273-278.

27. K. Shao, Y. Tian and J. Zhang, *International Journal of Mass Spectrometry*, 2021, **460**, 116476 116471-116479.

28. R. Toukabri and Y. Shi, *Phys. Chem. Chem. Phys.*, 2014, **16**, 7896-7906.

29. X. Liu, J. Zhang, A. Vazquez, D. Wang and S. Li, *Physical Chemistry Chemical Physics*, 2018, **20**, 18782-18789.

30. Y. J. Shi, X. M. Li, R. Toukabri and L. Tong, *J. Phys. Chem. A*, 2011, **115**, 10290-10298.

31. N. Auner, I. M. T. Davidson, S. Ijadi-Maghsoodi and F. T. Lawrence, *Organometallics,* 1986, **5**, 431-435.

32. G. Maier, H. P. Reisenauer, J. Jung, H. Pacl and H. Egenolf, *Eur. J. Org. Chem.*, 1998, **1998**, 1297-1305.

33. K. Sakamoto, J. Ogasawara, H. Sakurai and M. Kira, *J. Am. Chem. Soc.* , 1997, **119**, 3405-3406.

34. G. W. Schriver, M. J. Fink and M. S. Gordon, *Organometallics*, 1987, **6**, 1977-1984.

35. W. E. W. NIST Mass Spectrometry Data Center, director, NIST Chemistry WebBook, NIST Standard reference database number 69, Eds. P.J. Linstrom and W.G. Mallard, National Institute of Standards and Technology, Gaithersburg MD, 20899, https://webbook.nist.gov/cgi/inchi/InChI=1S/C6H16Si2/c1-7(2)5-8(3,4)6-7/h5-6H2,1-4H3, (retrieved November 2, 2020).

36. I. Badran and Y. J. Shi, *J. Phys. Chem. A*, 2015, **119**, 590-600.

37. M. S. Gordon, T. J. Barton and H. Nakano, *J. Am. Chem. Soc.* , 1997, **119**, 11966-11973.

38. I. Badran, A. Rauk and Y. J. Shi, *J. Phys. Chem. A*, 2012, **116**, 11806-11816.

39. L. E. Gusel'nikov, V. G. Avakyan and S. L. Guselnikov, *J. Am. Chem. Soc.* , 2002, **124**, 662-671.

40. H. Leclercq and I. Dubois, *J. Mol. Spectrosc.*, 1979, **76**, 39-54.

CHAPTER 5 Flash pyrolysis mechanism of trimethylchlorosilane

5.1 Introduction

The preparation of silicon carbide (SiC) by chemical vapor deposition (CVD) is important in industrial processing.[1, 2] A series of chloromethylsilanes ($SiMe_{4-x}Cl_x$) have been considered as suitable CVD precursors,[3, 4] and it therefore becomes important to understand their gas-phase thermal decomposition behaviors. A number of studies have focused on the pyrolysis mechanisms of several $SiMe_{4-x}Cl_x$ species, such as trichloromethylsilane and dichlorodimethylsilane.[3, 5-11] However, there are relatively fewer investigations on the gas-phase thermal decomposition of trimethylchlorosilane. The gas-phase dyotropic arrangement between chloromethyldimethylsilane and trimethylchlorosilane was studied by Martin et al. using a static cell at 636 K to 690 K.[12] It was reported that the isomerization between chloromethyldimethylsilane and trimethylchlorosilane was carried out in two parallel channels, a concerted dyotropic rearrangement and a free radical chain reaction. Davidson et al. examined the pyrolysis mechanisms of trimethylchlorosilane by using a low-pressure pyrolysis technique at temperatures between 1020 K and 1110 K.[13] The reactions were believed to be initiated by Si-C bond rupture (reaction (5.1)), and the main product was determined to be methane, which was proposed to be formed by a bimolecular reaction (reaction (5.2)). The $CH_2SiClMe_2$ radical produced in reaction (5.2) could further undergo dissociation reaction leading to the formation of $ClMeSi{=}CH_2$ and $\bullet CH_3$ (reaction (5.3)). The significant presence of hydrogen chloride was observed, and molecular elimination of HCl (reaction

(5.4)) was proposed as a possible formation channel.[13] With the significant amount of HCl present in the pyrolysis system, several bimolecular reactions involving HCl were identified (reaction (5.5) and (5.6)). Trimethylchlorosilane is known for its extreme sensitivity to moisture. Papanastasiou et al. studied the rate coefficient of the reaction between trimethylchlorosilane and OH radical over the 295-375 K temperature range and showed that trimethylchlorosilane may have a short lifetime in the atmosphere due to its high sensitivity to moisture and radicals.[14]

$$\mathrm{ClSiMe_3 \rightarrow \bullet SiClMe_2 + \bullet Me} \tag{5.1}$$

$$\mathrm{\bullet Me + ClSiMe_3 \rightarrow \bullet CH_2SiClMe_2 + CH_4} \tag{5.2}$$

$$\mathrm{\bullet CH_2SiClMe_2 \rightarrow ClMeSi{=}CH_2 + \bullet Me} \tag{5.3}$$

$$\mathrm{ClSiMe_3 \rightarrow Me_2Si{=}CH_2 + HCl} \tag{5.4}$$

$$\mathrm{ClMeSi{=}CH_2 + HCl \rightarrow Me_2SiCl_2} \tag{5.5}$$

$$\mathrm{\bullet SiClMe_2 + HCl \rightarrow Me_2SiCl_2 + \bullet H} \tag{5.6}$$

Among the $\mathrm{SiMe_{4-x}Cl_x}$ compounds mentioned above [4, 6-13, 15-18], the pyrolysis mechanism of trimethylchlorosilane was less studied. Furthermore, as discussed by Davidson et al., HCl was always present in the pyrolysis system, but its formation mechanism was not completely clear.[13] Therefore, studying the initiation reactions in the thermal decomposition of trimethylchlorosilane, especially on the formation mechanism of HCl, is informative. We describe here an investigation on the flash pyrolysis mechanism of trimethylchlorosilane using a SiC microreactor coupled with vacuum ultraviolet photoionization time-of-flight mass spectrometer (VUV-PI-TOFMS) under predominantly unimolecular reaction conditions. The detection of the early reaction products and reactive intermediates at elevated temperatures provided insights into how the dissociation reaction of trimethylchlorosilane was initiated. Quantum chemistry calculations were also employed to study the energetics of possible initiation channels. The experimental evidence for the HCl molecular elimination channel of trimethylchlorosilane leading to the production of dimethylsilene ($Me_2Si=CH_2$) and HCl (the HCl elimination channel) was found, and the conclusion was supported by the theoretical calculations. Other important initiation reactions and secondary reactions were also examined. A comprehensive decomposition mechanism of trimethylchlorosilane was developed.

5.2 Experimental and computational methods

The trimethylchlorosilane precursor (≥ 99 %) was purchased from Sigma Aldrich. Precaution was taken during the sample introduction process as trimethylchlorosilane is extremely sensitive to moisture, and it could lead to the production of hexamethyldisiloxane as a major impurity. The liquid sample of trimethylchlorosilane was taken out by a glass syringe and introduced to a bubbler filled with helium gas in a glove box. The mass spectrum showed that the contamination of hexamethyldisiloxane was negligible. The precursor was diluted to ~3.7 % in the helium carrier gas at a total pressure of ~970 torr.

Quantum chemistry calculations were performed in addition to the experimental investigations. The energetics of the reactants, products, and transition states involved in the trimethylchlorosilane pyrolysis were calculated. Density functional theory (DFT) calculations for geometry optimizations and zero-point energies were performed at the UM05-2X/aug-cc-pVDZ level of theory, as it was recommended by Sirianni et al.[19] for the geometry optimizations of bimolecular van der Waals complexes identified in this work. The single-point energy calculations were obtained at the UCCSD(T)/cc-pVTZ level, as similar methods have been widely used in benchmark calculations of silane systems.[20] For the zero-point energy calculations, all the zero-point vibrational frequencies were scaled by a factor of 0.9725 as recommended by Laury et al.[21] to account for overestimations in the vibrational frequency calculations. Transition states in this work were verified by IRC running calculation at the UM05-2X/aug-cc-pVDZ level of theory. All the computations in this work were carried out using the Gaussian 16 package.[22]

Unimolecular reaction rate constants of the initiation reactions were calculated using transition state theory (TST). For the unimolecular dissociation reaction with a conventional transition state, the rate constant was calculated using TST with Wigner tunneling correction.[23-26] The single point energy and frequencies of reactants and transition states were obtained from DFT calculations at the UM05-2X/aug-cc-pVDZ level of theory using the Gaussian 16 package as described before.[22] For the bond homolysis (barrierless) reactions, variational transition state theory (VTST) with Wigner tunneling correction was applied.[23-27] A series of constrained optimizations along the reaction path were carried out, and at each optimized geometry (“trial transition state”), the potential energy and vibrational frequencies were calculated. The dividing surface for the barrierless reactions at different temperatures were determined by finding the maximum Gibbs free energy change $\Delta G^{\ominus}(T)$ of the “trail transition state” along the reaction pathway at the different temperatures.[27] All the rate constant calculations were performed using the KISTHELP program.[25, 28, 29]

5.3 Results and discussion

The pyrolysis mass spectra of trimethylchlorosilane at temperatures ranging from 295 K to 1400 K are shown in Figure 5.1 and Figure 5.2. At 295 K, the m/z = 108, 109, and 110 peaks represented the parent molecule trimethylchlorosilane ($ClSiMe_3$). The relative natural abundance for ^{35}Cl and ^{37}Cl are 76 % and 24 %, and the relative abundance for ^{28}Si, ^{29}Si, and ^{30}Si are 92.2 %, 4.7 %, and 3.1 %.[30] The ratio of peak area of m/z = 108 to m/z = 110 is determined to be 2.56 based on Figure 5.1, which is close to the theoretical

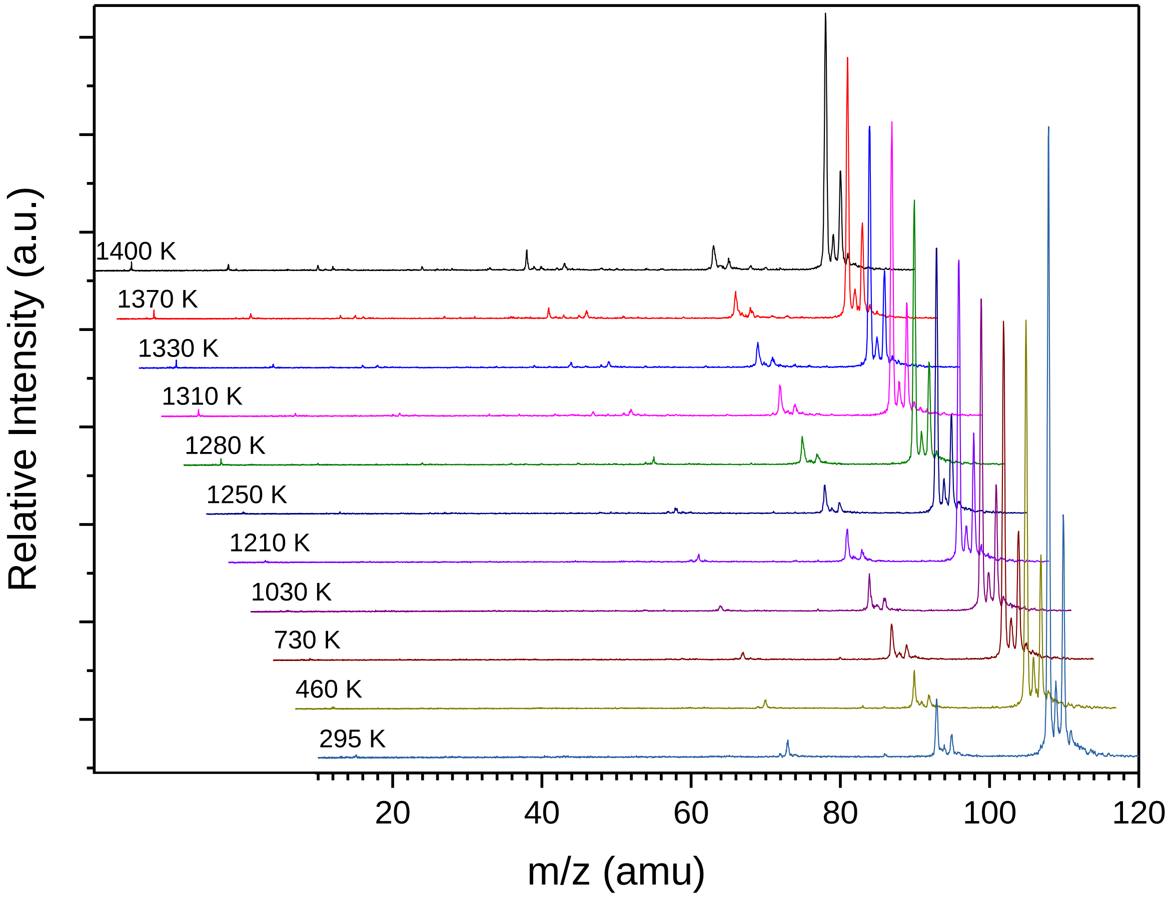

Figure 5.1 Mass spectra of the chlorotrimethylsilane pyrolysis at 295 K to 1400 K. The mass spectra are offset for clarity.

value of 2.86. Other peaks at 295 K, such as m/z = 73, 95, and 97, were caused by photoionization fragmentation of the parent molecule. At 295 K, the signal of m/z = 72 was not caused by photoionization of neutral $Me_2Si=CH_2$ molecule as the parent molecule could not readily decompose at room temperature. But it was not likely caused by photoionization fragmentation of the parent molecule, as the m/z = 72 signal was not observed in the electron impact spectra of trimethylchlorosilane.[31] The m/z = 72 peak was probably caused by ionization fragments of the very minor parent molecule clusters formed in the molecular beam (which was possible after supersonic cooling of room temperature gas sample). This was consistent with its temperature dependence; when the temperature increased to 460 K, which was not high enough to induce thermal dissociation reactions but sufficient to destroy the molecule clusters in the molecular beam, the m/z = 72 signal disappeared. A very minor peak at m/z = 88 was probably an impurity in the liquid sample, as its signal kept minor and nearly constant throughout all temperatures and could be treated as a spectator at all temperatures.

(a) The HCl molecular elimination channel forming $Me_2Si=CH_2$.

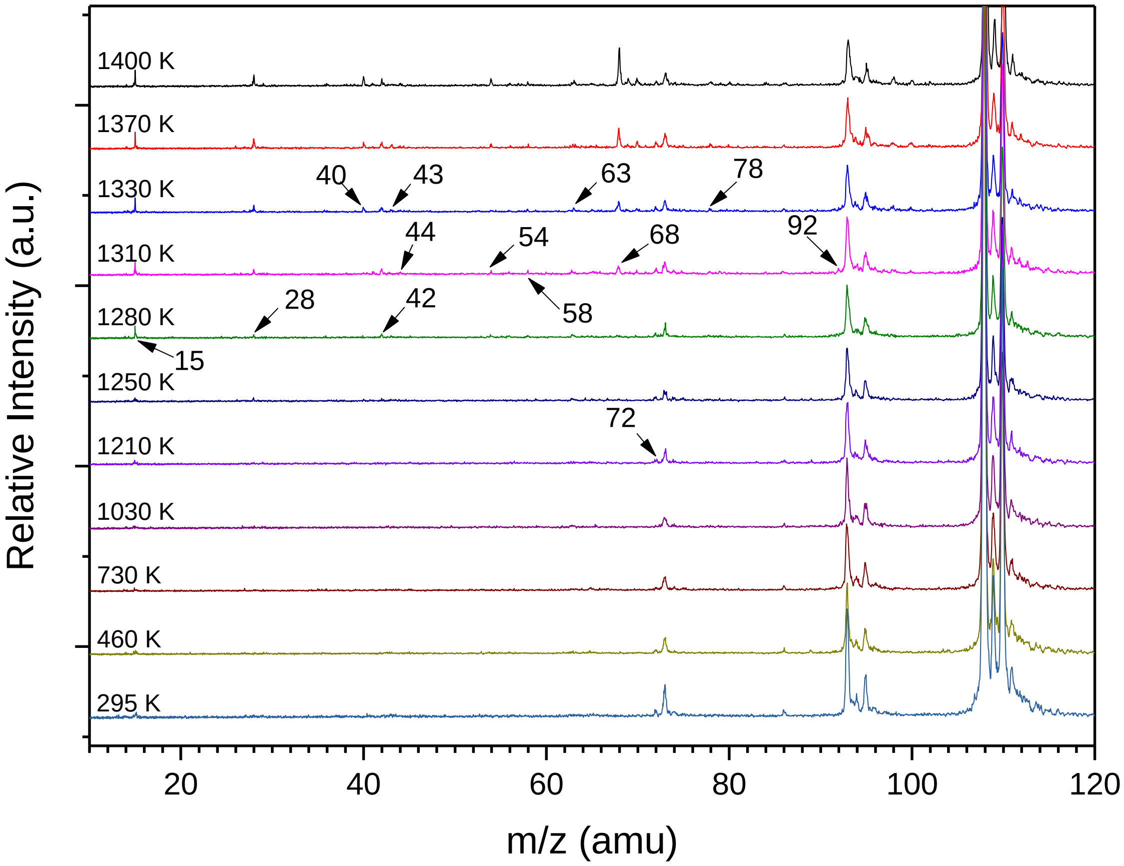

Figure 5.2 Mass spectra of the chlorotrimethylsilane pyrolysis at 295 K to 1400 K. The spectra were enlarged to identify the peaks of smaller fragments. The mass spectra are offset for clarity.

As shown in Figure 5.1 and 5.2, the m/z = 72 peak was first observed at 295 K. However, as discussed earlier, it was likely caused by the ionization of molecule clusters in the molecular beam. The signal of the m/z = 72 peak reappeared at 1210 K, and its intensity was nearly constant until reaching 1400 K. This indicated that $Me_2Si=CH_2$ was formed via the HCl elimination channel (reaction (5.4)) of the parent molecule. The appearance of the m/z = 68 peak also served as evidence for the presence of $Me_2Si=CH_2$, as the SiC_3H_4 species was readily produced by secondary reactions of $Me_2Si=CH_2$

according to previous studies.[32, 33] The counter fragment of the elimination reaction, HCl, was not observed since its ionization potential of 12.79 eV[34] is higher than the photon energy of the 118 nm (10.49 eV) laser radiation. As will be discussed later, trimethylsilyl radical losing one hydrogen atom forming $Me_2Si{=}CH_2$ was considered to be negligible (as the production of Cl and $\bullet SiMe_3$ from the parent molecule was very small).

Quantum chemistry calculations on the energetics of the initiation reactions of trimethylchlorosilane were summarized in Figure 5.3. The HCl molecular elimination channel was determined to have the lowest energy barrier. Trimethylchlorosilane overcomes an energy barrier (TS2) of 75.4 kcal/mol and forms a van der Waals complex at an energy of 71.2 kcal/mol relative to Me_3SiCl. The van der Waals complex may further decompose into $Me_2Si{=}CH_2$ and HCl (at an energy of 75.2 kcal/mol). Overall, $Me_2Si{=}CH_2$ and HCl can be viewed to be formed via TS2 with a 75.4 kcal/mol energy barrier. Compared to other possible initiation channels, the HCl elimination channel has the lowest energy barrier and is the most energetically favored.

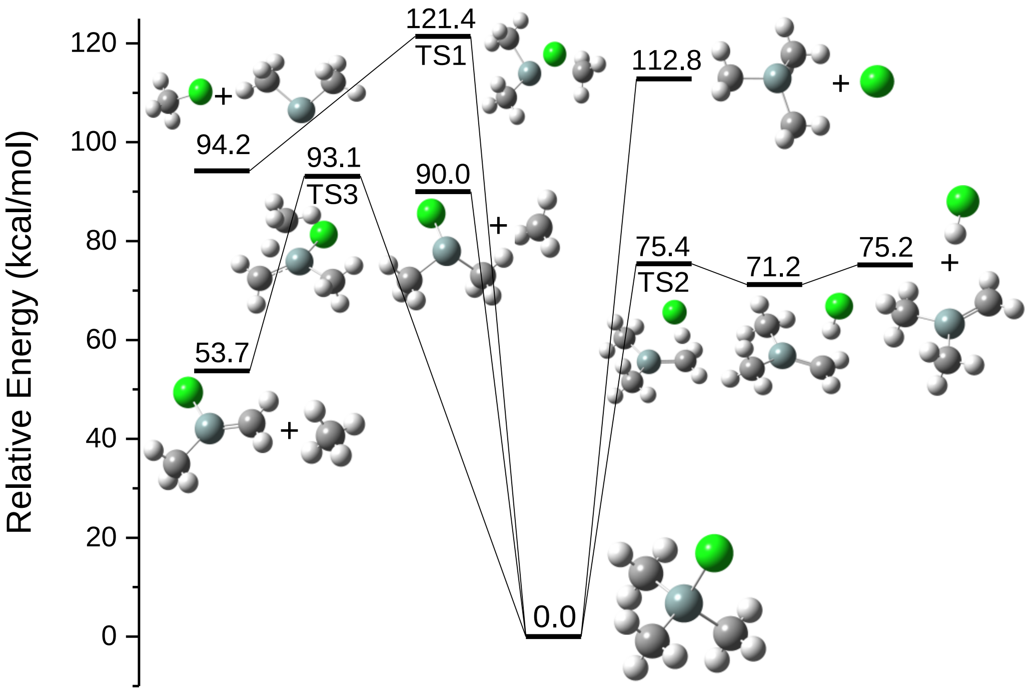

Figure 5.3 Energetics (0 K) of the possible initiation channels for the pyrolysis of trimethylchlorosilane at the UCCSD(T)/cc-pVTZ//UM05-2X/aug-cc-pVDZ level.

(b) Other initiation channels.

Two other possible initiation channels of the trimethylchlorosilane pyrolysis are the CH_3 loss channel (reaction (5.1)) and the Cl loss channel (reaction (5.7)). According to Figure 5.1 and 5.2, the m/z = 73 (•$SiMe_3$) and the m/z = 93 (•$Si^{35}ClMe_2$) and 95 (•$Si^{37}ClMe_2$) signals appeared as photoionization fragmentation peaks at room temperature. With the increase of temperature, the peak intensities remained nearly constant, suggesting that the thermal decomposition contributions to the signal were trivial. The ratio of peak area for m/z 93/108 and 73/108 (where the parent peak was at m/z 108) were plotted in Figure 5.4. It shows that the curve remained nearly flat when the temperature increased, and no significant increase of the curve was observed. The m/z =

15 signal for the methyl radical was first observed at 1280 K, which suggested that the onset temperature for reaction (5.1) was around 1280 K. The onset temperature for reaction (5.1) was higher than that of reaction (5.4), indicating that reaction (5.1) was less significant. Also based on the energetics calculations in Figure 5.3, the CH_3 loss channel has an energy threshold of 90.0 kcal/mol, while the threshold energy for the Cl loss channel was determined to be 112.8 kcal/mol; both were much higher than the HCl molecular elimination channel (reaction (5.4)), but the CH_3 loss channel (5.1) was more thermodynamically favored than the Cl loss channel (5.7).

$$ClSiMe_3 \rightarrow \bullet SiMe_3 + \bullet Cl \tag{5.7}$$

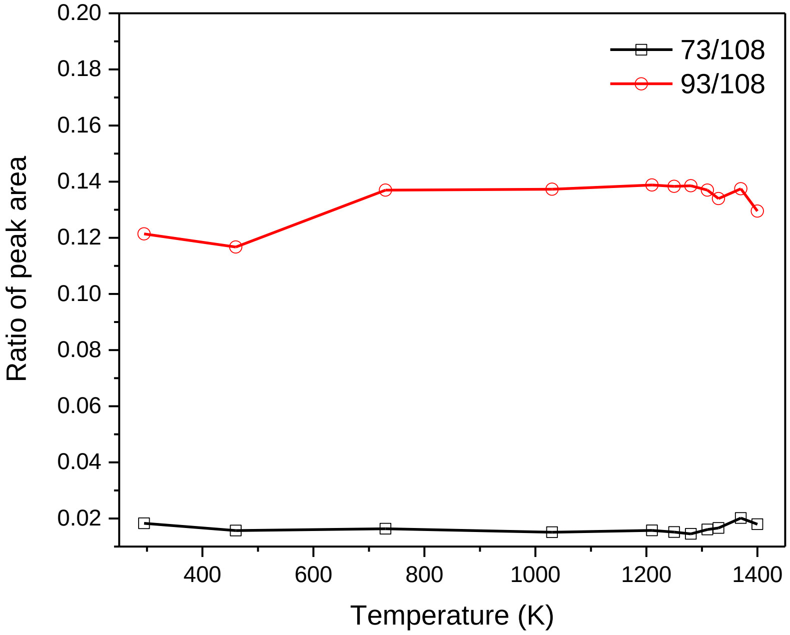

Figure 5.4 The plot of the m/z = 73 and 93 peak area over m/z = 108 peak area in the temperature range from 295 K to 1400 K.

A very minor peak of m/z = 92 appeared at 1310 K, suggesting the production of $ClMeSi=CH_2$, and it disappeared as the temperature further increased. $ClMeSi=CH_2$ was probably formed by the methane elimination reaction of $ClSiMe_3$ (reaction (5.8), the CH_4 elimination channel) or the hydrogen loss reaction of $\bullet SiClMe_2$ (reaction (5.9)). In Figure 5.3, the formation of $MeClSi=CH_2$ and CH_4 was the most thermodynamically favored pathway with a relative energy of 53.7 kcal/mol, although kinetically the energy barrier via TS3 (93.1 kcal/mol) is still much higher than that of TS2. The CH_4 elimination pathway (reaction (5.8)) was considered minor because of its higher energy barrier. Similarly, secondary loss of one hydrogen atom by $\bullet SiClMe_2$ (produced from reaction (5.1)) could also lead to the formation of the m/z = 92 peak. According to Davidson et al.,[13] $ClMeSi=CH_2$ was formed from secondary dissociations of $\bullet CH_2Si(Cl)Me_2$ (reaction (5.3)), which was produced from a series of bimolecular reactions. However, since the signal of $\bullet CH_2SiClMe_2$ was not detected (Figure 5.1 and 5.2), bimolecular reactions were greatly minimized, and the contribution of reaction (5.3) to the appearance of the m/z = 92 peak and the methyl radical was also considered trivial.

$$ClSiMe_3 \rightarrow MeClSi=CH_2 + CH_4 \qquad (5.8)$$

$$\bullet Si(Cl)Me_2 \rightarrow MeClSi=CH_2 + \bullet H \qquad (5.9)$$

(c) Unimolecular reaction rate constant calculations for the initiation reactions.

The unimolecular reaction rate constants of the above-mentioned initiation reactions at different temperatures were calculated using the TST/VTST theory and are summarized in Figure 5.5 and 5.6 (more information on the unimolecular reaction rate constant calculations is provided in the Supplementary Materials). At low temperatures (~ 1200 K), the HCl elimination channel is the most kinetically favored pathway. As the temperature further increased (above ~ 1300 K), the CH_3 loss channel started to become significant, while the reaction rate constants for the other three reaction channels remained relatively small. Although there were distributions of temperature in the microreactor, one could still compare the calculated unimolecular reaction rate constants of competing reactions (using the temperature measured in the center region of the microreactor) to determine the relative importance of each reaction. The results of the rate calculations are consistent with the calculated reaction energetics (Figure 5.3) and the experimental observations.

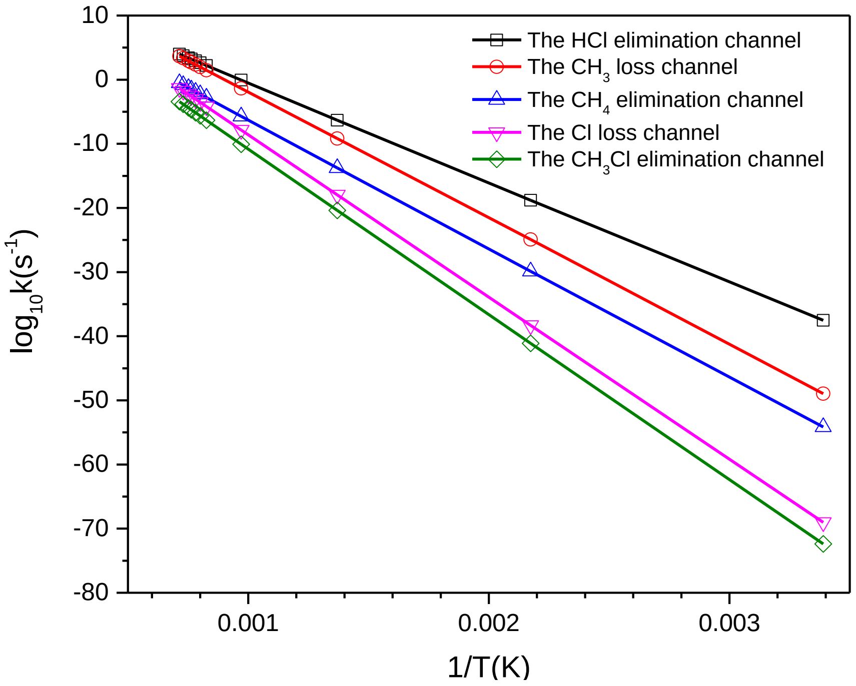

Figure 5.5 The unimolecular rate constant calculations of all the initiation reactions with the TST/VTST method. The results are displayed in the form of $\log_{10}k$ vs 1/T.

As shown in Figure 5.6, the calculated rate constant for the HCl elimination channel remained almost constant until around 1050 K and was found to significantly increase at around 1210 K and above. This is consistent with the experimental observation that the signal of $Me_2Si=CH_2$ (m/z = 72) was first found at around 1210 K. The calculated rate constant for the CH_3 loss channel showed a similar trend at higher temperatures. The rate constant for the CH_3 loss channel increased significantly around 1280 K and kept increasing sharply as the temperature further increased. This is also consistent with the first appearance of the m/z = 15 signal at 1280 K, which indicated that the onset temperature of the Si-C bond fission was around 1280 K.

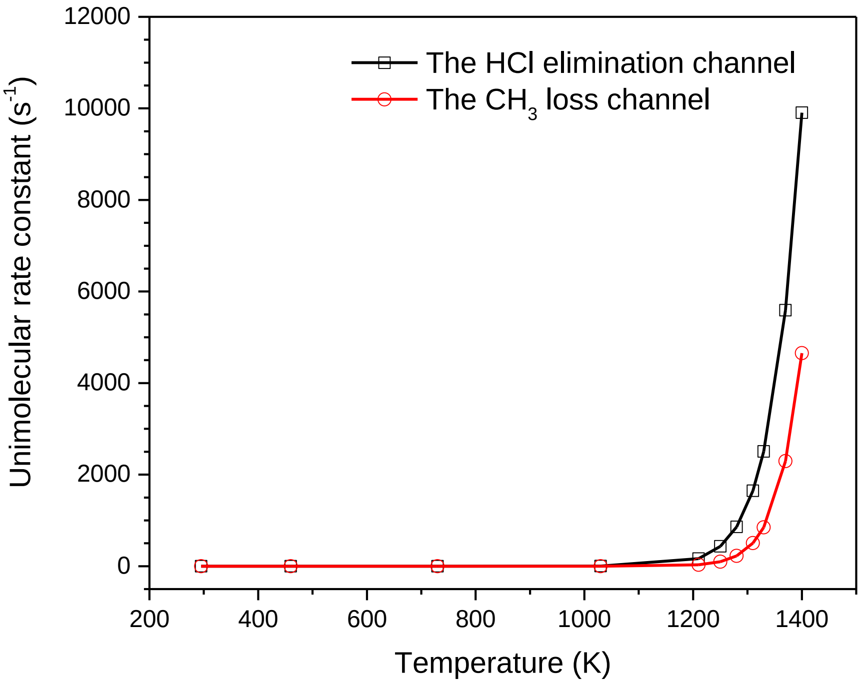

Figure 5.6 The unimolecular rate constant calculations of the HCl elimination channel and the CH_3 loss channel with the TST/VTST method.

As indicated in Figure 5.5, compared to the HCl elimination and CH_3 loss channels, the calculated rate constants for the CH_4 elimination channel, the Cl loss channel, and the CH_3Cl elimination channel were significantly smaller. For example, the rate constant for the CH_4 elimination channel at 1400 K was 0.3 s^{-1} and that for the Cl loss channel at 1400 K was 0.05 s^{-1}, while the rate constant for the HCl elimination channel at the lower temperature of 1210 K was 165 s^{-1}, which is three or more order of magnitude larger. And this is consistent with the experimental observations that the HCl elimination channel and the CH_3 loss channel are more significant than the other initiation reaction pathways.

(d) Secondary reactions.

Evidence for the occurrences of secondary reactions was also observed and was found to be consistent with the previous experimental and theoretical studies.[18, 32, 33, 35] At 1310 K, the m/z = 68 and 70 peaks were first observed. According to Shao et al.[18] and Liu et al.,[32] the SiC_3H_6 and SiC_3H_4 species were produced by sequential dehydrogenation reactions of $Me_2Si{=}CH_2$ (reaction (5.10)-(5.12)). Liu et al. investigated the energetics of the secondary reactions of $Me_2Si{=}CH_2$ in detail at the UB3LYP/6-311++G(d,p) level of theory.[32] According to Liu et al., the overall energy barrier of the multistep isomerization channel from $Me_2Si{=}CH_2$ to $:Si(H)C_3H_7$ (reaction (5.10)) is 62.6 kcal/mol relative to $Me_2Si{=}CH_2$. The H_2 elimination of $:Si(H)C_3H_7$ producing $:Si{=}CHCH_2CH_3$ (reaction (5.11)) was identified as the most energetically favored pathway for the appearance of the m/z = 70 peak, with an energy barrier of 65.4 kcal/mol relative to $Me_2Si{=}CH_2$. $:Si{=}CHCH_2CH_3$ could further lose an H_2 forming $:Si{=}CHCH{=}CH_2$ (m/z = 68) with a total threshold energy of 57.9 kcal/mol (reaction (5.12)). $:Si(H)C_3H_7$ could also directly dissociate to Si and C_3H_8 (m/z = 44) with an energy barrier of 58.2 kcal/mol (reaction (5.13)). This is consistent with the mass spectra in Figure 5.2, where the m/z = 44 peak first appeared at 1310 K.

$$Me_2Si{=}CH_2 \rightarrow :Si(H)C_3H_7 \tag{5.10}$$

$$:Si(H)C_3H_7 \rightarrow :Si{=}CHCH_2CH_3 + H_2 \tag{5.11}$$

$$:Si{=}CHCH_2CH_3 \rightarrow :Si{=}CHCH{=}CH_2 + H_2 \tag{5.12}$$

$$:Si(H)C_3H_7 \rightarrow Si + C_3H_8 \tag{5.13}$$

At 1310 K, the signals of m/z = 58, 56, and 54 were detected, which corresponded to $:SiMe_2$, SiC_2H_4, and SiC_2H_2 respectively. However, these peak intensities were very small. As the temperature further increased, the signal of m/z = 58 and 56 turned trivial, while the signal of m/z = 54 remained nearly constant. The formation of $:SiMe_2$ might be caused by the chlorine loss reaction of $SiClMe_2$, or the methyl loss reaction of $SiMe_3$. According to Figure 5.4 and the discussions above, the secondary reactions of $\bullet SiClMe_2$ leading to $:SiMe_2$ were more likely to take place, since reaction (5.1) was more energetically favored than reaction (5.7). After the formation of $:SiMe_2$, dehydrogenation reactions started to take place which led to the m/z = 56 peak (reaction (5.14)).[18, 32] According to Liu et al., the threshold energy for reaction (5.14) was 56.4 kcal/mol. $:Si{=}CHCH_3$ could further lose one H_2 and decompose to $:Si{=}C{=}CH_2$ (reaction (5.15)). Its threshold energy was calculated to be 44.1 kcal/mol relative to $:Si{=}CHCH_3$.[32] The possible secondary reaction product from the secondary decomposition of $SiClMe_2$ (reaction

(5.16)), :SiClMe (m/z = 78), was first observed at 1330 K, and the signal of m/z = 63 ($Si^{35}Cl$) was detected at 1330 K, which suggested further secondary reactions of :SiClMe. The isotopic signal of m/z = 65 ($Si^{37}Cl$) was hardly observed due to its small peak intensity. SiCl could further lose a Cl atom forming Si, although the signal of Si (m/z = 28) could evolve from multiple sources.

$$:SiMe_2 \rightarrow :Si{=}CHCH_3 + H_2 \tag{5.14}$$

$$:Si{=}CHCH_3 \rightarrow :Si{=}C{=}CH_2 + H_2 \tag{5.15}$$

$$SiClMe_2 \xrightarrow{-CH_3} :SiClMe \xrightarrow{-CH_3} SiCl \tag{5.16}$$

At 1280 K, the signal of m/z = 42 was detected, and when the temperature increased to 1330 K, the m/z = 40 peak was observed. The peak m/z = 40 and 42 signals remained constant as the temperature increased. The m/z = 42 peak corresponds to $Si{=}CH_2$ or C_3H_6, and the m/z = 40 peak represents SiC. The m/z = 42 signal at 1280 K was likely produced by the methane elimination mechanism from $:SiMe_2$ (reaction (5.17)) with an energy barrier of 56.6 kcal/mol according to Liu et al..[32] Alternatively, it could be evolved from the secondary decompositions of $:Si{=}CHCH_2CH_3$ (reaction (5.18)), and this is consistent with the appearance of m/z = 28 signal (Si) at 1280 K.

$$:SiMe_2 \xrightarrow{-CH_4} :Si{=}CH_2 \tag{5.17}$$

$$:Si{=}CHCH_2CH_3 \rightarrow Si + C_3H_6 \tag{5.18}$$

The appearance of the small m/z = 98, 100, and 102 (:$SiCl_2$) peaks at 1330 K might be associated with some very minor bimolecular reactions at high temperatures between HCl and the parent molecule $ClSiMe_3$. The HCl, which was produced in abundancy in reaction (5.4), reacted with $ClSiMe_3$ and produced Cl_2SiMe_2 (reaction (5.19)). Then, further decomposition of Cl_2SiMe_2 at high temperatures led to the formation of the $SiCl_2$ species.[6] In this work, the signal of the $SiCl_2$ species was much smaller than that in the previous study of the Cl_2SiMe_2 pyrolysis,[6] suggesting that the production of Cl_2SiMe_2 and $SiCl_2$ species were insignificant under the predominantly unimolecular reaction conditions.

$$HCl + ClSiMe_3 \rightarrow Cl_2SiMe_2 + CH_4 \tag{5.19}$$

Reaction (5.19) might need further attention, although it was found insignificant in this work. The quantum chemistry calculations were performed at the UCCSD(T)/cc-pVTZ//UM05-2X/aug-cc-pVDZ level of theory and are displayed in Figure 5.7. It shows that reaction (5.19) is exothermic and has an energy barrier of 48.8 kcal/mol, which indicates that reaction (5.19) was the most kinetically and thermodynamically favored pathway in this system. This previously ignored reaction pathway might have played an important role in the study by Davidson et al.,[13] since it might be another significant bimolecular reaction pathway leading to the major product, methane.

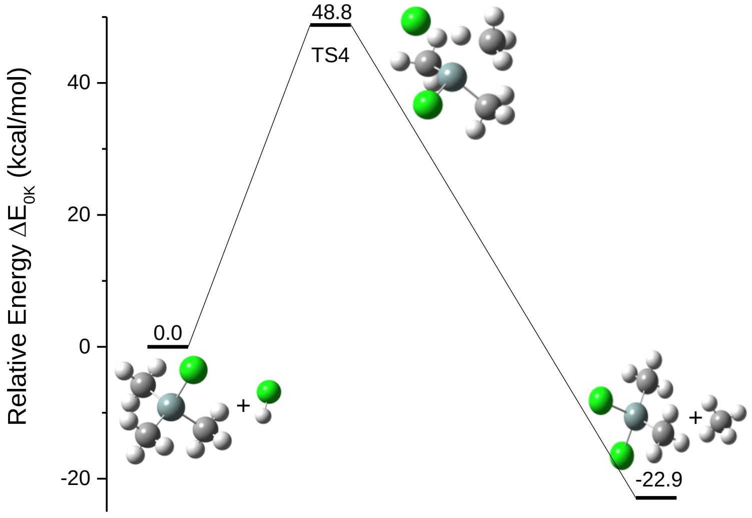

Figure 5.7 Energetics (0 K) of the bimolecular reaction between trimethylchlorosilane and HCl at the UCCSD(T)/cc-pVTZ//UM05-2X/aug-cc-pVDZ level.

4.4 Conclusion

The thermolysis of trimethylchlorosilane was studied by flash pyrolysis coupled with molecular beam sampling and VUV-SPI-TOFMS in this work. The quantum chemistry calculations regarding the energetics of several initiation reaction products were performed. The main decomposition mechanism was summarized in Scheme 5.1. The HCl molecular elimination channel of the parent molecule producing HCl and $Me_2Si=CH_2$ via a van der Waals intermediate was identified as the predominant pathway. The onset temperature for this reaction was determined to be around 1210 K. The CH_3 loss channel was also observed, and its onset temperature was determined to be around 1280 K. Other possible initiation channels such as the CH_4 elimination channel and the Cl loss channel were less significant. The quantum chemistry calculations and the TST/VTST calculations of the unimolecular reaction rate constants revealed that the HCl elimination channel was the most favorable pathway, which was in consistence with the experimental observations.

Several secondary reaction products have been observed and their formation mechanisms were identified. The secondary reaction of $Me_2Si=CH_2$ leading to the formation of the m/z = 70 and m/z = 68 signals were also discussed. The secondary reaction products of other species such as $SiMe_2Cl$ or $:SiMe_2$ were also identified. The appearance of the $SiCl_2$ signals at high temperatures was believed to be involved with some minor bimolecular reactions between the main initial product HCl and the parent molecule $ClSiMe_3$.

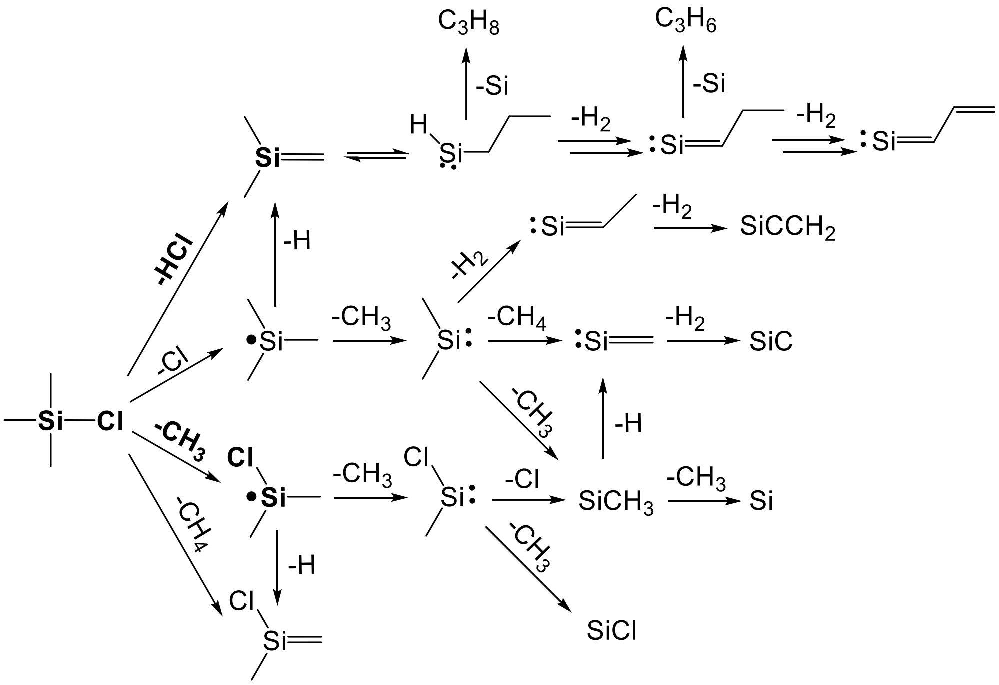

Scheme 5.1 The overall decomposition mechanisms of trimethylchlorosilane, which include the initiation reactions and the secondary reactions. The prominent decomposition pathways are marked in bold.

REFERENCE

1. G. Aresta, J. Palmans, M. C. M. v. d. Sanden and M. Creatore, *Journal of Vacuum Science & Technology A*, 2012, **30**, 041503.

2. M. B. J. Wijesundara and R. G. Azevedo, in *Silicon carbide microsystems for harsh environments*, Springer New York, New York, NY, 2011, pp. 33-95.

3. Y. Funato, N. Sato, Y. Fukushima, H. Sugiura, T. Momose and Y. Shimogaki, *ECS Journal of Solid State Science and Technology*, 2017, **6**, P399-P404.

4. B. J. Choi, *Journal of Materials Science Letters*, 1997, **16**, 33-36.

5. T. M. Besmann, B. W. Sheldon, T. S. Moss III and M. D. Kaster, *Journal of the American Ceramic Society*, 1992, **75**, 2899-2903.

6. J. M. Lemieux and J. Zhang, *European Journal of Mass Spectrometry*, 2014, **20**, 409-417.

7. D. E. Cagliostro, S. R. Riccitiello and M. G. Carswell, *Journal of the American Ceramic Society*, 1990, **73**, 607-614.

8. F. Loumagne, F. Langlais and R. Naslain, *Journal of Crystal Growth*, 1995, **155**, 198-204.

9. F. Loumagne, F. Langlais and R. Naslain, *Journal of Crystal Growth*, 1995, **155**, 205-213.

10. G. D. Papasouliotis and S. V. Sotirchos, *Journal of Materials Research*, 2011, **14**, 3397-3409.

11. S. H. Mousavipour, V. Saheb and S. Ramezani, *The Journal of Physical Chemistry A*, 2004, **108**, 1946-1952.

12. J. G. Martin, M. A. Ring and H. E. O'Neal, *Organometallics*, 1986, **5**, 1228-1230.

13. I. M. T. Davidson and C. E. Dean, *Organometallics*, 1987, **6**, 966-969.

14. D. K. Papanastasiou, F. Bernard and J. B. Burkholder, *International Journal of Chemical Kinetics*, 2020, **52**, 221-226.

15. Y. Ge, M. S. Gordon, F. Battaglia and R. O. Fox, *The Journal of Physical Chemistry A*, 2010, **114**, 2384-2392.

16. Y. Ge, M. S. Gordon, F. Battaglia and R. O. Fox, *The Journal of Physical Chemistry A*, 2007, **111**, 1462-1474.

17. Y. Ge, M. S. Gordon, F. Battaglia and R. O. Fox, *The Journal of Physical Chemistry A*, 2007, **111**, 1475-1486.

18. K. Shao, Y. Tian and J. Zhang, *International Journal of Mass Spectrometry*, 2021, **460**, 116476-116484.

19. D. A. Sirianni, A. Alenaizan, D. L. Cheney and C. D. Sherrill, *Journal of Chemical Theory and Computation*, 2018, **14**, 3004-3013.

20. M. Cypryk and B. Gostyński, *J Mol Model*, 2016, **22**, 35.

21. M. L. Laury, S. E. Boesch, I. Haken, P. Sinha, R. A. Wheeler and A. K. Wilson, *J Comput Chem*, 2011, **32**, 2339-2347.

22. M. J. Frisch, G. W. Trucks, H. B. Schlegel, G. E. Scuseria, M. A. Robb, J. R. Cheeseman, G. Scalmani, V. Barone, G. A. Petersson, H. Nakatsuji, X. Li, M. Caricato, A. V. Marenich, J. Bloino, B. G. Janesko, R. Gomperts, B. Mennucci, H. P. Hratchian, J. V. Ortiz, A. F. Izmaylov, J. L. Sonnenberg, Williams, F. Ding, F. Lipparini, F. Egidi, J. Goings, B. Peng, A. Petrone, T. Henderson, D. Ranasinghe, V. G. Zakrzewski, J. Gao, N. Rega, G. Zheng, W. Liang, M. Hada, M. Ehara, K. Toyota, R. Fukuda, J. Hasegawa, M. Ishida, T. Nakajima, Y. Honda, O. Kitao, H. Nakai, T. Vreven, K. Throssell, J. A. Montgomery Jr., J. E. Peralta, F. Ogliaro, M. J. Bearpark, J. J. Heyd, E. N. Brothers, K. N. Kudin, V. N. Staroverov, T. A. Keith, R. Kobayashi, J. Normand, K. Raghavachari, A. P. Rendell, J. C. Burant, S. S. Iyengar, J. Tomasi, M. Cossi, J. M. Millam, M. Klene, C. Adamo, R. Cammi, J. W. Ochterski, R. L. Martin, K. Morokuma, O. Farkas, J. B. Foresman and D. J. Fox, *Gaussian 16 Rev. C.01,* (2016), Wallingford, CT.

23. D. G. Truhlar, B. C. Garrett and S. J. Klippenstein, *The Journal of Physical Chemistry*, 1996, **100**, 12771-12800.

24. E. Wigner, *Transactions of the Faraday Society*, 1938, **34**, 29-41.

25. S. Canneaux, F. Bohr and E. Henon, *Journal of computational chemistry*, 2014, **35**, 82-93.

26. A. W. Jasper, J. A. Miller and S. J. Klippenstein, *The Journal of Physical Chemistry A*, 2013, **117**, 12243-12255.

27. M. A. Ali, *Scientific Reports*, 2020, **10**, 10995.

28. S. Mohandas, R. O. Ramabhadran and S. S. Kumar, *The Journal of Physical Chemistry A*, 2020, **124**, 8373-8382.

29. S. Begum and R. Subramanian, *RSC Advances*, 2015, **5**, 39110-39121.

30. J. Meija, B. Coplen Tyler, M. Berglund, A. Brand Willi, P. De Bièvre, M. Gröning, E. Holden Norman, J. Irrgeher, D. Loss Robert, T. Walczyk and T. Prohaska, *Pure and Applied Chemistry*, 2016, **88**, 265-291.

31. W. E. W. NIST Mass Spectrometry Data Center, director, NIST Chemistry WebBook, NIST Standard reference database number 69, Eds. P.J. Linstrom and W.G. Mallard, National Institute of Standards and Technology, Gaithersburg MD, 20899, https://doi.org/10.18434/T4D303, (retrieved November 2, 2020).

32. X. Liu, J. Zhang, A. Vazquez, D. Wang and S. Li, *Physical Chemistry Chemical Physics*, 2018, **20**, 18782-18789.

33. X. Liu, J. Zhang, A. Vazquez, D. Wang and S. Li, *The Journal of Physical Chemistry A*, 2019, **123**, 10520-10528.

34. R. G. Wang, M. A. Dillon and D. Spence, *The Journal of Chemical Physics*, 1984, **80**, 63-69.

35. K. Shao, Y. Tian and J. Zhang, *The Journal of Physical Chemistry A,* 2022, **126**, 1085-1093.

CHAPTER 6 Thermal Decomposition Mechanism of Tetraethylsilane: The Competition between β-Hydride Elimination and Bond Homolysis

6.1 Introduction

Silicon carbide (SiC) thin film, due to its excellent performance in physical, chemical, and electronic properties, has been widely applied in the electronic industry.[1-4] Using organosilanes as a single source precursor for the SiC thin film production in chemical vapor deposition (CVD) has become an improvement initiative.[5-10] Compared to using separate carbon and silicon precursors, using single source organosilanes precursor, as the Si-C bond already exists, could avoid high temperatures which are required for the formation of Si-C bond in gas phase between the carbon and silicon precursors, and therefore, reduce the mismatches between Si and SiC in lattice constants and thermal expansion coefficients.[8, 11] A number of organosilanes have been regarded as good candidates for CVD production of SiC;[12] among them, tetraethylsilane ($SiEt_4$) has been considered as a popular precursor in various investigations of SiC thin film productions using the CVD method.[12-19]

Amjoud et al. studied the metal-organic CVD of tetraethylsilane at 500 – 1000 ^{o}C in a classical horizontal CVD reactor interfaced with a gas-phase chromatograph.[16] It was found that thermal decomposition of tetraethylsilane started at 845 ^{o}C in helium carrier gas and C_2H_4 was a major product in the gas-phase reactions. However, a detailed gas-phase reaction mechanism was not proposed. Pola et al. explored ArF laser photolysis of tetraethylsilane at 193.3 nm for its suitability for use in CVD of Si/C materials and examined the products using FTIR spectroscopy.[20] It was reported that the only initiation pathway in the photolytic decomposition of tetraethylsilane is β-hydride elimination of ethylene (reaction (6.1)), and the produced $HSiEt_3$ would further undergo stepwise ethylene elimination reactions until the formation of SiH_4 (reaction (6.2)). However, it was also noted that the presumed key intermediates H_2SiEt_2, H_3SiEt, and SiH_4 were not detected.

$$SiEt_4 \xrightarrow{hv \text{ at 193 nm}} HSiEt_3 + C_2H_4 \tag{6.1}$$

$$HSiEt_3 \xrightarrow{\text{multistep photolysis at 193 nm}} SiH_4 + 3C_2H_4 \tag{6.2}$$

The β-hydride elimination mechanism was also found in the pyrolysis of ethylsilane (H_3SiEt), a simple homologue of tetraethylsilane ($SiEt_4$). The thermal decomposition mechanism of ethylsilane (H_3SiEt) has been investigated by several researchers.[21-24] Ring et al. and Rickborn et al. studied the thermal decomposition of H_3SiEt using a single-pulse shock tube at temperatures between 1080 K and 1245 K.[21, 22] They proposed that the thermal decomposition of H_3SiEt did not undergo the direct β-hydride elimination of ethylsilane (reaction (6.3)); instead, it was primarily initiated by an H_2 elimination channel (reaction (6.4)). The produced reactive intermediate, HSiEt, further dissociated via a β-hydride elimination channel to SiH_2 and C_2H_4 (reaction (6.5)). Jardine et al. studied the thermal decomposition of ethylsilane in a static cell,[23, 25] and Sela et al. later revisited the thermal decomposition of ethylsilane using a single-pulse shock tube;[24] their results were mostly in agreement with the initiation reaction of H_3SiEt and its subsequent dissociation reactions proposed by Ring et al. and Rickborn et al.[21, 22] The gas-phase pyrolysis study on other ethylsilanes, diethylsilane, triethylsilane, and tetraethylsilane, has been limited. The

β-hydride elimination reaction of the surface SiEt group producing ethylene and SiH on the surface (reaction (6.6)) is a tool to quantitatively explore the adsorption and decomposition of ethylsilanes (H_xSiEt_{4-x}) on the surface.[12, 26-29] Nevertheless, the fundamentals of the β-hydride elimination mechanism of the SiEt group are less studied in the gas phase. Tetraethylsilane would be an ideal candidate to investigate the β-hydride elimination reaction of the SiEt group in the gas phase, as it does not possess an active Si-H bond and the initial reaction mechanism could be less complicated.[12]

$$H_3SiEt \rightarrow SiH_4 + C_2H_4 \qquad (6.3)$$

$$H_3SiEt \rightarrow HSiEt + H_2 \qquad (6.4)$$

$$HSiEt \rightarrow SiH_2 + C_2H_4 \qquad (6.5)$$

$$Si\text{-}C_2H_5(ad) \rightarrow SiH\ (ad) + C_2H_4 \qquad (6.6)$$

To further explore the gas-phase decomposition mechanism of tetraethylsilane and its adequacy for CVD, and to better understand the β-hydride elimination mechanism of the SiEt group in the gas phase, flash pyrolysis of tetraethylsilane ($SiEt_4$) was studied using vacuum ultraviolet photoionization time-of-flight mass spectrometry (VUV-PI-TOF-MS) in this chapter. Density functional theory (DFT) calculations of the energetics of the reactants, transition states, and products were carried out to identify the competing reaction pathways. Furthermore, transition state theory (TST)/variational transition state theory (VTST) calculations were performed, and the rate constants of various unimolecular decomposition pathways were compared to illustrate the competitions between the β-hydride elimination and the bond homolysis reactions.

6.2 Experimental and computational methods

The thermal decomposition study of tetraethylsilane was conducted using a home-made flash pyrolysis vacuum ultraviolet photoionization time-of-flight mass spectrometer (VUV-PI-TOFMS), which has been described previously in this thesis.[30-35] The tetraethylsilane sample was purchased from Sigma Aldrich (99 %). The precursor was introduced in the apparatus by bubbling helium carrier gas through the liquid tetraethylsilane sample; the total backing pressure of the gas mixture was around 950 torr, while the precursor was diluted to ~ 0.5 % in the gas phase.

DFT calculations on the geometries and energetics of the corresponding transition states, intermediates, products, and reactants were performed using the Gaussian 16 package.[36] All geometries including transition states were optimized using the UB3LYP method under 6-31+G(d,p) basis sets. This method was chosen as it has been reported that the B3LYP method provides good results in geometry optimization while maintaining computational efficiency, and the unrestricted method was employed to ensure the consistency between the open-shell and closed-shell calculations.[37, 38] A scaling factor of 0.964 was applied to all the zero-point energies, as recommended by the Computational Chemistry Comparison and Benchmark DataBase (CCCBDB). The single-point energy for each species was calculated at the UM06-2X/6-311++G(3df, 2pd) level of theory.[39] The M06-2X method could produce good thermal chemistry calculation results for main group compounds with a reasonable computational cost.[40] Transition states with only one imaginary frequency were tested using intrinsic reaction coordinate (IRC) calculations at the UB3LYP/6-31+G(d,p) level. The geometries of the species involved could be located in the Supporting Information (SI). All results are presented as relative energies at 0 Kelvin (ΔE_{0K}).

Unimolecular reaction rate constants of the tetraethylsilane ($SiEt_4$) dissociation channels, and the secondary dissociation channels of the triethylsilyl radical ($SiEt_3$) were calculated using TST and VTST. For the unimolecular dissociation reaction with a conventional transition state, the rate constant was calculated using TST with Wigner tunneling correction at various temperatures.[41-44] The frequency analysis of reactants and transition states were evaluated at the UB3LYP/6-31+G(d,p) level of theory with a recommended scaling factor,[45] while the single point energy calculations were carried out at the UM06-2X/6-311++G(3df,2pd) level of theory as described earlier. All rate constant calculations were performed utilizing the KISTHELP package.[43, 46, 47]

6.3 Results and discussions

The mass spectra of the tetraethylsilane pyrolysis at temperatures between 300 K and 1330 K are displayed in Figure 6.1. At 300 K, the signal of m/z = 144 and 145 represented the parent molecule tetraethylsilane ($SiEt_4$). The relative abundance for ^{28}Si, ^{29}Si, and ^{30}Si is 92.2 %, 4.7 %, and 3.1 %, respectively.[48] The relative abundance of ^{12}C and ^{13}C is 98.9 % and 1.01 %. The ratio of peak area of m/z = 145 to m/z = 144 was determined to be 0.19 in Figure 6.1, close to the theoretical value of 0.14. Other peaks at 300 K, such as m/z = 115 and 116 ($SiEt_3$), m/z = 87 ($HSiEt_2$), and m/z = 141 were caused by dissociative photoionization of the parent molecule.

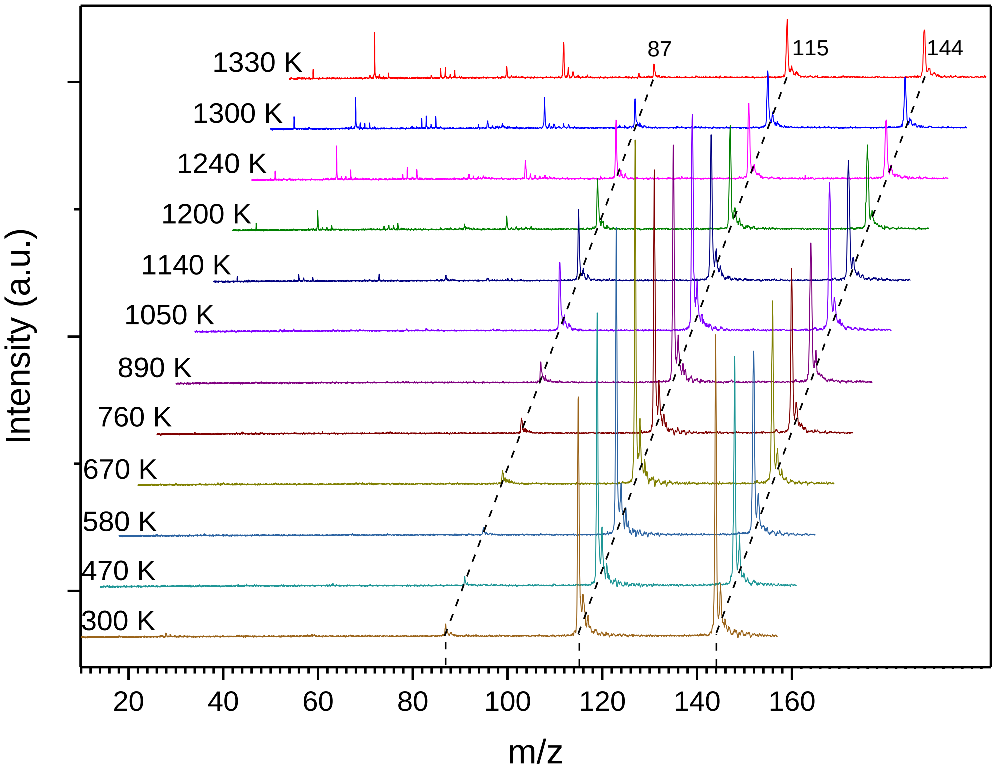

Figure 6.1 Mass spectra of the tetraethylsilane pyrolysis at 300 K to 1330 K. The mass spectra are offset horizontally and vertically for clarity.

(a) The initiation step of the tetraethylsilane pyrolysis

Similar to the thermal decomposition of the related organosilane molecule tetramethylsilane ($SiMe_4$),[33, 49] the Si-C bond fission (reaction (6.7)) was considered the initiation step in the tetraethylsilane pyrolysis. As shown in Figure 6.1 and Figure 6.2, the signal of m/z = 115, which corresponds to $SiEt_3$, was observed at 300 K as a dissociative photoionization peak of the parent molecule. As the temperature increased, its peak intensity increased and then started to decrease above 1050 K. Both dissociative photoionization and thermal decomposition of the parent molecule can contribute to the

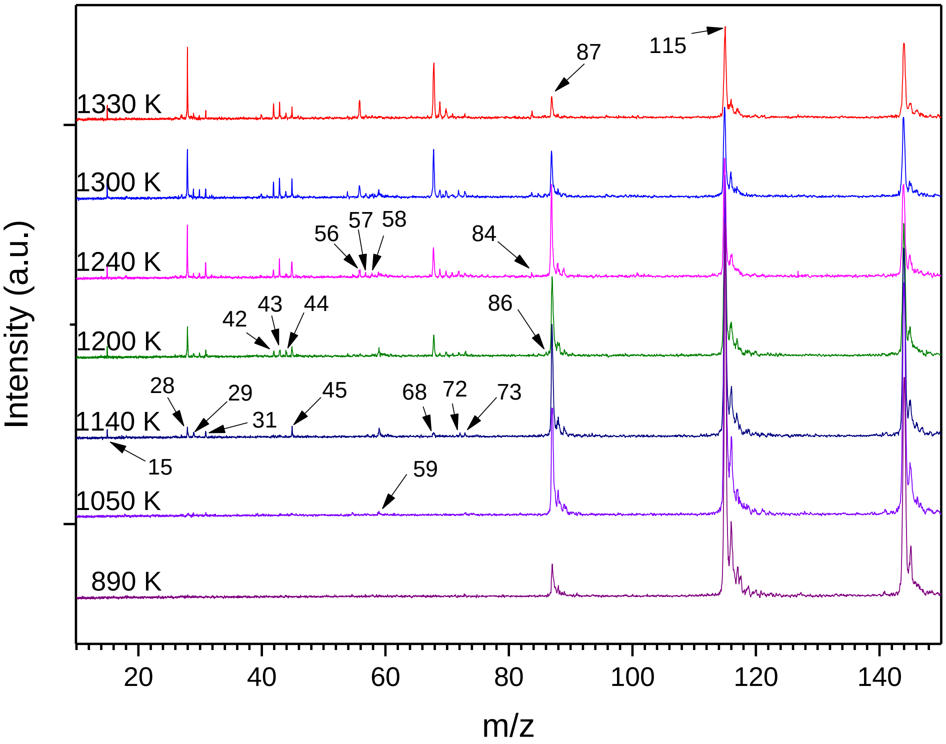

Figure 6.2 Enlarged mass spectra of the tetraethylsilane pyrolysis from 890 K to 1330 K. The mass spectra are offset vertically for clarity.

peak area of the fragment peak. At low temperatures, the fragment peak was only due to the dissociative photoionization; as the temperature increased beyond the decomposition onset temperature, the thermal decomposition started to contribute to the fragment peak. Consequently, as shown by Li et al. and Shao et al,[34, 49] plotting the ratio of the fragment peak area to the parent peak area is a useful method to determine the temperature at which the thermal decomposition reaction starts. However, the peak area ratio of m/z 115 vs. m/z 144 was 0.86 at 300 K, which was large due to the prominent contribution to m/z 115 from dissociative photoionization of the parent molecule and hindered the determination of the additional contribution from thermal decomposition at elevated temperatures.[34] Instead, the peak area ratio of m/z 87 vs. m/z 144 is plotted in Figure 6.3 to determine the onset temperature for reaction (6.7). $SiEt_3$ was the product of the primary reaction (6.7), and, as will be discussed later, it could promptly decompose into $HSiEt_2$ (m/z = 87) and C_2H_4 via a two-step mechanism (reaction (6.8)). The production of $HSiEt_2$ (m/z = 87), as the immediate secondary decomposition product of $SiEt_3$, could suggest the upper limit of the onset temperature of reaction (6.7). According to Figure 6.3, the peak area ratio of m/z 87 vs. m/z 144 increased initially around 890 K and then significantly around 1050 K, and the ratio dropped when it reached its maximum at 1240 K. The co-product of $SiEt_3$ in reaction (6.7), C_2H_5 (m/z = 29), was first detected at 1050 K. Its peak intensity increased with increasing temperature until 1300 K, and then it started to decrease. These could serve as direct evidence that reaction (6.7) was initiated around 1050 K. From the discussions above, it is considered that the onset temperature for the Si-C bond homolysis reaction (reaction (6.7)) was around 1050 K.

$SiEt_4 \rightarrow SiEt_3 + C_2H_5$ (6.7)

$SiEt_3 \rightarrow HSiEt_2C_2H_4 \rightarrow HSiEt_2 + C_2H_4$ (6.8)

The *β*-hydride elimination mechanism of tetraethylsilane (reaction (6.9)) was not experimentally observed in the initiation step. The possible products of reaction (6.9) are triethylsilane ($HSiEt_3$) and ethylene (C_2H_4). In Figure 6.1 and 6.2, the signal of $HSiEt_3$ (m/z = 116) overlapped with one of the isotopic signals of $SiEt_3$. The peak area ratio of m/z 116 vs. m/z 115 is plotted in Figure 6.3 in order to identify the production of $HSiEt_3$. However, the curve remained flat as the temperature increased, reflecting the peak area ratio of the m/z 116 and m/z 115 isotope peaks in $SiEt_3$ and indicating little or no production of $HSiEt_3$

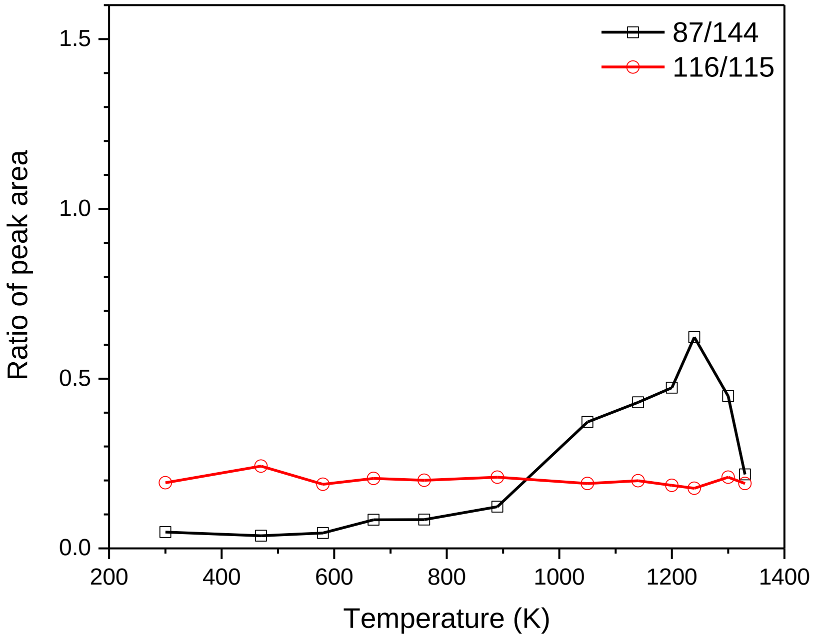

Figure 6.3 The plot of the m/z = 87 peak area over m/z = 144 peak area, and the m/z = 116 peak area over m/z = 115 peak area in the temperature range from 300 K to 1330 K.

from thermal decomposition at all the temperatures. The signal of C_2H_4, the possible co-product of $HSiEt_3$ in reaction (6.9), was first observed at 1140 K as shown in Figure 6.2; however, it could be produced from the fast H-loss reaction of C_2H_5 (produced in reaction (6.7)) or reaction (6.8) instead.[50, 51]

$$SiEt_4 \rightarrow HSiEt_3 + C_2H_4 \qquad (6.9)$$

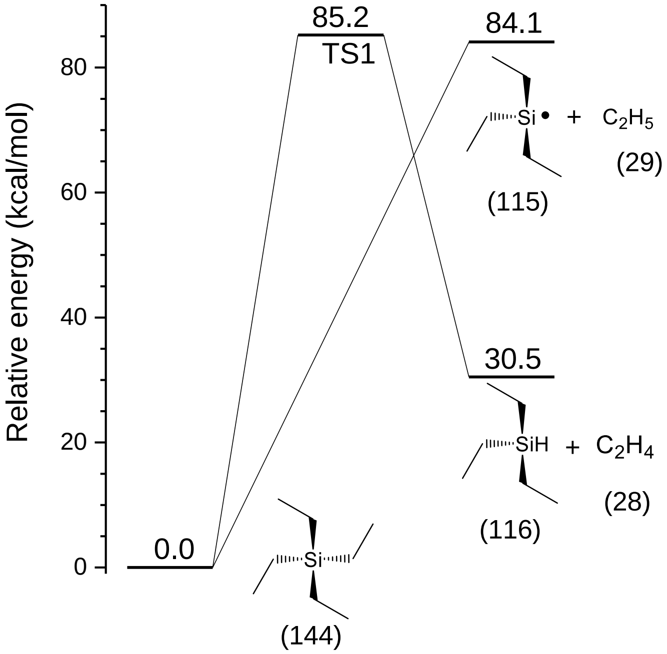

Figure 6.4 Energetics (0 K) of the possible initiation channels for the pyrolysis of tetraethylsilane at the UM06-2X/6-311++G(3df, 2pd)//UB3LYP/6-31+G(d,p) level.

The β-hydride elimination mechanism of tetraethylsilane was also not supported by the theoretical calculations. The quantum chemistry calculations regarding the energetics of the possible initiation channels are displayed in Figure 6.4. The calculated energy threshold for the Si-C bond homolysis reaction (6.7) was 84.1 kcal/mol, while the calculated energy barrier for the β-hydride elimination channel via TS1 was 85.2 kcal/mol. The Si-C bond homolysis reaction is energetically slightly favored than the β-hydride elimination channel, and furthermore it has a loose transition state than the tight transition state of the molecular elimination pathway. Kinetic analysis was performed by the VTST calculation for the bond homolysis channel and the TST calculation for the molecular elimination via TS1. The unimolecular reaction rate constant calculations for the initiation channels are summarized in Figure 6.5. It shows that the rate constant for the Si-C bond fission channel is much larger than that for the β-hydride elimination channel. For example, at the onset temperature of reaction (6.7), 1050 K, the calculated unimolecular rate constant of reaction (6.7) is 0.13 s^{-1}, while that of reaction (6.9) is 9.2×10^{-7} s^{-1}. This rate constant

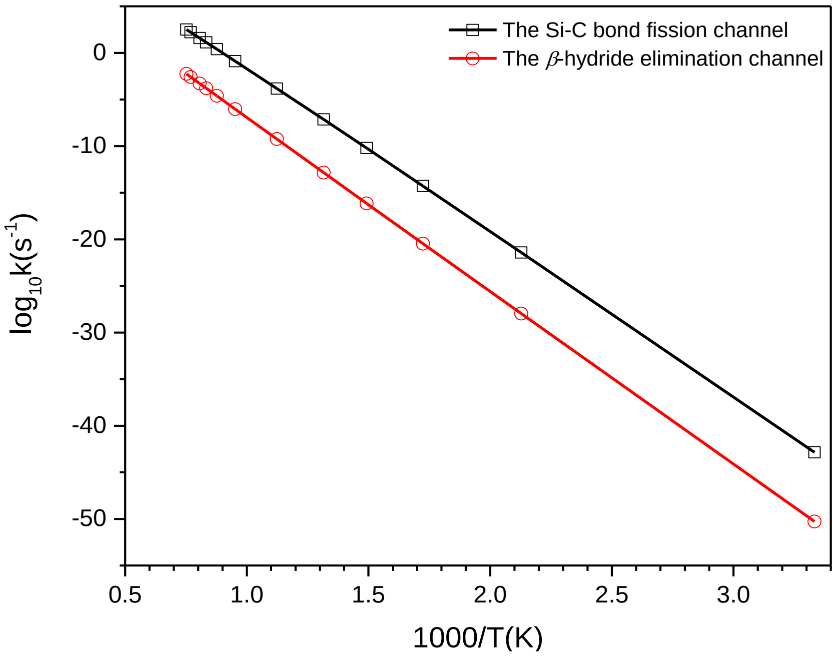

Figure 6.5 Unimolecular rate constant calculations of the initiation reactions with the TST/VTST method. The results are displayed in the form of $\log_{10}k$ vs 1000/T.

comparison demonstrates that the Si-C bond fission reaction is much more competitive than the β-hydride elimination reaction in the initiation step.

(b) Secondary reactions of the triethylsilyl radical

The secondary reaction of the trimethylsilyl radical, which was the predominant product in the initiation step, was mostly advanced by the β-hydride elimination mechanism. As mentioned earlier, the appearance of the m/z = 87 peak ($HSiEt_2$) was used as the evidence to identify the production of the triethylsilyl radical. In Figure 6.1 and 6.2, the signal of the m/z = 87 peak started to increase significantly at around 1050 K. The signal of the counterpart of $HSiEt_2$ in reaction (6.8), C_2H_4 (m/z = 28), was first found at 1140 K, and its intensity kept increasing with the temperature. C_2H_4 (m/z = 28) was not observed simultaneously at 1050 K, possibly because its ionization potential (10.51 eV[52]) is slightly higher than the VUV photon energy (10.49 eV) which made the detection of the C_2H_4 signal difficult.[32] Figure 6.3 also shows the trend of the peak ratio of m/z 87 vs. m/z 144 as a function of temperature, indicating that thermal decomposition contribution to the m/z = 87 peak became significant at around 1050 K. On the other hand, the Si-C bond homolysis of the triethylsilyl radical (reaction (6.10)) was found to be insignificant. As shown in Figure 6.1 and 6.2, the signal of $:SiEt_2$ (m/z = 86) first appeared at 1200 K with a very small intensity, and as the temperature further increased, the m/z =86 signal disappeared. In the mass spectra (Figure 6.1 and 6.2), m/z = 100 and 114 peaks were not observed at all the elevated temperature, indicating the absence of β-sicssion pathways of $SiEt_3$, $Et_2Si{=}CH_2$ (m/z = 100) + CH_3 and $Et_2Si{=}CHCH_3$ (m/z =114) + H. This was consistent with the fact that the formation of the Si=C bond (in both $Et_2Si{=}CH_2$ and

$Et_2Si=CHCH_3$) is energetically less favorable than the formation of the C=C bond (in C_2H_4 in the main pathway, reaction (6.8)).

$$SiEt_3 \rightarrow :SiEt_2 + C_2H_5 \tag{10}$$

To illuminate the β-hydride elimination mechanism of the triethylsilyl radical, and compare the energetics of several competing reaction channels, quantum chemistry calculations regarding dissociations of $SiEt_3$ were carried out, and the results are displayed in Figure 6.6. The theoretical calculations indicated that the β-hydride elimination reaction of $SiEt_3$ proceeds via a two-step pathway. $SiEt_3$ first isomerizes to an intermediate ($HSiEt_2C_2H_4$) via TS2 with an energy barrier of 37.5 kcal/mol. Then it readily decomposes into $HSiEt_2$ and C_2H_4 via TS3, with an energy barrier of 24.9 kcal/mol with respect to $HSiEt_2C_2H_4$ (reaction (6.8)). The overall energy barrier for the β-hydride elimination of $SiEt_3$ is 37.5 kcal/mol. The energy threshold for its competing reaction channel, the Si-C

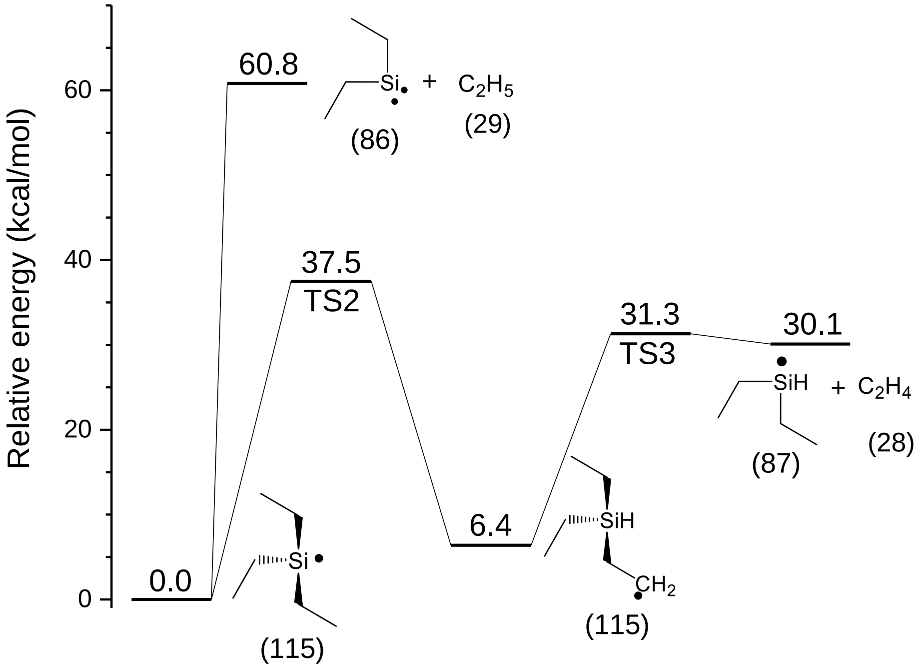

Figure 6.6 Energetics (0 K) of the dissociation channels of $SiEt_3$ at the UM06-2X/6-311++G(3df, 2pd)//UB3LYP/6-31+G(d,p) level.

bond cleavage producing $:SiEt_2$ and C_2H_5, is calculated to be 60.8 kcal/mol. It shows that the *β*-hydride elimination reaction of $SiEt_3$ is energetically favored. The TST and VTST methods were applied to calculate the unimolecular rate constants of these two competing reaction pathways at different temperatures. As shown in Figure 6.7, the unimolecular rate constant for the *β*-hydride elimination channel (energetically favored via a tight TS) is larger than that of the C_2H_5 loss channel (energetically less favored via a loose TS). For example, at 1050 K, the rate constant for the *β*-hydride elimination channel is 1.8×10^5 s^{-1}, more than 1 order of magnitude higher than that of the C_2H_5 loss channel (7.6×10^3 s^{-1}). As the temperature further increased, the difference between the two rate constants became smaller. When the temperature reached 1330 K, the calculated rate constant for the *β*-

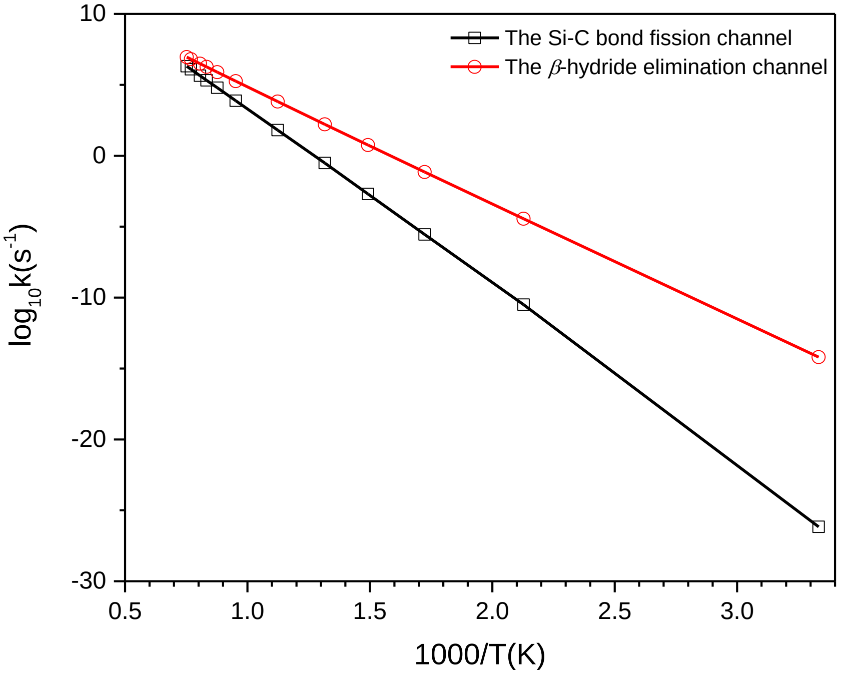

Figure 6.7 Unimolecular rate constant calculations of the triethylsilyl radical ($SiEt_3$) using the TST/VTST method. The results are displayed in the form of $\log_{10}k$ vs 1000/T.

hydride elimination channel of $SiEt_3$ (9.1×10^6 s^{-1}) is larger than that of the C_2H_5 loss channel (2.0×10^6 s^{-1}) by a factor of 4.5. It is then concluded that, around the onset temperature, thermal dissociation of $SiEt_3$ proceeded predominantly via the β-hydride elimination channel, and at higher temperatures, the C_2H_5 loss channel became significant. This could explain the first appearance of the m/z = 86 signal at 1200 K, since its bond homolysis rate constant (2.1×10^5 s^{-1}) is only an order of magnitude smaller than that of the β-hydride elimination channel (1.8×10^6 s^{-1}).

(c) Other important secondary reactions in the tetraethylsilane pyrolysis system.

Evidence for the appearance of other secondary reactions was also identified. As shown in Figure 6.2, the signal of m/z = 59 (H_2SiEt) was first observed at 1050 K, and its intensity started to increase until the temperature reached 1200 K, and then gradually disappeared as the temperature further increased. Based on the earlier discussion, because the production of $HSiEt_2$ (m/z = 87) became significant at 1050 K and the appearance of the m/z = 59 peak was prior to the signals of other fragment peaks, it is postulated that H_2SiEt was produced from secondary dissociation of $HSiEt_2$. Theoretical calculation regarding the energetics of the dissociation channels of $HSiEt_2$ is shown in Figure 6.8. As suggested by the DFT calculations, the dissociation of $HSiEt_2$ leading to the production of

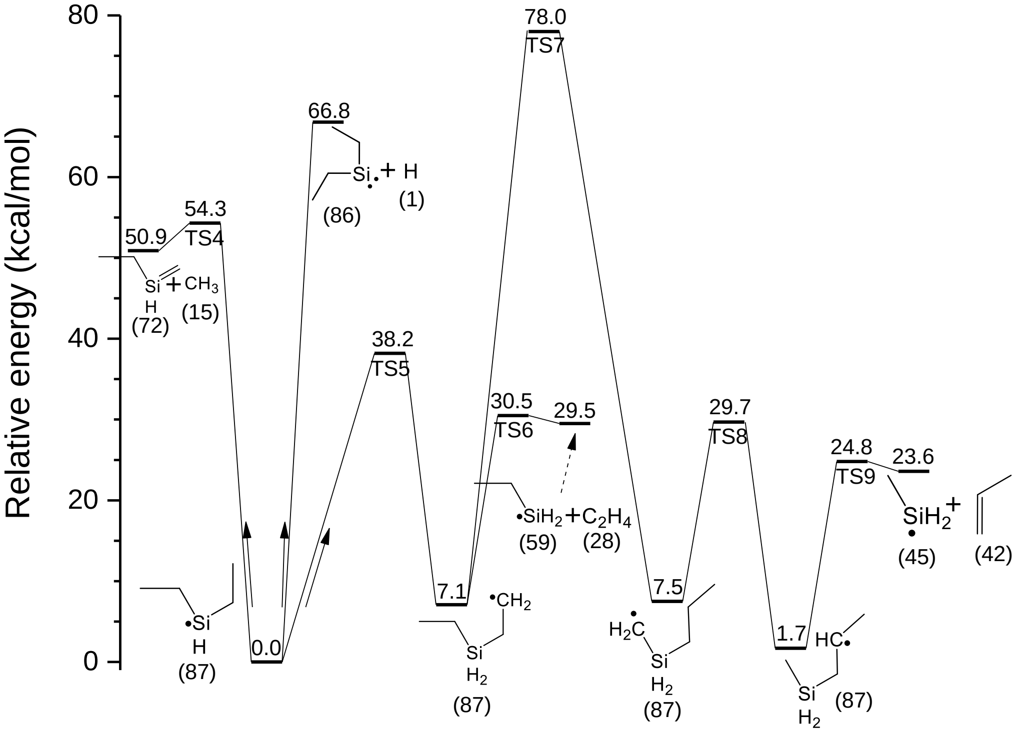

Figure 6.8 Energetics (0 K) of the possible decomposition channel of $HSiEt_2$ at the UM06-2X/6-311++G(3df, 2pd)//UB3LYP/6-31+G(d,p) level.

H_2SiEt (reaction (6.11)) was similar to the production of $HSiEt_2$ from $SiEt_3$ (reaction (6.8)) via the β-hydride elimination mechanism. $HSiEt_2$ first isomerized to $H_2SiEtC_2H_4$ with an energy barrier (TS5) of 38.2 kcal/mol, followed by further decomposition to H_2SiEt and C_2H_4 via TS6 with an energy barrier of 23.4 kcal/mol (with respect to $H_2SiEtC_2H_4$).

$$HSiEt_2 \rightarrow H_2SiEtC_2H_4 \rightarrow H_2SiEt + C_2H_4 \qquad (6.11)$$

Figure 6.8 also indicated a direct decomposition pathway of $HSiEt_2$ that produces $EtHSi{=}CH_2$ and CH_3 (reaction (6.12)) via TS4, with an energy barrier of 54.3 kcal/mol. This possible reaction pathway was supported by the experimental observations. At 1140 K, the signal of m/z = 72, and m/z = 68 (SiC_3H_4) was first observed. When the temperature further increased, the signal of the m/z = 72 peak remained nearly constant, while the signal intensity of the m/z = 68 peak kept increasing. Earlier studies have established that the detection of the m/z = 68 signals signifies the formation of dimethylsilene ($Me_2Si{=}CH_2$) (m/z = 72) and its isomers such as $EtHSi{=}CH_2$, as dimethylsilene ($Me_2Si{=}CH_2$) can readily undergo thermal decomposition to the neutral m/z = 68 species under the comparable reaction conditions.[33, 34, 53, 54] It is noted that the dimerization of $Me_2Si{=}CH_2$, which could lead to the production of 1,1,3,3-tetramethyl-1,3-disilacyclobutane (m/z = 144) as reported by Tong et al.,[55] could not be confirmed in this study due to the overlap of the resulting signal with that of the parent molecule $SiEt_4$; this dimerization process was unlikely under the current experimental conditions (very short residence time and low concentrations). Furthermore, as the co-product of $EtHSi{=}CH_2$, the signal of the methyl radical (m/z = 15) was also first observed at 1140 K. Therefore, it is argued that the secondary reaction of

$HSiEt_2$ led to the production of $EtHSi=CH_2$ and CH_3 from around 1140 K and on. The signal of m/z = 73 (SiC_3H_9) also first appeared at 1140 K, and the origin of this peak was unclear. As previous studies inferred that the ionization cross section of the m/z = 73 species is large,[34, 54, 56] its barely detectable peak intensity suggested that the m/z = 73 species was negligible in the system. Also, quantum chemistry calculation did not demonstrate any possible unimolecular dissociation channel that could explain the appearance of the m/z = 73 signal.

$$HSiEt_2 \rightarrow EtHSi{=}CH_2 + CH_3 \qquad (6.12)$$

Theoretical calculations may provide a plausible explanation for the H_2SiCH_3 (m/z = 45) production in the secondary reactions of $HSiEt_2$. According to Figure 6.2, the m/z = 45 signal was first detected at 1140 K, and as the temperature further increased, its peak intensity kept increasing until 1300 K, and then started to decrease. The DFT calculations indicated that the formation of the m/z = 45 species involved a series of isomerization of $HSiEt_2$, followed by a Si-C homolysis. As shown in Figure 6.8, $HSiEt_2$ first isomerizes to $H_2Si(C_3H_6)CH_3$ via two transition states, TS7 and TS8, and their energy barriers were determined to be 70.9 kcal/mol and 22.2 kcal/mol. Finally, $H_2Si(C_3H_6)CH_3$ overcomes an energy barrier of 23.1 kcal/mol via TS9, leading to the formation of H_2SiCH_3 (m/z = 45) and C_3H_6 (m/z = 42). The signal for the counterpart of H_2SiCH_3 in this reaction (C_3H_6 m/z = 42), however, was not observed simultaneously at 1140 K. The ionization potential of C_3H_6 is 9.73 eV,[57] which is lower than the VUV photon energy used in this work. Therefore, the missing of the m/z = 42 signal indicated the absence of the C_3H_6 species at

1140 K, and thus, it could not support the proposed mechanism. The relatively high energy barrier for TS7 (78.0 kcal/mol relative to $HSiEt_2$) also suggests that there might be an alternative route for the formation of the m/z = 45 signal, which has not been identified yet.

Besides, as shown in Figure 6.8, the H-loss of $HSiEt_2$ may contribute to the formation of the m/z = 86 ($:SiEt_2$) signal, with an energy threshold of 66.8 kcal/mol. As discussed above, $:SiEt_2$ could be produced from reaction (6.10) directly at around 1200 K. Alternatively the H-loss channel of $HSiEt_2$ may offer another possible reaction route for the formation of the m/z = 86 species.

The possible secondary reactions of $:SiEt_2$ (m/z = 86) were also discovered in this work. $:SiEt_2$ may undergo a series of isomerization reactions and lead to the production of the m/z = 84 species. As discussed earlier, $:SiEt_2$ could be one of the products of the secondary reactions of $SiEt_3$, and the reaction rate constant calculations suggests that this reaction pathway became significant at high temperatures. After the first appearance of the m/z = 86 peak at 1200 K, the signal of the m/z = 84 peak was first observed at 1240 K. As the temperature further increased, the signal of the m/z = 84 peak remained nearly unchanged until 1330 K. Theoretical calculations regarding a possible two-step mechanism

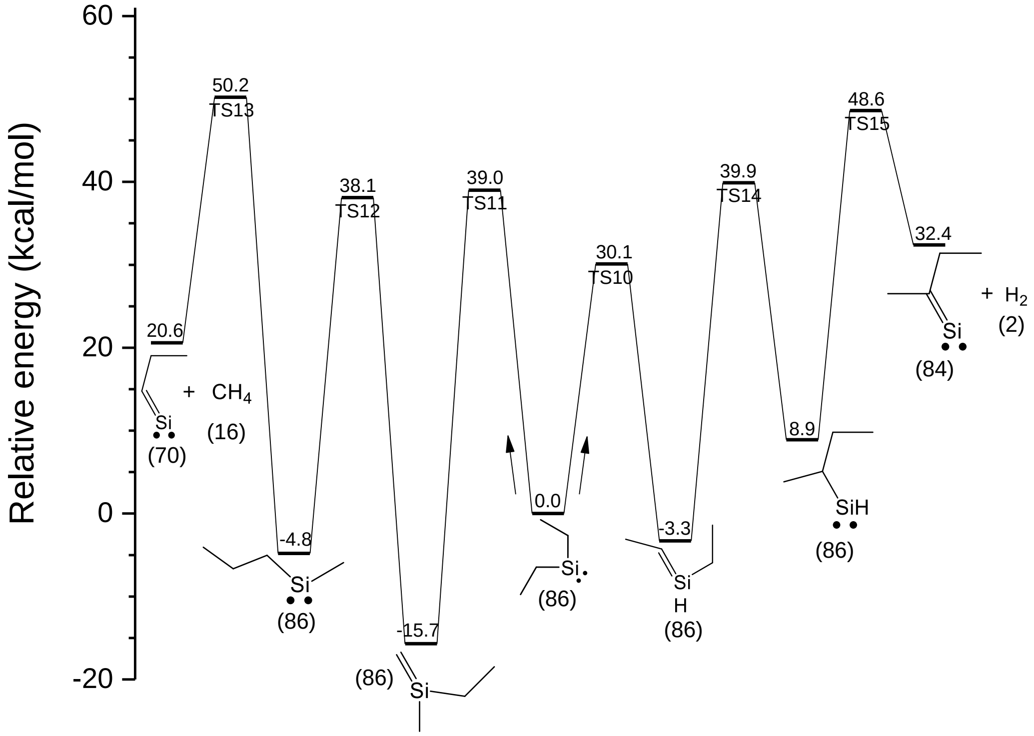

Figure 6.9 Energetics (0 K) of the possible decomposition channel of :SiEt$_2$ at the UM06-2X/6-311++G(3df, 2pd)//UB3LYP/6-31+G(d,p) level.

of its formation were carried out, and the energy diagram is shown in Figure 6.9. According to Figure 6.9, it was suggested that :SiEt$_2$ first went through an isomerization pathway (TS10) leading to the production of EtHSi=CHCH$_3$ with an energy barrier of 30.1 kcal/mol, followed by another isomerization reaction via TS14 forming :Si(H)CH(Et)CH$_3$ with a threshold energy of 43.2 kcal/mol. Finally, :Si(H)CH(Et)CH$_3$ went through a H$_2$ elimination mechanism (TS15) to produce :Si=C(Et)CH$_3$ (m/z = 84), with a calculated energy barrier of 39.7 kcal/mol with respect to :Si(H)CH(Et)CH$_3$ (reaction (6.13)).

Theoretical calculations also revealed other possible dissociation channels of :SiEt$_2$. As shown in Figure 6.9, :SiEt$_2$ could undergo a two-step isomerization reaction through an intermediate CH_2=Si(Et)CH_3 to :Si(CH_3)C_3H_7 via TS11 and TS12, and the overall energy barrier was determined to be 39.0 kcal/mol. Then it could further lose one CH_4 to form :Si=CHC_2H_5 (m/z = 70) over an energy barrier of 55.0 kcal/mol (reaction (6.14)). This mechanism is consistent with the experimental observations, since at 1240 K the signal of m/z = 70 was found, although, as discussed earlier, the appearance of the m/z = 70 peak could be evolved from the secondary reactions of the m/z = 72 species. As the overall energy barrier of reaction (6.14) with respect to :SiEt$_2$ (50.2 kcal/mol) is close to that for reaction (6.13) (48.6 kcal/mol), the contribution for m/z = 70 signal from the secondary reactions of :SiEt$_2$ may not be neglected.

$$:\mathrm{SiEt_2} \rightleftharpoons \mathrm{EtHSi{=}CHCH_3} \rightleftharpoons \mathrm{Si(H)CH(Et)CH_3} \rightarrow \mathrm{Si{=}C(Et)CH_3} + \mathrm{H_2} \tag{6.13}$$

$$:\mathrm{SiEt_2} \rightleftharpoons \mathrm{CH_2{=}Si(Et)CH_3} \rightleftharpoons \mathrm{Si(CH_3)C_3H_7} \rightarrow \mathrm{Si{=}CHC_2H_5} + \mathrm{CH_4} \tag{6.14}$$

Several possible dissociation channels for H_2SiEt were found in this chapter. The signal of SiH_3 (m/z = 31) was first found at 1140 K, and its peak intensity remained nearly constant until the temperature reached 1330 K. This was believed to be a secondary reaction product of H_2SiEt. The DFT calculations for the possible dissociation channels are summarized in Figure 6.10. The reaction pathway that leads to the production of the m/z = 31 peak was the most energetically favored. In this pathway, H_2SiEt first isomerizes to

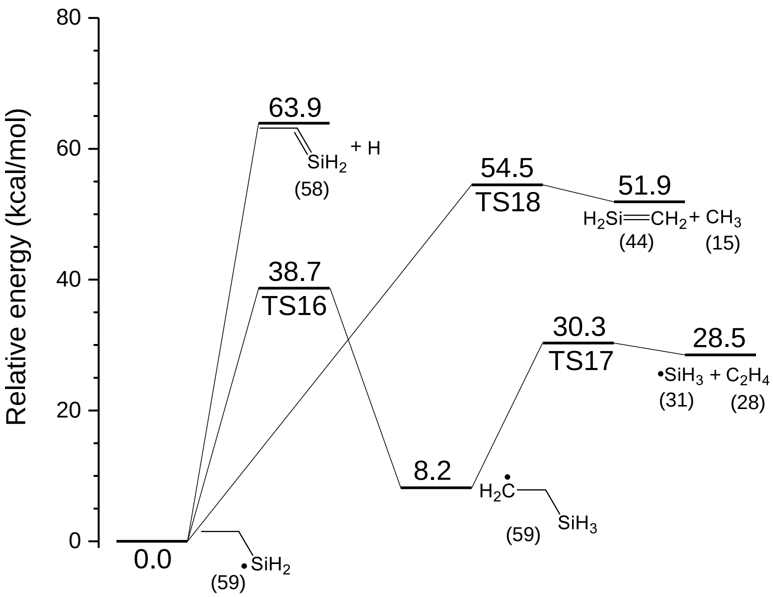

Figure 6.10 Energetics (0 K) of the possible decomposition channel of H_2SiEt at the UM06-2X/6-311++G(3df, 2pd)//UB3LYP/6-31+G(d,p) level.

$H_3SiC_2H_4$ via TS16 with an energy barrier of 38.7 kcal/mol. Then $H_3SiC_2H_4$ decomposes to SiH_3 and C_2H_4 via TS17 with an energy barrier of 22.1 kcal/mol (relative to $H_3SiC_2H_4$).

Theoretical calculations also indicates that H_2SiEt could further decompose into $H_2Si=CH_2$ and CH_3 via TS18, with an energy barrier of 54.5 kcal/mol. The experimental observations are consistent with this proposed mechanism as the signal of the m/z = 44 species was first detected at 1200 K. Its later appearance than the m/z = 31 is also consistent with the theoretical calculations that the energy barrier for TS18 is higher than that for TS16.

H_2SiEt could further lose a hydrogen atom forming $H_2Si=CHCH_3$ (m/z = 58). As shown in Figure 6.2, the m/z = 58 signal first showed up at 1240 K and remained nearly constant when the temperature further increased. One explanation for this peak is the H-loss reaction of H_2SiEt. Figure 6.10 displays that the energy threshold for this reaction is 63.9 kcal/mol, which is higher than the other two reaction pathways of H_2SiEt. Experimental observations agreed with these calculation results, since the temperature for the first appearance of m/z = 58 is higher than those of the other two reaction pathways.

When the pyrolysis temperature further increased, more fragment signals appeared, and the fragment signal from m/z = 54 – 57 were possibly yielded from the secondary reactions of the m/z = 58 species ($H_2Si{=}CHCH_3$). For example, as shown in Figure 6.2, the signal of the m/z = 57 and 56 species first showed up at 1240 K, and these two peaks were possibly the dissociation reaction products of the m/z = 58 species discussed earlier. Their

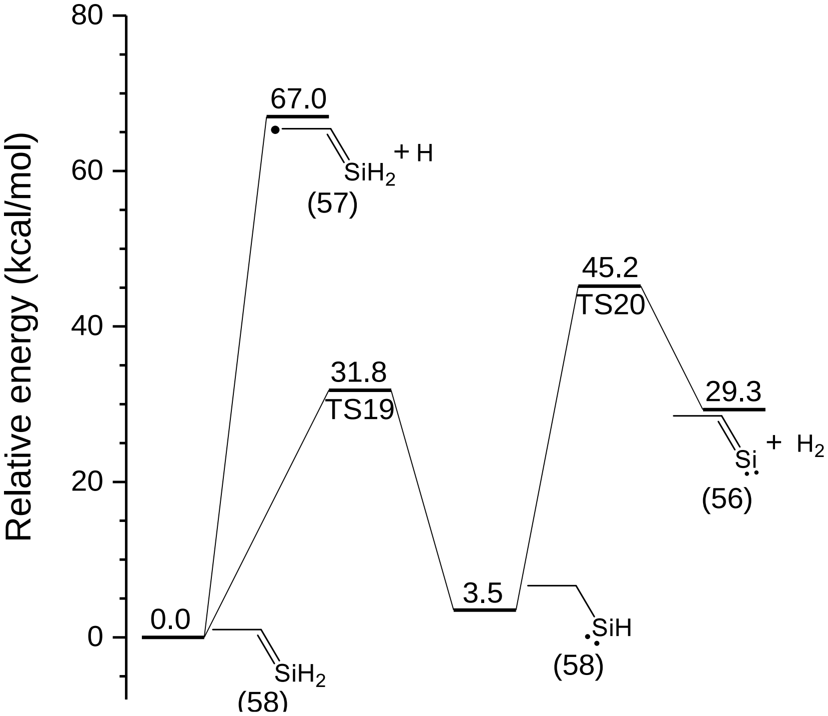

Figure 6.11 Energetics (0 K) of the possible decomposition channel of the m/z = 58 species at the UM06-2X/6-311++G(3df, 2pd)//UB3LYP/6-31+G(d,p) level.

possible dissociation reaction energetics were calculated theoretically and are displayed in Figure 6.11. Figure 6.11 suggests that there may be an isomerization reaction channel between $H_2Si=CHCH_3$ and :SiHEt via TS19 with an energy barrier of 31.8 kcal/mol. The m/z = 56 species (:$Si=CHCH_3$) was possibly caused by H_2 elimination reaction of :SiHEt, via TS20 with an energy barrier of 41.7 kcal/mol. As the temperature increased to 1300 K, the m/z = 54 signal first appeared; it might correspond to :$Si=C=CH_2$, possibly produced from further H_2 elimination reactions of :$Si=CHCH_3$. The m/z = 57 species were probably produced from the H-loss reaction of $H_2Si=CHCH_3$, with an energy threshold of 67.0 kcal/mol.

The m/z = 43 and 42 signal were also captured in this chapter. When the temperature reached 1200 K, the m/z = 43 and 42 signal first appeared. Unlike the m/z = 44 signal, the intensity for the m/z = 43 and 42 signal kept increasing when the temperature further increased. It was possibly caused by further dissociations of the m/z = 44 species. Previous studies have discussed the secondary reactions of the m/z = 44 species in detail; the m/z = 44 species could lose H or H_2, and lead to the production of the $SiCH_3$ (m/z = 43) or $SiCH_2$ (m/z = 42) species.[54] Also, the m/z = 44 – 42 signals could correspond to signals of hydrocarbons (C_3H_8 – C_3H_6) from multiple secondary reactions, and it could be further identified by structural studies in the future.

6.4 Conclusion

The thermal decomposition of tetraethylsilane was investigated experimentally by using flash pyrolysis vacuum ultraviolet mass spectrometry. DFT calculations regarding the energetics of the initiation reactions and important secondary reactions were performed. In the initiation step of the tetraethylsilane pyrolysis, the Si-C bond homolysis was found to be the predominant reaction pathway, with $SiEt_3$ as the primary dissociation product, instead of the direct β-hydride elimination pathway. The unimolecular rate constant calculations with the TST and VTST methods revealed that the rate constant of the Si-C bond fission channel was 5 orders of magnitude higher than the β-hydride elimination pathway. In the secondary dissociation pathways of $SiEt_3$, however, the β-hydride elimination pathway producing $HSiEt_2$ was predominant at lower temperatures than the Si-C bond fission (producing $:SiEt_2$); while at higher temperatures, the Si-C bond homolysis became more significant.

Several secondary reactions were identified in the tetraethylsilane pyrolysis. The further dissociation reaction of $HSiEt_2$ was believed to be associated with the appearance of the m/z = 59 species (H_2SiEt); also, possible dissociation channels of $HSiEt_2$ leading to the productions of the m/z = 72 species and the m/z = 45 species were proposed. The secondary reactions of $:SiEt_2$ that led to the formation of the m/z = 84 species and m/z = 70 species were described. Other possible secondary reaction channels that were involved in this chapter, such as the production of the m/z = 54 – 57 species and m/z = 44 – 42 species, were also discussed. The main thermal decomposition mechanism of tetraethylsilane, including the initiation reaction channels and several important secondary reaction pathways, is summarized in Scheme 6.1.

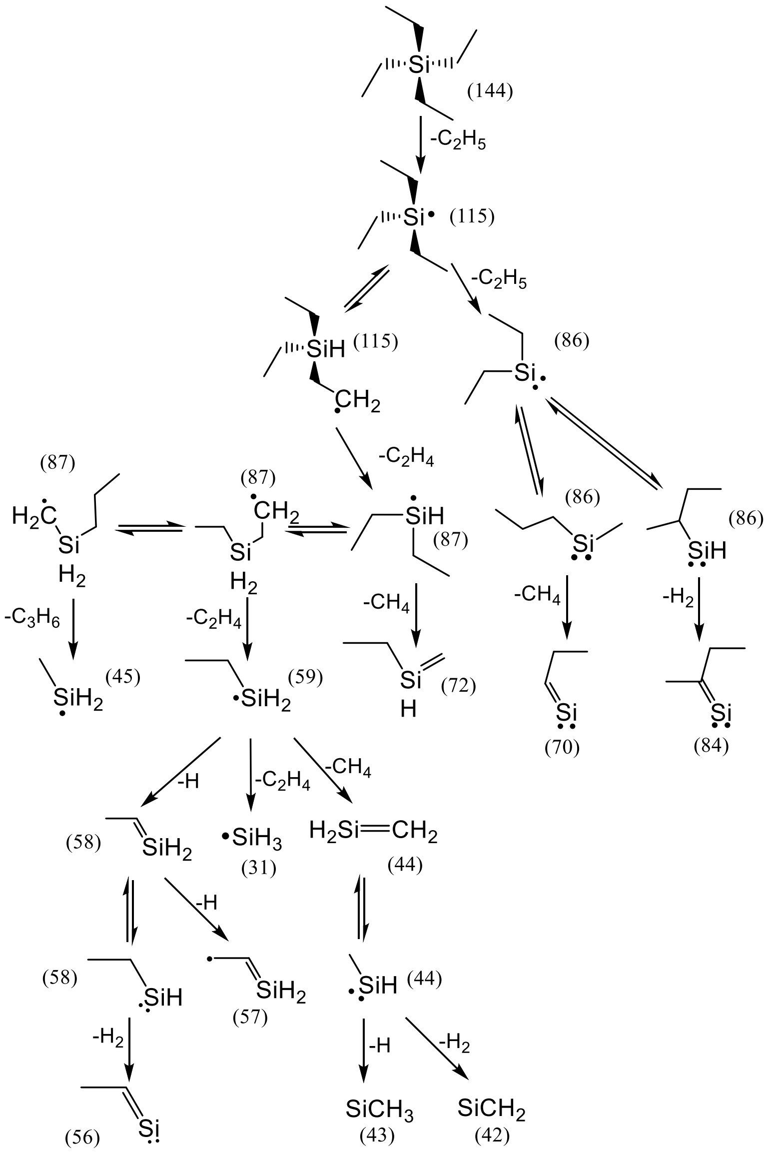

Scheme 6.1 Main thermal decomposition mechanism of the pyrolysis of tetraethylsilane.

REFERENCE

1. L. Sun, G. Yuan, L. Gao, J. Yang, M. Chhowalla, M. H. Gharahcheshmeh, K. K. Gleason, Y. S. Choi, B. H. Hong and Z. Liu, *Nature Reviews Methods Primers*, 2021, **1**, 5.

2. M. A. H. Mohd Sohor, M. Mustapha and J. Chandra Kurnia, *MATEC Web Conf.*, 2017, **131**, 04003.

3. D. Hotza, M. Di Luccio, M. Wilhelm, Y. Iwamoto, S. Bernard and J. C. Diniz da Costa, *Journal of Membrane Science*, 2020, **610**, 118193.

4. R. F. Davis, G. Kelner, M. Shur, J. W. Palmour and J. A. Edmond, *Proceedings of the IEEE*, 1991, **79**, 677-701.

5. J. Selvakumar and D. Sathiyamoorthy, *Journal of Materials Research*, 2012, **28**, 136-149.

6. J. M. Lemieux and J. Zhang, *International Journal of Mass Spectrometry*, 2014, **373**, 50-55.

7. K. C. Kim, K. S. Nahm, Y. B. Hahn, Y. S. Lee and H.-S. Byun, *Journal of Vacuum Science & Technology A*, 2000, **18**, 891-899.

8. I. Golecki, F. Reidinger and J. Marti, *Applied Physics Letters*, 1992, **60**, 1703-1705.

9. A. Veneroni, F. Omarini and M. Masi, *Crystal Research and Technology*, 2005, **40**, 967-971.

10. I. Badran and Y. Shi, *Physical Chemistry Chemical Physics*, 2018, **20**, 75-85.

11. J. M. Lemieux and J. Zhang, *European Journal of Mass Spectrometry*, 2014, **20**, 409-417.

12. A. M. Wrobel, A. Walkiewicz-Pietrzykowska, M. Ahola, I. J. Vayrynen, F. J. Ferrer-Fernandez and A. R. Gonzalez-Elipe, *Chemical Vapor Deposition*, 2009, **15**, 39-46.

13. J. W. Keister, P. Tomperi and T. Baer, *Journal of the American Society for Mass Spectrometry*, 1998, **9**, 597-605.

14. L. Maya, *MRS Online Proceedings Library*, 1993, **327**, 215-220.

15. N. Zaitseva, S. Hamel, Z. R. Dai, C. Saw, A. Williamson and G. Galli, *The Journal of Physical Chemistry C*, 2008, **112**, 3585-3590.

16. M. b. Amjoud, A. Reynes, R. Morancho and R. Carles, *Journal of Materials Chemistry*, 1992, **2**, 1205-1208.

17. L. Vandenbulke and M. Leparoux, *J. Phys. IV France*, 1995, **05**, C5-735-C735-751.

18. D. C. Lee, T. Hanrath and B. A. Korgel, *Angewandte Chemie International Edition*, 2005, **44**, 3573-3577.

19. S. Asahina, N. Kubo, H. Tsuda, N. Kanayama, A. Moritani and K. Kitahara, *Journal of The Surface Finishing Society of Japan*, 2003, **54**, 372-373.

20. J. Pola, J. P. Parsons and R. Taylor, *Journal of Organometallic Chemistry*, 1995, **489**, C9-C11.

21. M. A. Ring, H. E. O'Neal, S. F. Rickborn and B. A. Sawrey, *Organometallics*, 1983, **2**, 1891-1894.

22. S. F. Rickborn, M. A. Ring and H. E. O'Neal, *International Journal of Chemical Kinetics*, 1984, **16**, 1371-1383.

23. R. E. Jardine, H. E. O'Neal, M. A. Ring and M. E. Beatie, *The Journal of Physical Chemistry*, 1995, **99**, 12507-12511.

24. P. Sela, S. Peukert, H. Somnitz, H. Janbazi, I. Wlokas, J. Herzler, M. Fikri and C. Schulz, *Energy & Fuels*, 2021, **35**, 3266-3282.

25. J. G. Martin, M. A. Ring and H. E. O'Neal, *International Journal of Chemical Kinetics*, 1987, **19**, 715-724.

26. P. A. Coon, M. L. Wise and S. M. George, *The Journal of Chemical Physics*, 1993, **98**, 7485-7495.

27. L. A. Keeling, L. Chen, C. Michael Greenlief, A. Mahajan and D. Bonser, *Chemical Physics Letters*, 1994, **217**, 136-141.

28. A. C. Dillon, M. B. Robinson, M. Y. Han and S. M. George, *Journal of The Electrochemical Society*, 1992, **139**, 537-543.

29. M. Foster, B. Darlington, J. Scharff and A. Campion, *Surface Science*, 1997, **375**, 35-44.

30. S. D. Chambreau, J. Zhang, J. C. Traeger and T. H. Morton, *International Journal of Mass Spectrometry*, 2000, **199**, 17-27.

31. S. D. Chambreau and J. Zhang, *Chemical Physics Letters*, 2001, **343**, 482-488.

32. K. Shao, X. Liu, P. J. Jones, G. Sun, M. Gomez, B. P. Riser and J. Zhang, *Physical Chemistry Chemical Physics*, 2021, **23**, 9804-9813.

33. X. Liu, J. Zhang, A. Vazquez, D. Wang and S. Li, *Physical Chemistry Chemical Physics*, 2018, **20**, 18782-18789.

34. K. Shao, Y. Tian and J. Zhang, *International Journal of Mass Spectrometry*, 2021, **460**, 116476.

35. P. J. Jones, B. Riser and J. Zhang, *The Journal of Physical Chemistry A*, 2017, **121**, 7846-7853.

36. M. J. Frisch, G. W. Trucks, H. B. Schlegel, G. E. Scuseria, M. A. Robb, J. R. Cheeseman, G. Scalmani, V. Barone, G. A. Petersson, H. Nakatsuji, X. Li, M. Caricato, A. V. Marenich, J. Bloino, B. G. Janesko, R. Gomperts, B. Mennucci, H. P. Hratchian, J. V. Ortiz, A. F. Izmaylov, J. L. Sonnenberg, Williams, F. Ding, F. Lipparini, F. Egidi, J. Goings, B. Peng, A. Petrone, T. Henderson, D. Ranasinghe, V. G. Zakrzewski, J. Gao, N. Rega, G. Zheng, W. Liang, M. Hada, M. Ehara, K. Toyota, R. Fukuda, J. Hasegawa, M. Ishida, T. Nakajima, Y. Honda, O. Kitao, H. Nakai, T. Vreven, K. Throssell, J. A. Montgomery Jr., J. E. Peralta, F. Ogliaro, M. J. Bearpark, J. J. Heyd, E. N. Brothers, K. N. Kudin, V. N. Staroverov, T. A. Keith, R. Kobayashi, J. Normand, K. Raghavachari, A. P. Rendell, J. C. Burant, S. S. Iyengar, J. Tomasi, M. Cossi, J. M. Millam, M. Klene, C. Adamo, R. Cammi, J. W. Ochterski, R. L. Martin, K. Morokuma, O. Farkas, J. B. Foresman and D. J. Fox, *Gaussian 16 Rev. C.01,* (2016), Wallingford, CT.

37. P. R. Tentscher and J. S. Arey, *Journal of Chemical Theory and Computation*, 2012, **8**, 2165-2179.

38. É. Brémond, M. Savarese, N. Q. Su, Á. J. Pérez-Jiménez, X. Xu, J. C. Sancho-García and C. Adamo, *Journal of Chemical Theory and Computation*, 2016, **12**, 459-465.

39. G. P. Khanal, R. Parajuli, E. Arunan, S. Yamabe, K. Hiraoka and E. Torikai, *Computational and Theoretical Chemistry*, 2015, **1056**, 24-36.

40. Y. Zhao and D. G. Truhlar, *Theoretical Chemistry Accounts*, 2008, **120**, 215-241.

41. D. G. Truhlar, B. C. Garrett and S. J. Klippenstein, *The Journal of Physical Chemistry*, 1996, **100**, 12771-12800.

42. E. Wigner, *Transactions of the Faraday Society*, 1938, **34**, 29-41.

43. S. Canneaux, F. Bohr and E. Henon, *Journal of computational chemistry*, 2014, **35**, 82-93.

44. A. W. Jasper, J. A. Miller and S. J. Klippenstein, *The Journal of Physical Chemistry A*, 2013, **117**, 12243-12255.

45. , NIST Standard Reference Database Number 101, Release 22, May 2022, Editor: Russell D. Johnson III http://cccbdb.nist.gov/.

46. S. Mohandas, R. O. Ramabhadran and S. S. Kumar, *The Journal of Physical Chemistry A*, 2020, **124**, 8373-8382.

47. S. Begum and R. Subramanian, *RSC Advances*, 2015, **5**, 39110-39121.

48. J. Meija, B. Coplen Tyler, M. Berglund, A. Brand Willi, P. De Bièvre, M. Gröning, E. Holden Norman, J. Irrgeher, D. Loss Robert, T. Walczyk and T. Prohaska, *pac*, 2016, **88**, 265-291.

49. X. M. Li, B. D. Eustergerling and Y. J. Shi, *International Journal of Mass Spectrometry*, 2007, **263**, 233-242.

50. G. Amaral, K. Xu and J. Zhang, *The Journal of Chemical Physics*, 2001, **114**, 5164-5169.

51. K. H. Weber, J. M. Lemieux and J. Zhang, *The Journal of Physical Chemistry A*, 2009, **113**, 583-591.

52. K. Ohno, K. Okamura, H. Yamakado, S. Hoshino, T. Takami and M. Yamauchi, *The Journal of Physical Chemistry*, 1995, **99**, 14247-14253.

53. X. Liu, J. Zhang, A. Vazquez, D. Wang and S. Li, *The Journal of Physical Chemistry A*, 2019, **123**, 10520-10528.

54. K. Shao, Y. Tian and J. Zhang, *The Journal of Physical Chemistry A*, 2022, **126**, 1085-1093.

55. L. Tong and Y. J. Shi, *Thin Solid Films*, 2009, **517**, 3461-3465.

56. S. Kawaguchi, K. Takahashi, K. Satoh and H. Itoh, *Plasma Sources Science and Technology*, 2017, **26**, 054001.

57. J. C. Traeger, *International Journal of Mass Spectrometry and Ion Processes*, 1984, **58**, 259-271.

CHAPTER 7 Thermal decomposition of cyclohexane by flash pyrolysis: A study on the initial unimolecular decomposition mechanism

7.1 Introduction

Cycloalkanes and their thermal decompositions are ubiquitous in hydrocarbon fuel usage and biomass conversion.[1-5] Cyclohexane, for its relatively simple structure, has been considered as a prototypical cycloalkane system. The pyrolysis of cyclohexane has been extensively studied experimentally and theoretically. In a single-pulse shock-tube study, Tsang stated that the main initial steps involve isomerization of cyclohexane (c-C_6H_{12}) to 1-hexene (1-C_6H_{12}) through a diradical intermediate ($\bullet CH_2(CH_2)_4H_2C\bullet$), followed by decomposition of 1-hexene to $\bullet C_3H_7$ and $\bullet C_3H_5$ (reaction (7.1)-(7.2)). They argued that C_3H_6 could also be produced from retro-ene dissociation of 1-hexene (reaction (7.3)).[6] Brown et al. reported similar results by applying the very low-pressure pyrolysis (VLPP) technique.[7]

$$\text{c-}C_6H_{12} \rightarrow \bullet CH_2(CH_2)_4H_2C\bullet \rightarrow \text{1-}C_6H_{12} \quad (7.1)$$

$$\text{1-}C_6H_{12} \rightarrow \bullet C_3H_7 + \bullet C_3H_5 \quad (7.2)$$

$$\text{1-}C_6H_{12} \rightarrow 2\ C_3H_6 \quad (7.3)$$

Arikibe et al. developed a numerical kinetic simulation and proposed a detailed mechanism of cyclohexane pyrolysis as shown in Scheme 7.1.[8, 9] In this model, the reaction is initiated by the fission of C-C single bond forming a diradical intermediate, and then it dissociates to different products, such as C_4H_8 + C_2H_4, C_3H_6 + C_3H_6 (reaction (7.4) - (7.5))

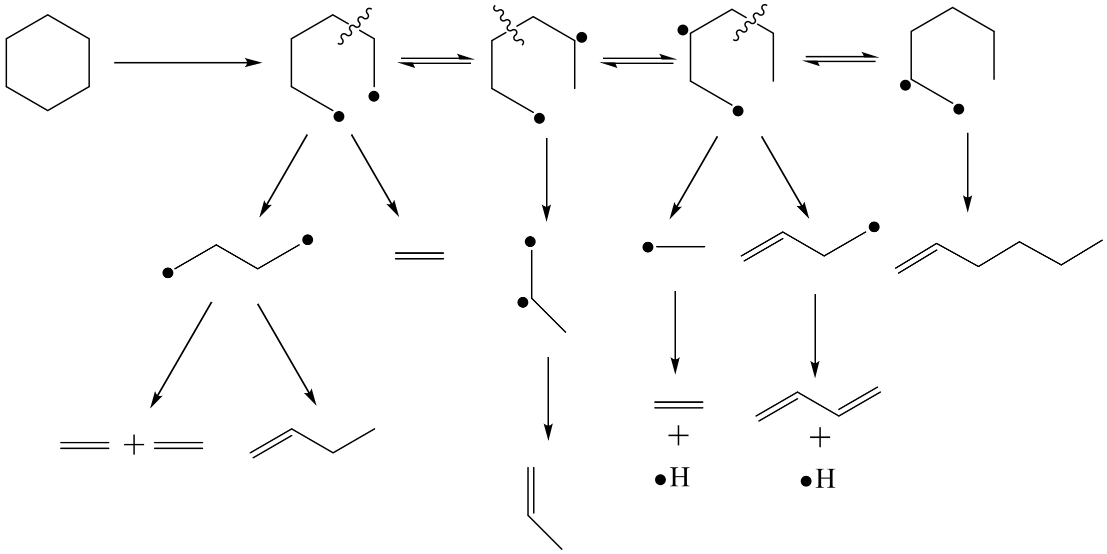

Scheme 7.1 The reaction mechanism for cyclohexane pyrolysis proposed by Aribike et al.[8,9]

and isomerizes to 1-C_6H_{12} (reaction (7.1)). Bakali et al. examined the oxidation of cyclohexane in a jet-stirred reactor (JSR) at various temperatures and pressures.[10] They added that decomposition of cyclohexane to cyclobutane is an important initiation pathway (reaction (7.6)). However, the signal of cyclobutane was not detected in that work, as cyclobutane may quickly dissociate to ethylene. The yield of cyclohexyl radical (c-$\bullet C_6H_{11}$) from c-C_6H_{12} (reaction (7.7)) was also added to improve the prediction of the 1-hexene concentration profile. Unlike the mechanism proposed by Arikibe et al. (reaction (7.4)), the recombination reaction of $\bullet CH_3$ and $\bullet C_3H_5$ (reaction (7.8)) was postulated as a pathway for the 1-butene production.

$$\text{c-}C_6H_{12} \leftrightarrow \bullet CH_2(CH_2)_4H_2C\bullet \rightarrow \bullet CH_2(CH_2)_2H_2C\bullet + C_2H_4 \rightarrow \text{1-}C_4H_8 + C_2H_4 \tag{7.4}$$

$$\text{c-}C_6H_{12} \leftrightarrow \bullet CH_2(CH_2)_4H_2C\bullet \rightarrow 2\ CH_2{=}CHCH_3 \tag{7.5}$$

$$\text{c-}C_6H_{12} \rightarrow \text{c-}C_4H_8 + C_2H_4 \tag{7.6}$$

$$\text{c-}C_6H_{12} \rightarrow \text{c-}\bullet C_6H_{11} + H\bullet \tag{7.7}$$

$$\bullet CH_3 + \bullet C_3H_5 \rightarrow 1\text{-}C_4H_8 \tag{7.8}$$

Later, Steil et al. conducted the pyrolysis of cyclohexane using the shock tube technique and argued that there was a 1:1 branching ratio between reaction (7.7) and reaction (7.1), and the importance of reaction (7.7) was previously underestimated.[11] It was also stated that the cyclohexyl radical further loses one H atom to form cyclohexene (reaction (7.9)), and several subsequent reactions would occur after that. Granata et al. considered that cyclohexene could be produced directly from cyclohexane by H_2 elimination (reaction (7.10)) in their kinetic modeling of cyclohexane.[12]

$$c\text{-}\bullet C_6H_{11} \rightarrow c\text{-}C_6H_{10} + H\bullet \tag{7.9}$$

$$c\text{-}C_6H_{12} \rightarrow c\text{-}C_6H_{10} + H_2 \tag{7.10}$$

Kiefer et al. performed the thermal decomposition of cyclohexane and 1-hexene by applying the shock tube technique as well as numerical modeling.[13] It was considered that 1-hexene was the main initial product in the cyclohexane pyrolysis, and 1-hexene was consumed predominantly via C3-C4 bond fission (reaction (7.2)). The production of $\bullet C_2H_5 + \bullet C_4H_7$ (reaction (7.11)) and $\bullet CH_3 + \bullet C_5H_9$ (reaction (7.12)) were considered to make a marginal contribution to the overall mechanism. The retro-ene reaction (7.3) was found to be insignificant under their reaction conditions. Liu et al. performed the flash pyrolysis of 1-hexene coupled with vacuum ultraviolet single-photon ionization mass spectrometry (VUV-SPI-MS) and studied its unimolecular decomposition mechanism.[14] They argued that the 1,5-diradical and 1,6-diradical retro-ene reactions leading to the formation of 1,5-hexyl diradical and 1,6-hexyl diradical are important initiation pathways (reaction (7.13a) and (7.13b)) in the 1-hexene thermal decomposition. Recently, some other works which mainly focused on improving the rate coefficients to better quantify the mechanistic models have also been reported.[8, 15-18]

$1\text{-}C_6H_{12} \rightarrow \bullet C_2H_5 + \bullet C_4H_7$ (7.11)

$1\text{-}C_6H_{12} \rightarrow \bullet CH_3 + \bullet C_5H_9$ (7.12)

$1\text{-}C_6H_{12} \rightarrow 1,5\text{-}\bullet C_6H_{12}\bullet$ (7.13a)

$1\text{-}C_6H_{12} \rightarrow 1,6\text{-}\bullet C_6H_{12}\bullet$ (7.13b)

The formation mechanism of the C_6H_6 compounds during the cyclohexane decomposition also drew some attention. Several mechanisms were proposed for the C_6H_6 production. One was a stepwise dehydrogenation mechanism from the parent precursor,[10, 19-22] and the other was bimolecular recombination reactions of smaller species such as C_2H_2 + C_4H_4 or C_3H_3 + C_3H_3.[15, 18, 23-25]

In addition to the experimental investigations mentioned above, quantum chemistry studies have also been performed, and the role of the 1,6-hexyl diradical in the cyclohexane pyrolysis was an emphasis. Sirjean et al. reported a theoretical investigation based on CBS-QB3 calculations on the cycloalkane unimolecular dissociations.[26] The Gibbs free energies of each species of interest including the diradical intermediates were calculated. The C-C bond breaking of cyclohexane producing the 1,6-hexyl diradical was considered as the initiation step, and the barrier for the 1,6-hexyl diradical to further dissociate into 1,4-butyl diradical and ethylene was calculated to be 107 kJ/mol. Kiefer et al. examined the thermal decomposition pathways of cyclohexane and 1-hexene at the CASPT2/cc-pVDZ level.[13] They argued that the 1,6-hexyl diradical could be formed from the ring-opening reaction of cyclohexane, and rapidly isomerizes to 1-hexene as other reactions of 1,6-hexyl diradical are not competitive. Gong et al. explored the decomposition mechanism of cyclohexane at the CCSD(T)/cc-pVDZ//UBH&HLYP/cc-pVDZ level of theory. The reaction pathways of the $\bullet C_6H_{12}\bullet$ diradical (both singlet and triplet) yielding the C_4H_8 species as well as other products were studied.[27] Huang et al. performed a density functional theory (DFT) investigation on the decomposition of cyclohexane in the hydrogen plasma at the B3LYP/6-31G(d,p) level of theory.[28] In that work, the 1,6-hexyl diradical was considered to be a less important reaction intermediate, while the cyclohexane pyrolysis was mainly initiated by C-H bond breaking with the involvement of an active hydrogen atom.

Although many studies on the cyclohexane pyrolysis have been reported, there are still some different opinions on the initial steps. For example, there are questions on the role of the 1,6-hexyl diradical in the cyclohexane decomposition, and if or not it has direct dissociation pathways in the unimolecular reaction regime. In previous works, either the reaction time or the product detection time was long, and therefore the bimolecular reactions could not be avoided; the unimolecular reactivity of the 1,6-hexyl diradical was rather unclear. Other reaction mechanisms such as the formation of the cyclohexyl radical and benzene could also be re-examined under the unimolecular reaction conditions. These motivate further studies to focus on the initial steps of the unimolecular dissociation of cyclohexane. Here, we provide a different approach, using flash pyrolysis of diluted cyclohexane in inert carrier gas (~ 1%) in a short reaction time (< 100 μs), which can mainly focus on the initiation pathways of the unimolecular thermal decomposition of cyclohexane. In this chapter, evidence for the 1,6-hexyl diradical and its direct dissociation was exhibited. The $\bullet C_6H_{11}$ radical was not detected in this chapter. Therefore, the initial reactions of cyclohexane were primarily explained by the ring-opening and diradical mechanism. The formation mechanism of the C_6H_6 species was also examined in this chapter.

7.2 Experimental and computational methods

The flash pyrolysis of cyclohexane was carried out by employing a vacuum ultraviolet photoionization time-of-flight mass spectrometer (VUV-PI-TOFMS) coupled with a SiC tubular microreactor, which has been described previously.[29-32] The cyclohexane precursor (99.9%, Fisher Scientific) was diluted to around 1% in the N_2 or helium carrier gas. The gas mixture passed through a pulse valve operated at 10 Hz and expanded into the SiC microreactor. The dimensions of the SiC microreactor were depicted in Scheme 7.2.

Quantum chemistry calculations were also performed on the energies of the reactants, products, and transition states involved in the cyclohexane pyrolysis. Cyclohexane is known for its 3 common conformers: chair, boat, and twist boat. Only the chair conformer, the lowest energy conformer, was chosen because the three have similar energies and relatively small isomerization barriers.[26] For the same reason, only the lowest

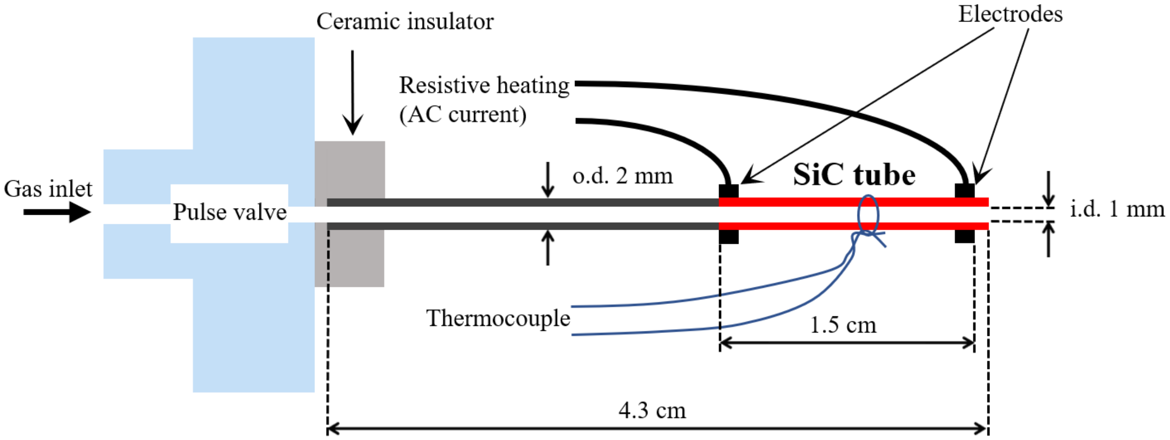

Scheme 7.2 Schematic diagram of the SiC microreactor.

energy conformer for each diradical was considered. The geometries of species of interest were optimized using the UB3LYP method with the cc-pVDZ basis sets. It could yield reliable geometries compared to those with more advanced computational approaches.[26, 33] All transition states were verified using intrinsic reaction coordinate (IRC) calculations at the UB3LYP/cc-pVDZ level. The single-point energy was calculated using the UCCSD(T) method (with full treatment of single and double excitations and an estimate to the non-iteratively calculated triple excitation contributions) and cc-pVDZ basis sets. The zero-point energy (ZPE) corrections were made based on the frequency calculations at the UB3LYP/cc-pVDZ level. In addition, the energies of singlet diradicals in this chapter were calculated using $E_{singlet} = 2E_{Guess=Mix} - E_{triplet}$,[34, 35] in which the energy of the diradical with the "Guess=Mix" option was assumed to be the average of the single point energies of its singlet configuration and triplet configuration. This method was first proposed by Ziegler et al in order to deal with the unsatisfactory spin contaminations caused by significant mixing between the singlet and triplet states of diradicals.[27, 34, 35] All vibrational frequencies were scaled by 0.97 in this chapter as recommended by Sinha et al..[36] The single-reference calculation approach in this chapter was similar to the method employed in Gong et al.[27] All the computational works in this chapter were employed using Gaussian 09 package.[37]

7.3 Results and discussions

(a) Initiation reactions

The mass spectra of thermal decomposition of cyclohexane from 295 K to 1310 K are presented in Figure 7.1 and 7.2. At 295 K, *m/z* = 84 and 85 correspond to the signal of the cyclohexane parent molecule. The natural isotope abundance of ^{12}C : ^{13}C is 98.9 : 1.1

and H : D = 99.98 : 0.02.[38] The peak area ratio of *m/z* = 85 to 84 was measured to be 0.083, close to the expected value of 0.074. The ionization energy (IE) of cyclohexane is 9.82 eV,[39] which is lower than the VUV photon energy (10.49 eV). The minor signal of *m/z* = 56 (C_4H_8) and *m/z* = 55 (C_4H_7) at 295 K, prior to any contributions from thermal decomposition, were caused by a small amount of multiphoton or electron impact ionization fragmentation of the parent molecule, as the appearance energy of $C_4H_8^+$ and $C_4H_7^+$ in the photoionization of cyclohexane are larger than 10.49 eV.[40] The small amount of electron impact ionization could be resulted from photoelectrons produced by scattered VUV radiation within the photoionization region.[46] At 295 K, *m/z* = 28 corresponded to the signal of $[N_2]^+$, as N_2 was the inert carrier gas utilized in this cyclohexane pyrolysis. Although the IE of N_2 is 15.6 eV[41] which is higher than 10.49 eV, the minor signal was due to a small amount of electron impact or multiphoton ionization of the N_2 molecules.[42] As will be discussed later, when the temperature increased, the increase of the *m/z* = 28 peak could also correspond to the signal of neutral C_2H_4 molecules produced by thermal dissociations. Note that N_2 (m/z = 28.01) and C_2H_4 (m/z = 28.05) mass peaks could not be resolved by the mass spectrometer in this chapter.

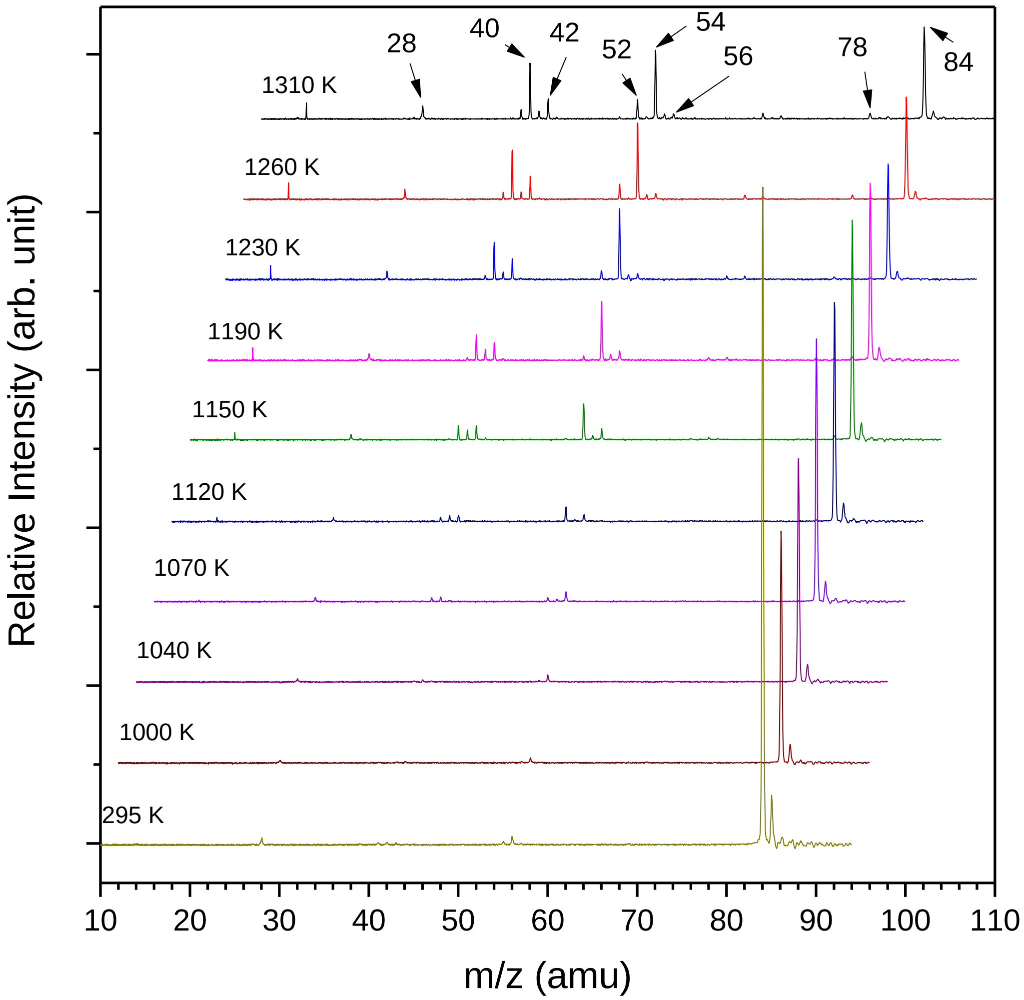

Figure 7.1 Mass spectra for the cyclohexane pyrolysis at 295 K to 1310 K. Four mass spectra at temperatures between 540 K and 940 K were identical to that at 1000 K and were omitted. The mass spectra are offset horizontally for clarity.

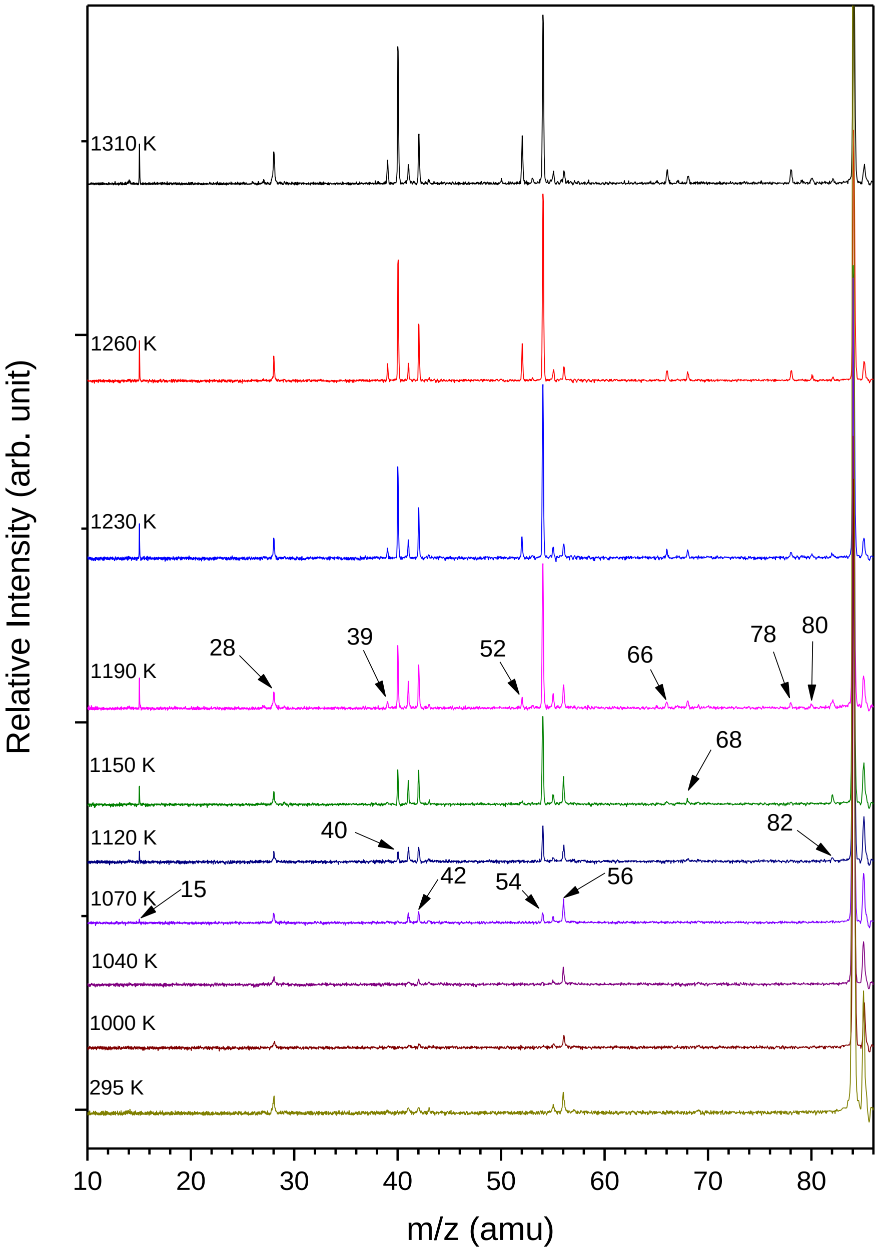

Figure 7.2 Enlarged sections of mass spectra for the cyclohexane pyrolysis at 295 K to 1310 K. Four mass spectra at temperatures between 540 K and 940 K were identical to that at 1000 K and were omitted. The relative intensity scale is the same for all the mass spectra, but the vertical space is adjusted to better show peaks of fragments at elevated temperatures.

Experimental evidence for the direct dissociation of the 1,6-hexyl diradical was identified. As shown in Figure 7.1 and 7.2, the *m/z* = 56 peak was detected as a minor ionization fragmentation peak of the parent molecule at 295 K, and it started to increase in intensity at around 1070 K. The signal kept growing until at ~ 1190 K and remained approximately constant as the temperature further increased. To better illustrate the contributions to the signals from thermal decomposition,[29] the ratios of fragment peak areas relative to the parent are plotted for several species in Figure 7.3**.** The ratio of *m/z* = 56 mass peak area to the parent (*m/z* = 84) shows that at around 1070 K, *m/z* = 56 peak (C_4H_8)

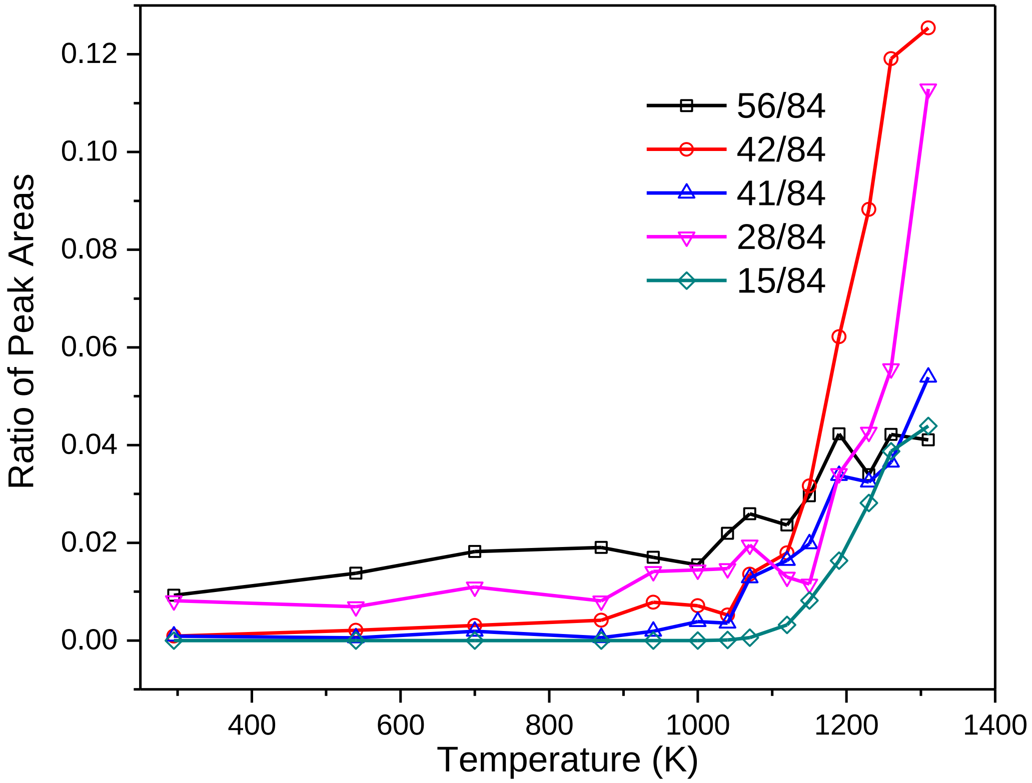

Figure 7.3 The ratio of peak area of several fragment peaks against the parent peak in the cyclohexane pyrolysis.

started to grow, and the ratio further increased with the temperature. The reaction (7.4) is a likely reaction pathway for cyclohexane to decompose into C_4H_8 and C_2H_4 through the 1,6-hexyl diradical intermediate.[9, 14] The absence of *m/z* = 57 peak (C_4H_9) at all temperatures suggests that the C_4H_8 species was not produced from H-atom loss from the C_4H_9 radical. This is consistent with Kiefer et al. that the C2-C3 bond fission was not feasible for 1-hexene, which was the major isomerization product following the 1,6-hexyl diradical in the cyclohexane pyrolysis (reaction (7.1)).[13] Also, since bimolecular reactions were minimized by short reaction time and low precursor concentrations, the bimolecular recombination reaction of $\bullet C_3H_5$ and $\bullet CH_3$ to form C_4H_8 (reaction (7.8)) was unlikely; furthermore, C_4H_8 was already formed prior to a significant amount of $\bullet C_3H_5$ and $\bullet CH_3$ were produced. Hence, the increase of the *m/z* = 56 signal at around 1070 K indicated that C_4H_8 was evolved from breaking of the C2-C3 single bond in the $\bullet C_6H_{12}\bullet$ diradical, and this was also the evidence of the existence of the $\bullet C_6H_{12}\bullet$ diradical intermediate.

Similar observations have been made in the pyrolysis of 1-hexene by Liu et el. under similar experimental conditions.[14] Although with a different precursor 1-hexene, the $\bullet C_6H_{12}\bullet$ diradical was formed in both cyclohexane and 1-hexene pyrolysis due to isomerization. In that work, the *m/z* = 56 peak was found increasing significantly at around

990 K, and it could only be explained by the secondary decompositions of 1,5- and 1,6-hexyl diradical which were produced from the isomerization reactions of 1-hexene.

The mechanism proposed above that 1,6-hexyl diradical could directly decompose to the *m/z* = 56 product was also supported by quantum chemistry investigations carried out in this chapter. In Figure 7.4, several possible competing reaction pathways and their energetics that lead to the formation of the *m/z* = 56 peak are displayed. The C-C bond rupture producing •C_6H_{12}• via TS1 was considered as the initiation step of the cyclohexane decomposition, and the energy barrier was determined to be 359.5 kJ/mol relative to

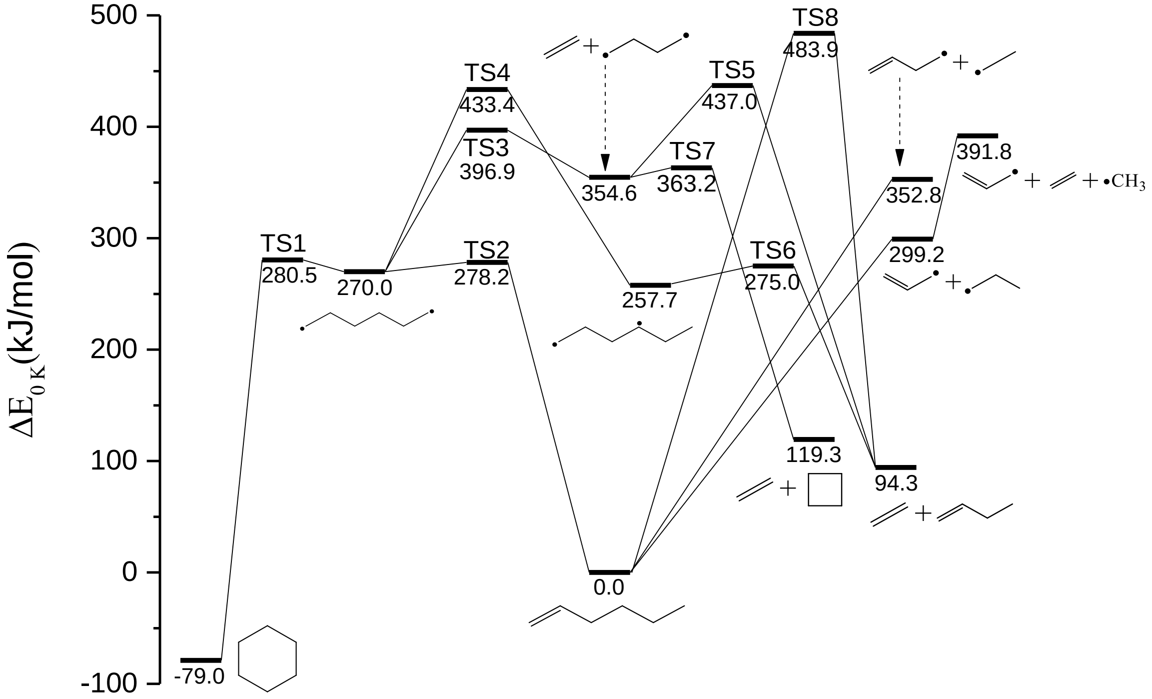

Figure 7.4 Possible reaction pathways leading to the formation of the m/z = 56 products, along with some dissociation channels of 1-hexene following isomerization of the 1,6-hexyl diradical. All geometry optimizations and zero-point energy corrections were made at the UB3LYP/cc-pVDZ level. The single-point electronic energies of all species involved were performed at the UCCSD(T)/cc-pVDZ level of theory. The relative energy differences at 0 K were used as the starting reference values.

cyclohexane. After the formation of $\bullet C_6H_{12}\bullet$, 1-hexene could be produced by overcoming TS2 with an 8.2 kJ/mol energy barrier from the 1,6-hexyl diradical intermediate. Figure 7.4 shows that the isomerization between cyclohexane and 1-hexene can readily take place compared to other reaction pathways. Our theoretical calculations on the initial pathways of 1-hexene isomerization through the 1,6-hexyl diradical intermediate are in agreement with Liu et al. at MRCI(8e,8o)/cc-pVTZ level.[14] In Liu et al., the energy difference between 1-hexene and the 1,6-hexyl diradical was determined to be 278.6 kJ/mol, while in this work the corresponding value is 270.0 kJ/mol. The height of the energy barrier between the transition state TS2 and the 1,6-hexyl diradical was calculated to be 8.8 kJ/mol,[14] similar to 8.2 kJ/mol in this work. The 1,6-hexyl radical could decompose into $\bullet C_4H_8\bullet$ and C_2H_4 through TS3, which requires overcoming an additional barrier of 126.9 kJ/mol (this could take place via thermal activation of the 1,6-hexyl radical by additional collisions with the buffer gas). The $\bullet C_4H_8\bullet$ 1,4-butyl diradical could further take two possible pathways, isomerization to cyclobutane via TS7 with an energy barrier of 8.6 kJ/mol, or formation of 1-butene with a threshold energy of 82.4 kJ/mol via TS5. The detailed geometries of the species involved could be found in the Supplemental Materials.

As the co-product of C_4H_8 in reaction (7.4), $m/z = 28$ (C_2H_4) peak seemed to appear around 1070 K and became more obvious at temperatures above 1200K (Figure 7.2 and 7.3), although this onset and trend were not well defined. This was possibly because the IE of ethylene (10.51 eV[43]) is slightly higher than the VUV photon energy (10.49 eV), and more significantly because the background signal of N_2^+ made the detection of the ethylene signal difficult. To eliminate the influence of N_2 on the detection of $m/z = 28$ signal, the pyrolysis of cyclohexane was also performed using helium as a carrier gas under similar thermal decomposition conditions. Without the background signal of N_2 at $m/z = 28$, the $m/z = 28$ signal was first detected at about the same temperature where the $m/z = 56$ species started to be formed. Also, in the mass spectra using the helium carrier gas, the C_2H_4 signal was found to show up at a similar temperature when the $m/z = 15$ peak appeared, as the secondary decomposition of $\bullet C_3H_7$ producing $\bullet CH_3$ and C_2H_4 could also contribute to the appearance of the $m/z = 15$ and 28 peaks. In this chapter, as shown in Figure 7.2 and 7.3, the $m/z = 15$ signal first appeared at 1070 K, which indicated that ethylene could also start to show up at the similar temperature of ~ 1070 K.

In addition to the reaction mechanism mentioned above, several other competing reaction pathways leading to the formation of $m/z = 56$ species are considered, and the calculated energetics are depicted in Figure 7.4. The 1,6-hexyl diradical could isomerize to 1,4-hexyl diradical via TS4, followed by 1-butene formation; this reaction pathway requires 163.4 kJ/mol additional energy to go over TS4 from the $\bullet C_6H_{12}\bullet$ diradical. 1-butene produced directly from 1-hexene via TS8 is also considered; however, the energy threshold is determined to be 483.9 kJ/mol relative to 1-hexene. This reaction channel requires the highest amount of energy, which is the least likely explanation for the $m/z = 56$ peak. In summary, according to the theoretical calculations (Figure 7.4), the most favored pathway for the formation of the C_4H_8 species is that cyclohexane decomposes into the 1,6-hexyl diradical followed by the C2-C3 bond breaking of the 1,6-hexyl diradical in the secondary reaction (likely activated by additional collisions with the buffer gas), which leads to the formation of 1,4-butyl diradical. Then the 1,4-butyl diradical could isomerize to cyclobutane via TS7 or to 1-butene via TS5. Although the formation of 1-hexene was the reaction channel with the lowest energy barrier among the secondary reactions of the $\bullet C_6H_{12}\bullet$ diradical, the formation of $m/z = 56$ could not be readily explained by the direct dissociation of 1-hexane due to the high energy barrier of TS8. And this supports the conclusion in the previous investigation carried by Liu et al. that 1-hexene has to go through the $\bullet C_6H_{12}\bullet$ diradical to form the C_4H_8 species.[14]

In Sirjean et al., the rate constants for different potential pathways of the 1,6-hexyl diradical were determined at 1 atm pressure, from 600 K to 2000 K.[26] Under such condition, the reaction of the 1,6-hexyl diradical leading to 1-hexene was considered to be more important than that to the C_4H_8 species, as the C_4H_8 species had not been observed as a unimolecular dissociation product previously.[6, 26] In this chapter, thermal decomposition production of the C_4H_8 species was identified. However, it was difficult and inconclusive to quantify the kinetics in this chpater, due to the complexity in the experimental conditions (e.g., non-uniformity of pressure and temperature). Therefore, this chapter mainly focused on the qualitative analysis of the kinetics in the microreactor.

Cyclohexane isomerizing to 1-hexene is an important mechanism in the thermal dissociation of cyclohexane. Several mass peaks likely produced from the decomposition of 1-hexene were also identified in this chapter. Figure 7.1 and 7.2 show that when the temperature reached ~1070 K, the peaks at $m/z = 41$ and 42 started to appear and grew significantly at higher temperatures, indicating the production of $\bullet C_3H_5$ and C_3H_6. The peak area ratio of m/z 41/84 ($\bullet C_3H_5$ versus C_6H_{12}) in Figure 7.3 was nearly constant below 1070 K and started to increase at around 1070 K. The formation of the $m/z = 41$ peak ($\bullet C_3H_5$) is known from the following steps: cyclohexane first isomerizes to 1-hexene via the diradical intermediate (reaction (7.1)), then 1-hexene undergoes C3-C4 bond homolysis (reaction (7.2)). $\bullet C_3H_5$ was less likely to be produced via H-loss secondary reaction from the propene product under our experimental condition, as propene has a strong C-H bond.[6, 9, 13, 15] According to Figure 7.1 and 7.2, the signal *m/z* = 43 ($\bullet C_3H_7$), which was the counterpart of $\bullet C_3H_5$ in reaction (7.2), was detected with a minor amount at 1070 K. It increased more at ~ 1150 K but remained very small. This was possibly due to the unstable nature of the *n*-propyl radical $\bullet C_3H_7$, which further decomposed rapidly into methyl radical and ethylene (reaction (7.14)) or, to a lesser extent, propene and H (reaction (7.15)).[13, 14, 44, 45] The observation of the *m/z* = 15 peak at 1070 K, as well as the arguments mentioned previously that ethylene was captured at around 1070 K, was consistent with the assumption that $\bullet C_3H_7$ was unstable and decomposed rapidly.

$$\bullet C_3H_7 \rightarrow \bullet CH_3 + C_2H_4 \qquad (7.14)$$

$$\bullet C_3H_7 \rightarrow H\bullet + C_3H_6 \qquad (7.15)$$

As shown in the mass spectra in Figure 7.2 and peak area ratio of *m/z* 42/84 in Figure 7.3, the *m/z* = 42 species were produced at ~1070 K. There are several possible sources of C_3H_6 formation. It could be evolved from 1-hexene after the initial isomerization from cyclohexane, which decomposed through a retro-ene mechanism into two propene molecules (reaction (7.3)),[6, 14, 46] although this was later considered to be not important.[13, 14] It could also be originated from the $\bullet C_6H_{12}\bullet$ diradical as described in reaction (7.5): cyclohexane first broke a C-C bond forming the 1,6-hexyl diradical followed by isomerization to 1,5-hexyl diradical or 2,5-hexyl diradical, leading to propene plus cyclopropane or two propene molecules via symmetric C-C breaking, or the symmetric C-C bond breaking of the 1,6-hexyl diradical could directly lead to the formation of two cyclopropane (reaction (7.16)).[13, 14, 26] As discussed earlier, to a lesser extent, it was also possible to be produced from the secondary decomposition of the n-propyl radical, losing one H to form propene (reaction (7.15)).

$$c\text{-}C_6H_{12} \leftrightarrow \bullet CH_2(CH_2)_4H_2C\bullet \rightarrow 2\ c\text{-}C_3H_6 \tag{7.16}$$

Some other reaction products associated with 1-hexene following the isomerization of cyclohexane through the 1,6-hexyl diradical (reaction (7.1)) were observed. The *m/z* = 55 peak, which corresponds to $\bullet C_4H_7$, was found to increase significantly at around 1070 K, and its intensity kept nearly constant until the temperature reached around 1310 K as shown in Figure 7.1 and 7.2. It was likely produced by the C4-C5 bond fission of 1-hexene. It could also be produced from the H-loss secondary reactions of 1-butene at high temperatures. The co-product of $\bullet C_4H_7$ in reaction (7.11), $\bullet C_2H_5$ (*m/z* = 29), was not observed at all temperatures, although its ionization energy is 8.12 eV,[47] below the 10.49 eV VUV photon energy in this work. This was probably caused by the fast dissociation of $\bullet C_2H_5$ which led to the formation of C_2H_4 + H.[48] According to Figure 7.1 and 7.2, at 1150 K, *m/z* = 68 was first observed, and its intensity kept almost constant when the temperature further increased. The *m/z* = 68 peak was possibly the H-loss reaction product of $\bullet C_5H_9$ radical, which could be produced in reaction (7.12) from 1-hexene. There was a very minor amount of *m/z* = 69 signal around these temperatures.

The decomposition channels of 1-hexene were also examined theoretically. The DFT calculations on some of the dissociation channels of 1-hexene are presented in Figure

7.4. It shows that reaction (7.2) only requires an additional energy barrier of 299.2 kJ/mol relative to 1-hexene which makes it the most competitive dissociation channel among all, while reaction (7.11) has an energy barrier of 352.8 kJ/mol. Those two reaction channels have lower energy thresholds than the lowest possible threshold energy of the formation of the *m/z* = 56 species. The further secondary reaction of the $\bullet C_3H_7$ radical producing C_2H_4 and $\bullet CH_3$ is displayed with its energetics in Figure 7.4 as well. An additional 92.6 kJ/mol energy barrier needs to be overcome for the $\bullet C_3H_7$ radical, which makes the overall energy barrier for the formation of ethylene + $\bullet CH_3$ to be around 470.8 kJ/mol from cyclohexane. Note that this energy is about the same as the overall energy barrier of TS3 (475.9 kJ/mol relative to cyclohexane), which leads to the C_4H_8 product. The observation of the ethylene + $\bullet CH_3$ products and the C_4H_8 product around the same onset temperature in this chapter was consistent with these two similar energy barriers.

The theoretical investigations along with the experimental observations discussed above suggested that the predominant thermal decomposition reaction channels of cyclohexane pyrolysis were carried out via 1-hexene. This is consistent with previous investigations on the thermal decomposition of cyclohexane and 1-hexene, in which both species show many features in common in their pyrolysis processes. However, the secondary reactions of the hexyl-diradicals were often omitted, and in this chapter, both experimental and theoretical studies have shown that the secondary reactions of the 1,6-hexyl diradical are important among the unimolecular reactions. Consequently, the impact of the diradicals on the overall pyrolysis mechanism of similar cycloalkane systems needs to be evaluated.

At all temperatures in this chapter, *m/z* = 83 peak (•C_6H_{11}) was not detected. However, •C_6H_{11} has an ionization energy of 7.66 eV[49] and can be detected by the 10.49 eV VUV laser radiation used in this chapter, and it was detected in the pyrolysis of methylcyclohexane under the similar experimental conditions.[50] Therefore, H-atom loss (reaction (7.9)) was not one of the initiation steps of cyclohexane pyrolysis. This is understandable because the C-H bond (~410.9 kJ/mol) is much stronger than the C-C bond (~346.0 kJ/mol) in cyclohexane, which required more energy to break among the primary dissociation pathways under the unimolecular decomposition conditions. The cyclohexyl radical observed in some of the earlier studies under different conditions was likely produced from bimolecular reactions.[13, 15] In return, the absence of the *m/z* = 83 cyclohexyl signal in this work confirmed that bimolecular reactions were indeed minimized under the current experimental conditions.

When the temperature reached 1120 K, the *m/z* = 82 peak started to appear, and it most likely represented the signal of cyclohexene. According to the discussion above, cyclohexene was produced by the H_2 elimination reaction of cyclohexane (reaction (7.10)). When the temperature reached 1190 K and above, *m/z* = 80 and 78 started to appear subsequently, and *m/z* = 78 kept growing as the temperature increased. As shown in Figure 7.1 and 7.2, the signals of further H_2 elimination products such as *m/z* = 76 or 74 were not observed, which indicated that *m/z* = 78 was very stable at high temperatures and unlikely to be an open-chain unsaturated hydrocarbon. This further supports that the *m/z* = 78 product likely corresponded to benzene. As the bimolecular reactions were minimized under the current experimental conditions, benzene at m/z = 78 was not likely produced from recombination of small fragments, and therefore, it should be formed from sequential H_2 eliminations (reaction (7.17)), while the cyclohexyl radical was not detected.

$$\text{c-}C_6H_{12} \xrightarrow{-H_2} \text{c-}C_6H_{10} \xrightarrow{-H_2} \text{c-}C_6H_8 \xrightarrow{-H_2} C_6H_6 \qquad (7.17)$$

(b) Secondary reactions in cyclohexane pyrolysis

The decomposition fragments of cyclohexane after the initiation reactions went through a series of secondary reactions. The *m/z* = 40 and 39 peaks, which first showed up after 1120 K, were produced by the secondary reactions of the allyl radical and propene. The energetics of allyl radicals and propene have been examined theoretically and experimentally previously.[51, 52] Besides the pathways that lead to the formation of the C_3H_4 and C_3H_3 species, allyl radical could also decompose into C_2H_2 and $\bullet CH_3$ radical.[52] The *m/z* = 54 peak first appeared at 1070 K and it represented 1,3-butadiene. The *m/z* = 52 peak represented 1-buten-3-yne (or cyclobutadiene) and it was first observed at 1190 K. The peak intensities of these two peaks increased as the temperature further increased. They were evolved from sequential H_2 loss of C_4H_8 (1-butene or cyclobutane) or H-loss of the $\bullet C_4H_7$ radical. Also, the secondary decomposition of cyclohexene could contribute to the yields of 1,3-butadiene (known as retro-Diels Alder mechanism).[53] The *m/z* = 68 (C_5H_8) and 66 (C_5H_6) peaks, which were first observed at around 1190 K, could be explained by the secondary reactions of the $\bullet C_5H_9$ radical produced in reaction (7.12). To summarize, important initiation steps and part of the secondary reactions for the thermal decomposition of cyclohexane are depicted in Scheme 7.3.

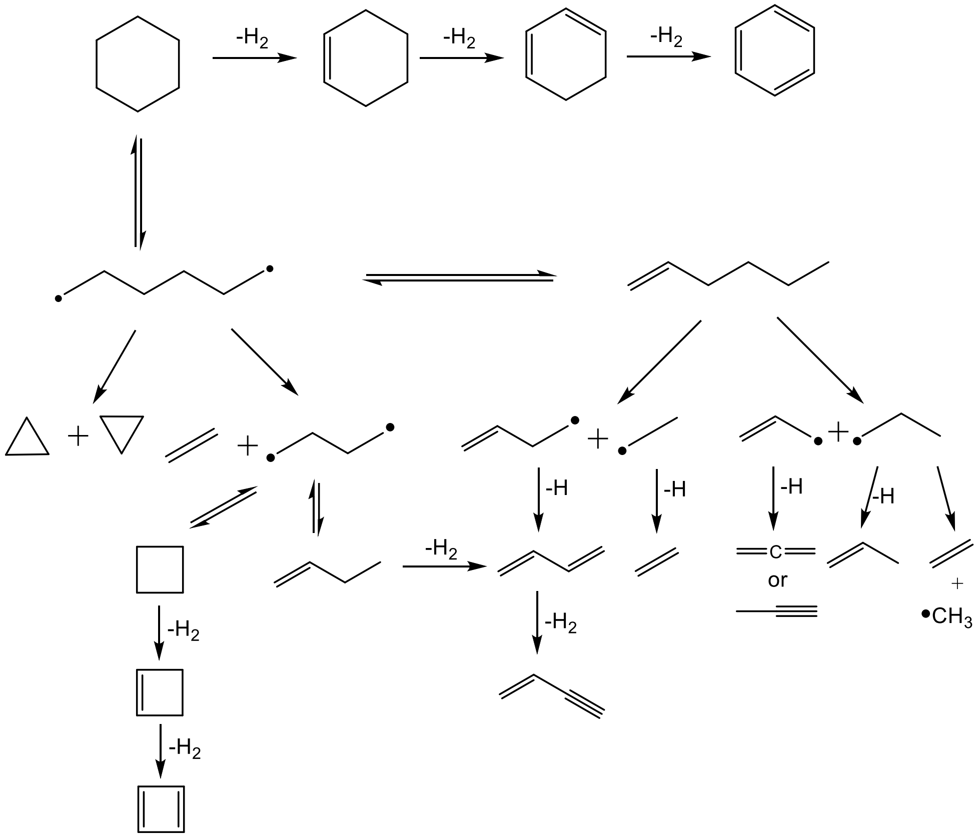

Scheme 7.3 Main initiation decomposition mechanism of cyclohexane.

7.4 Conclusion

The thermal decomposition of cyclohexane was studied by flash pyrolysis coupled with molecular beam sampling and VUV-PI-MS in this chapter. The C-C bond rupture of cyclohexane producing the 1,6-hexyl diradical was the main initiation reaction pathway. The *m/z* = 56 species was produced primarily by the direct dissociation reaction of the 1,6-hexyl diradical under unimolecular reaction conditions, and it was unlikely to be formed through 1-hexene which was the important isomerization product of the 1,6-hexyl diradical. Experimental observations and quantum chemistry investigations in this chapter were consistent with this mechanism. This chapter also shows that the pyrolysis of cyclohexane did not produce the $\bullet C_6H_{11}$ radical by C-H bond fission. Direct evidence for the sequential H_2 eliminations to form $m/z = 82$ (c-C_6H_{10}), 80 (c-C_6H_8), and 78 (benzene) were found.

This chapter, as well as the previous work on the 1-hexene and 1-heptene pyrolysis by Liu et al.,[14] have demonstrated the significance of the direct dissociation pathways of hydrocarbon diradicals and can provide insight into further numerical modeling studies on similar cycloalkane systems.

REFERENCE

1. G. W. Huber, S. Iborra and A. Corma, *Chemical Reviews*, 2006, **106**, 4044-4098.

2. A. M. Mastral and M. S. Callén, *Environmental Science & Technology*, 2000, **34**, 3051-3057.

3. E. Ranzi, A. Cuoci, T. Faravelli, A. Frassoldati, G. Migliavacca, S. Pierucci and S. Sommariva, *Energy & Fuels*, 2008, **22**, 4292-4300.

4. W. Jin, L. Pastor-Pérez, D. Shen, A. Sepúlveda-Escribano, S. Gu and T. Ramirez Reina, *ChemCatChem*, 2019, **11**, 924-960.

5. L. Mo, W. Yu, H. Cai, H. Lou and X. Zheng, *Frontiers in Chemistry*, 2018, **6**, 1-8.

6. W. Tsang, *International Journal of Chemical Kinetics*, 1978, **10**, 1119-1138.

7. T. C. Brown, K. D. King and T. T. Nguyen, *The Journal of Physical Chemistry*, 1986, **90**, 419-424.

8. D. S. Aribike and A. A. Susu, *Applied Petrochemical Research*, 2018, **8**, 193-201.

9. D. S. Aribike, A. A. Susu and A. F. Ogunye, *Thermochimica Acta*, 1981, **51**, 113-127.

10. A. El Bakali, M. Braun-Unkhoff, P. Dagaut, P. Frank and M. Cathonnet, *Proceedings of the Combustion Institute*, 2000, **28**, 1631-1638.

11. U. Steil, M. Braun-Unkhoff, C. Naumann and P. Frank, in *Proceedings of the European Combustion Meeting*, Louvain-la-Neuve, Belgium, April 3−6, 2005.

12. S. Granata, T. Faravelli and E. Ranzi, *Combustion and Flame*, 2003, **132**, 533-544.

13. J. H. Kiefer, K. S. Gupte, L. B. Harding and S. J. Klippenstein, *The Journal of Physical Chemistry A*, 2009, **113**, 13570-13583.

14. X. Liu, W. Yuan, J. Zhang, J. Yang and Z. Zhou, *Proceedings of the Combustion Institute*, 2020, https://doi.org/10.1016/j.proci.2020.1007.1060.

15. Z. Wang, Z. Cheng, W. Yuan, J. Cai, L. Zhang, F. Zhang, F. Qi and J. Wang, *Combustion and Flame*, 2012, **159**, 2243-2253.

16. S. Peukert, C. Naumann, M. Braun-Unkhoff and U. Riedel, *International Journal of Chemical Kinetics*, 2011, **43**, 107-119.

17. I. G. Zsély, T. Varga, T. Nagy, M. Cserháti, T. Turányi, S. Peukert, M. Braun-Unkhoff, C. Naumann and U. Riedel, *Energy*, 2012, **43**, 85-93.

18. M. K. Liszka and K. Brezinsky, *International Journal of Chemical Kinetics*, 2019, **51**, 49-73.

19. D. Voisin, A. Marchal, M. Reuillon, J. C. Boettner and M. Cathonnet, *Combustion Science and Technology*, 1998, **138**, 137-158.

20. O. Lemaire, M. Ribaucour, M. Carlier and R. Minetti, *Combustion and Flame*, 2001, **127**, 1971-1980.

21. F. Billaud, P. Chaverot, M. Berthelin and E. Freund, *Industrial & Engineering Chemistry Research*, 1988, **27**, 759-764.

22. W. Li, M. E. Law, P. R. Westmoreland, T. Kasper, N. Hansen and K. Kohse-Höinghaus, *Combustion and Flame*, 2011, **158**, 2077-2089.

23. C. S. McEnally and L. D. Pfefferle, *Combustion and Flame*, 2004, **136**, 155-167.

24. K. H. Weber and J. Zhang, *The Journal of Physical Chemistry A*, 2007, **111**, 11487-11492.

25. M. V. Khandavilli, M. Djokic, F. H. Vermeire, H.-H. Carstensen, K. M. Van Geem and G. B. Marin, *Energy & Fuels*, 2018, **32**, 7153-7168.

26. B. Sirjean, P. A. Glaude, M. F. Ruiz-Lopez and R. Fournet, *The Journal of Physical Chemistry A*, 2006, **110**, 12693-12704.

27. C.-M. Gong, Z.-R. Li and X.-Y. Li, *Energy & Fuels*, 2012, **26**, 2811-2820.

28. X. Huang, D. Cheng, F. Chen and X. Zhan, *Journal of Energy Chemistry*, 2015, **24**, 65-71.

29. K. Shao, Y. Tian and J. Zhang, *International Journal of Mass Spectrometry*, 2021, **460**, 116476.

30. X. Liu, J. Zhang, A. Vazquez, D. Wang and S. Li, *The Journal of Physical Chemistry A*, 2019, **123**, 10520-10528.

31. S. D. Chambreau, J. Zhang, J. C. Traeger and T. H. Morton, *International Journal of Mass Spectrometry*, 2000, **199**, 17-27.

32. D. W. Kohn, H. Clauberg and P. Chen, *Review of Scientific Instruments*, 1992, **63**, 4003-4005.

33. E. Kraka and D. Cremer, *Journal of the American Chemical Society*, 2000, **122**, 8245-8264.

34. D. H. Ess, E. R. Johnson, X. Hu and W. Yang, *The Journal of Physical Chemistry A*, 2011, **115**, 76-83.

35. T. Ziegler, A. Rauk and E. J. Baerends, *Theoretica chimica acta*, 1977, **43**, 261-271.

36. P. Sinha, S. E. Boesch, C. Gu, R. A. Wheeler and A. K. Wilson, *The Journal of Physical Chemistry A*, 2004, **108**, 9213-9217.

37. G. W. T. M. J. Frisch, H. B. Schlegel, G. E. Scuseria, M. A. Robb, J. R. Cheeseman, G. Scalmani, V. Barone, B. Mennucci, G. A. Petersson, H. Nakatsuji, M. Caricato, X. Li, H. P. Hratchian, A. F. Izmaylov, J. Bloino, G. Zheng, J. L. Sonnenberg, M. Hada, M. Ehara, K. Toyota, R. Fukuda, J. Hasegawa, M. Ishida, T. Nakajima, Y. Honda, O. Kitao, H. Nakai, T. Vreven, J. A. Montgomery, Jr., J. E. Peralta, F. Ogliaro, M. Bearpark, J. J. Heyd, E. Brothers, K. N. Kudin, V. N. Staroverov, R. Kobayashi, J. Normand, K. Raghavachari, A. Rendell, J. C. Burant, S. S. Iyengar, J. Tomasi, M. Cossi, N. Rega, J. M. Millam, M. Klene, J. E. Knox, J. B. Cross, V. Bakken, C. Adamo, J. Jaramillo, R. Gomperts, R. E. Stratmann, O. Yazyev, A. J. Austin, R. Cammi, C. Pomelli, J. W. Ochterski, R. L. Martin, K. Morokuma, V. G. Zakrzewski, G. A. Voth, P. Salvador, J. J. Dannenberg, S. Dapprich, A. D. Daniels, Ö. Farkas, J. B. Foresman, J. V. Ortiz, J. Cioslowski, and D. J. Fox, *Gaussian 09*, (2009), Wallingford, CT.

38. J. Meija, B. Coplen Tyler, M. Berglund, A. Brand Willi, P. De Bièvre, M. Gröning, E. Holden Norman, J. Irrgeher, D. Loss Robert, T. Walczyk and T. Prohaska, *Pure and Applied Chemistry*, 2016, **88**, 265-291.

39. L. W. Sieck and M. Mautner, *The Journal of Physical Chemistry*, 1982, **86**, 3646-3650.

40. Y. L. Sergeev, M. E. Akopyan, F. I. Vilesov and Y. V. Chizhov, *High Energy Chem.*, 1973, **369**, 418 in original.

41. M. Grade, J. Wienecke, W. Rosinger and W. Hirschwald, *Berichte der Bunsengesellschaft für physikalische Chemie*, 1983, **87**, 355-361.

42. S. D. Chambreau, J. Lemieux, L. Wang and J. Zhang, *The Journal of Physical Chemistry A*, 2005, **109**, 2190-2196.

43. K. Ohno, K. Okamura, H. Yamakado, S. Hoshino, T. Takami and M. Yamauchi, *The Journal of Physical Chemistry*, 1995, **99**, 14247-14253.

44. L. E. Gusel'nikov, V. V. Volkova, P. E. Ivanov, S. V. Inyushkin, L. V. Shevelkova, G. Zimmermann, U. Ziegler and B. Ondruschka, *Journal of Analytical and Applied Pyrolysis*, 1991, **21**, 79-93.

45. V. V. Volkova, L. E. Gusel'nikov and G. Zimmermann, *Journal of Analytical and Applied Pyrolysis*, 1992, **23**, 265-286.

46. M. Yahyaoui, N. Djebaïli-Chaumeix, C. E. Paillard, S. Touchard, R. Fournet, P. A. Glaude and F. Battin-Leclerc, *Proceedings of the Combustion Institute*, 2005, **30**, 1137-1145.

47. B. Ruscic, J. Berkowitz, L. A. Curtiss and J. A. Pople, *The Journal of Chemical Physics*, 1989, **91**, 114-121.

48. A. F. Wagner, L. A. Rivera-Rivera, D. Bachellerie, J. W. Perry and D. L. Thompson, *The Journal of Physical Chemistry A*, 2013, **117**, 11624-11639.

49. R. F. Pottie, A. G. Harrison and F. P. Lossing, *Journal of the American Chemical Society*, 1961, **83**, 3204-3206.

50. K. H. Weber, University of California, Riverside 2010.

51. F. H. Vermeire, R. De Bruycker, O. Herbinet, H.-H. Carstensen, F. Battin-Leclerc, G. B. Marin and K. M. Van Geem, *Fuel*, 2017, **208**, 779-790.

52. B. S. Narendrapurapu, A. C. Simmonett, H. F. Schaefer, J. A. Miller and S. J. Klippenstein, *The Journal of Physical Chemistry A*, 2011, **115**, 14209-14214.

53. Q. Guan, K. N. Urness, T. K. Ormond, D. E. David, G. Barney Ellison and J. W. Daily, *International Reviews in Physical Chemistry*, 2014, **33**, 447-487.

CHAPTER 8 Flash pyrolysis vacuum ultraviolet photoionization mass spectrometry of cycloheptane

8.1 Introduction

Thermal decomposition of cycloalkanes is an important process in hydrocarbon fuel usage and transformation and biomass conversion.[1-5] Many studies have been reported on the thermal decomposition mechanism of cyclohexane and its isomer 1-hexene.[6-16] While the investigations on cycloheptane and its isomer 1-heptene are much less than those of cyclohexane. Gusel'nikov et al. examined the very low-pressure pyrolysis (VLPP) coupled with low temperature matrix infrared spectroscopy method of cycloheptane and 1-heptene.[17] It was reported that isomerization of cycloheptane to 1-heptene was the primary initiation reaction (reaction (8.1)), and the decomposition reactions of cycloheptane mainly proceed via 1-heptene. The *γ*-scission (reaction (8.2)) and retro-ene mechanism (reaction (8.3)) were argued as the main decomposition pathways of cycloheptane or 1-heptene. Also, sequential H-atom loss reactions of cycloheptane leading to cycloheptene (reaction (8.4)), as well as its secondary reaction forming C_4H_6 and C_3H_6 (reaction (8.5)), were proposed. Besides, the formation of cyclopentane was found, and it was explained by the direct dissociation of the 1,7-heptyl diradical (reaction (8.6)). Liu et al. reported the flash pyrolysis of 1-heptene using vacuum ultraviolet single photon ionization time-of-flight mass spectrometry (VUV-SPI-TOFMS),[8] and the C_5H_{10} species was identified as a product. It was argued that the direct dissociations of the 1,7-heptyl diradical formed from the isomerization of 1-heptene produced the C_5H_{10} species (reaction (8.7)). Sikes et al.

using the shock tube technique at high temperatures of 1200-1650 K reported that the primary initial product in the cycloheptane pyrolysis is 1-heptene via two steps (ring opening to the 1,7-heptyl diradical and then isomerization to 1-heptene), which is similar to cyclohexane.[18] Similarly, they reported that the further secondary reactions were dominated by the 1-heptene pyrolysis mechanism, and reaction (8.2) was considered as the major decomposition channel. After comparing with other cycloalkane systems, they concluded that the ring-opening rate coefficient for cycloalkane is strongly dependent on molecular size, namely $k_{cyclopentane} << k_{cyclohexane} < k_{cycloheptane}$. These experimental investigations of the cycloheptane and cyclohexane pyrolysis have shown that the predominant initiation reaction channel is the ring-opening reaction in the cycloalkane leading to the formation of its corresponding diradical, followed by rapid isomerization to alkene.

$$\text{c-}C_7H_{14} \rightarrow CH_3(CH_2)_4CH{=}CH_2 \tag{8.1}$$

$$CH_3(CH_2)_4CH{=}CH_2 \rightarrow \cdot C_3H_5 + \cdot C_4H_9 \tag{8.2}$$

$$CH_3(CH_2)_4CH{=}CH_2 \rightarrow C_3H_6 + CH_2{=}CHCH_2CH_3 \tag{8.3}$$

$$\text{c-}C_7H_{14} \xrightarrow{-H} \text{c-}C_7H_{13} \xrightarrow{-H} \text{c-}C_7H_{12} \tag{8.4}$$

$$\text{c-}C_7H_{12} \rightarrow C_4H_6 + C_3H_6 \tag{8.5}$$

$$\text{c-}C_7H_{14} \rightarrow \cdot CH_2(CH_2)_5H_2C\cdot \rightarrow \text{c-}C_5H_{10} + C_2H_4 \tag{8.6}$$

$$\text{1-}C_7H_{14} \rightarrow \cdot CH_2(CH_2)_5H_2C\cdot \rightarrow \text{c-}C_5H_{10} + C_2H_4 \tag{8.7}$$

Theoretical chemistry studies have also been conducted focusing on the ring-opening mechanism of cycloalkanes.[18-20] Sirjean et al. examined the ring-opening mechanism of C4-C6 cycloalkanes at the CBS-QB3 level, and the energetics and geometries involving the C4-C6 diradicals were studied. The relevant dissociation kinetics were also reported.[20] Gong et al. explored the possible decomposition channels of cyclohexane at the CCSD(T)/cc-pVDZ//UBH&HLYP/cc-pVDZ level.[19] The direct decomposition of the $\cdot C_6H_{12}\cdot$ diradical leading to the C_4H_8 species as well as other products were studied. Sikes et al. examined the energetics and kinetics of the ring-opening reaction of cycloheptane, as well as the energetics of the β-scission reaction for 1-heptene at the CCSD(T)/cc-pV∞Z//M06-2X/cc-pVTZ level of theory.[18]

Many studies on the cycloalkane pyrolysis, especially cyclohexane, have been reported so far, while the studies of cycloheptane are much less. Also, the investigations on the initiation reactions, especially the reactive intermediates that are produced in the thermal decomposition of cycloalkanes, were less studied. In our previous studies, emphasis was made on the initiation reactions of cyclohexane, 1-hexene and 1-heptene pyrolysis.[6, 8] Therefore, investigating how the pyrolysis of cycloheptane is initiated is also important, which can not only further verify the mechanism that were proposed in our early works, but also contribute to a more comprehensive understanding of the pyrolysis mechanism of cycloalkanes. These motivations led us to investigate the flash pyrolysis mechanism of cycloheptane under unimolecular reaction conditions. In this chapter, the thermal decomposition mechanism of cycloheptane initiated by C-C bond rupture to the 1,7-heptyl diradical and isomerization to 1-heptene, followed by further dissociation of 1-heptene, was detected and characterized. Furthermore, evidence that supports the direct dissociation pathways of the 1,7-heptyl diradical is also found. Other possible initiation channels such as the H-loss channel of cycloheptane, as well as possible secondary reaction channels of cycloheptane, were examined. Density functional theory (DFT) calculations on their geometries and energetics were also performed to support experimental conclusions.

8.2 Experimental and computational methods

The flash pyrolysis of cycloheptane was performed using a home-made vacuum ultraviolet single-photon ionization time-of-flight mass spectrometer (VUV-SPI-TOFMS) coupled with a SiC tubular microreactor. The vapor of cycloheptane (98%, Sigma Aldrich) was diluted to around 1% in the He carrier gas. The backing pressure of the gas mixture before the pulse valve was 1050 torr.

Quantum chemistry calculations have been carried out on the energetics of the reactants, products, and transition states involved in this chapter. The energetics of each species were represented by its most stable configuration since the energy barriers for conformational change were negligible.[20] The geometries of those species were optimized using the DFT method at the UB3LYP/cc-pVDZ level. It could perform descent geometry optimizations with a relatively affordable cost.[20, 32] All transition states were verified using intrinsic reaction coordinate (IRC) calculations at the same level as geometry optimizations. The single-point energy was calculated using the UCCSD(T) method and with cc-pVDZ basis sets, and the zero-point energy corrections were made based on the frequency calculations at UB3LYP/cc-pVDZ level. All vibrational frequencies were scaled by 0.97 in this chapter as recommended by Sinha et al..[33] Notably, the energies of the singlet diradicals in this chapter were calculated using $E_{singlet} = 2E_{Guess=Mix} - E_{triplet}$,[6, 19, 34, 35] in which, the energy of the diradical with the “Guess=Mix” option was assumed as the average of the single point energy of its singlet configuration and triplet configuration. This method was used to resolve the spin contaminations caused by the mixing between singlet and triplet states of diradicals.[19, 35] The single-reference calculation approach in this chapter was similar to the method employed in Gong et al.[19] All the computational works were performed using Gaussian 09 package.[36]

8.3 Results and discussions

Figure 8.1 and 8.2 display the pyrolysis spectra of cycloheptane at temperatures from 298 K to 1380 K. The five mass spectra at temperatures between 350 K and 980 K were omitted in the figures since they were identical to that at 298 K. At room temperature (295 K), *m/z* = 98 peak and its isotopic peak *m/z* = 99 correspond to the parent molecule cycloheptane. The minor peak at *m/z* = 92 (C_7H_8) and 78 (C_6H_6) were probably produced by impurities in the sample, because they were minor fragments even in electron impact ionization with ~ 70 eV electron energy,[37] and therefore they were less likely to be dissociative photoionization products of cycloheptane by the 10.49 eV photoionization in this experiment. Furthermore, these two peaks had nearly constant intensities throughout all temperatures, suggesting their thermal stability and that they were impurities not involved in the cycloheptane thermal dissociation. Other trace peaks at 295 K, such as *m/z* = 42, 44, 45, and 55, 56, 58, were caused by a minor amount of dissociative photoionization of the parent molecule.[38]

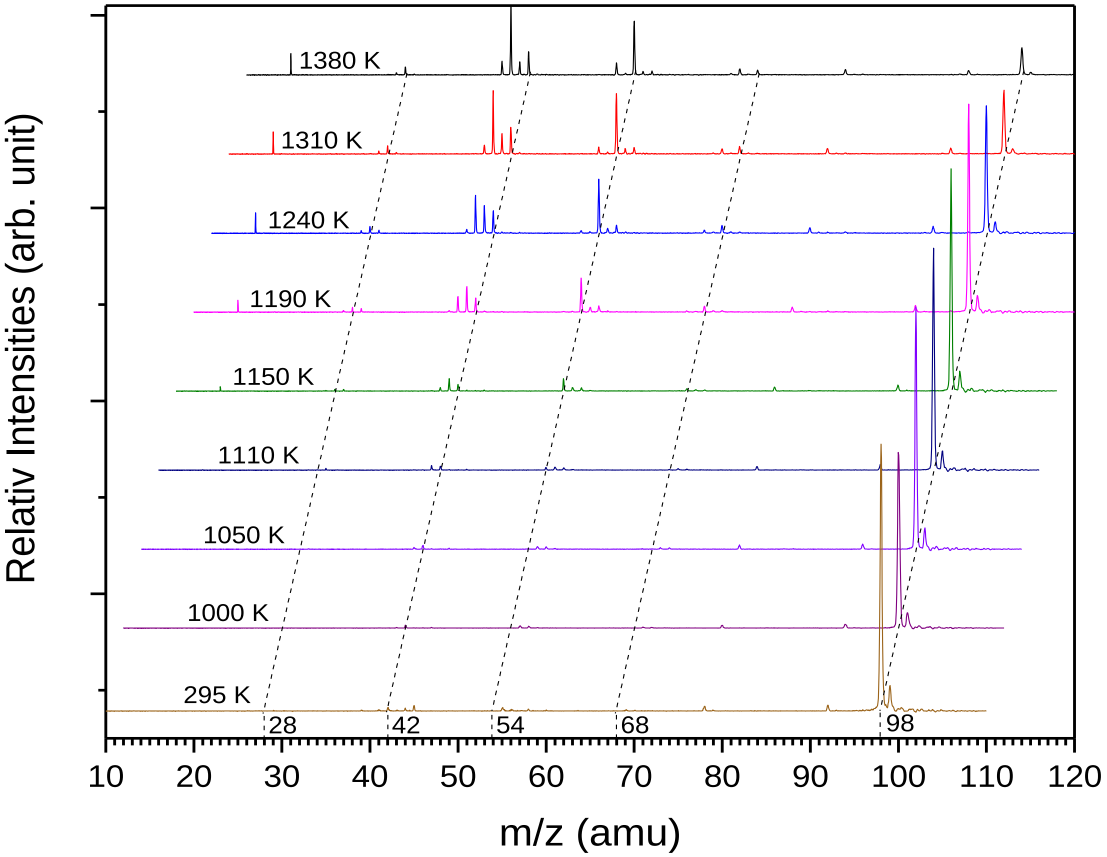

Figure 8.1 Mass spectra for the cycloheptane (1% diluted in helium) pyrolysis at 295 K to 1380 K. Five mass spectra at temperatures between 350 K and 980 K were essentially identical to that at 295 K and were omitted. The mass spectra are offset both horizontally and vertically for clarity. Detailed mass to charge ratio information is provided in Figure 8.2.

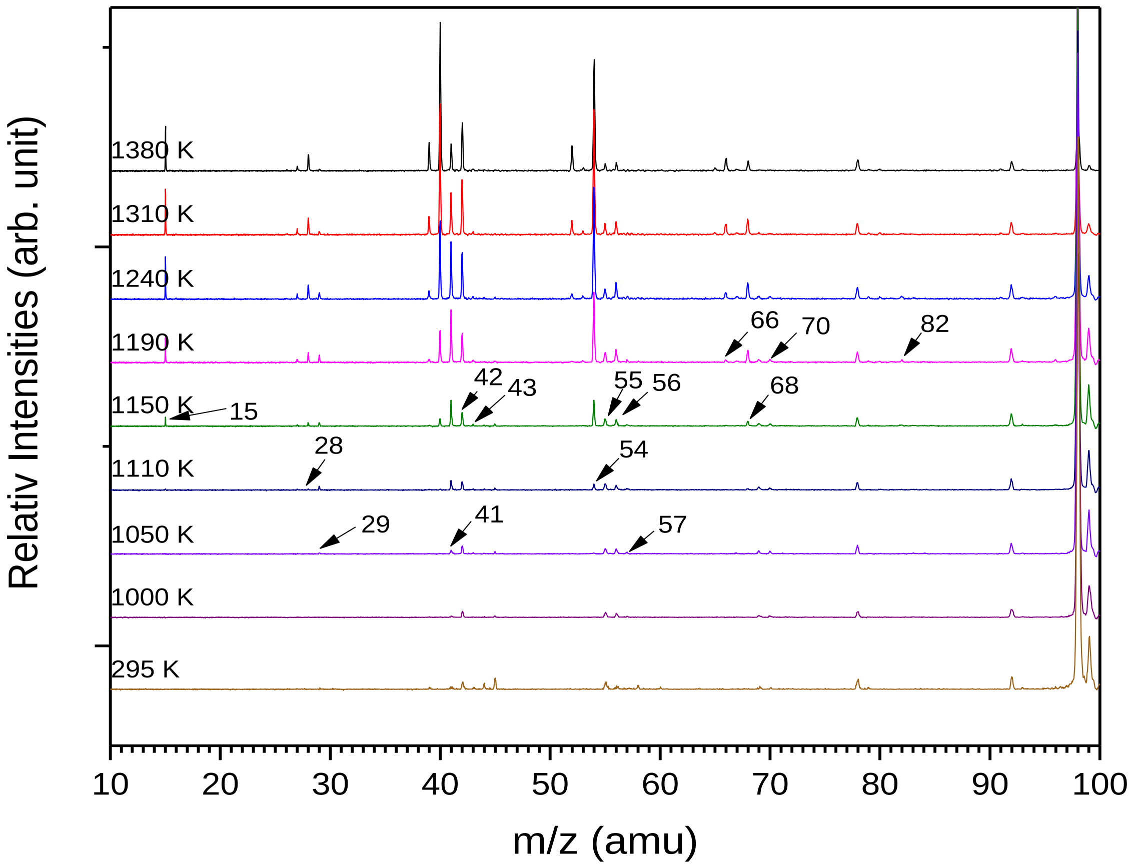

Figure 8.2 Enlarged mass spectra for the cycloheptane (1% diluted in helium) pyrolysis at 295 K to 1380 K. Five mass spectra at temperatures between 350 K and 980 K were essentially identical to that at 295 K and were omitted. The mass spectra are offset vertically for clarity.

(a) Initiation reactions

The studies of the cycloheptane pyrolysis in this chapter mainly focused on the initiation reactions. As inspired by our previous works on cyclohexane, 1-hexene, and 1-heptene,[6, 8] similar dissociation channels of cycloheptane via the formation of the 1,7-heptyl radical are proposed and depicted in Scheme 8.1. It is considered that cycloheptane initially undergoes the C-C bond fission and produces the 1,7-heptyl diradical. The 1,7-heptyl radical could have three possible decomposition channels. It could decompose into the 1,5-pentyl diradical via C2-C3 bond fission and quickly isomerize to 1-pentene or cyclopentane; it could also decompose into the 1,4-butyl diradical via C3-C4 bond breaking. Another reaction channel for the 1,7-heptyl diradical is to quickly isomerize to 1-heptene.

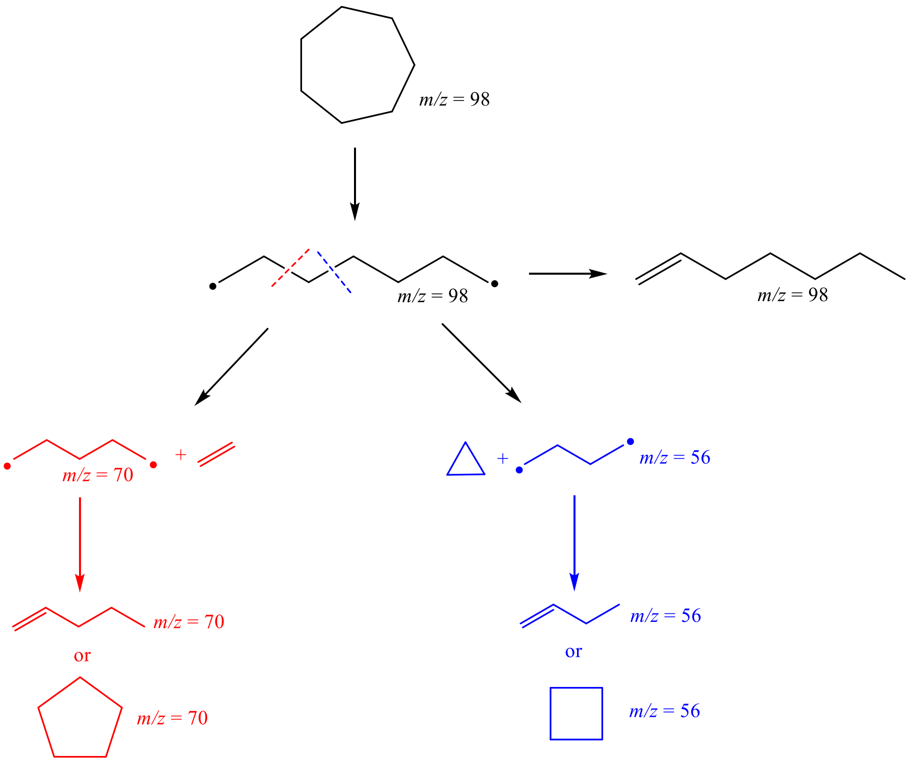

Scheme 8.1 Possible formation mechanism of the 1,5-pentyl diradical, the 1,4-butyl diradical, and 1-heptene from the 1,7-heptyl diradical in the initial steps of cycloheptane pyrolysis.

In the initial C-C bond breaking reaction that produces the 1,7-heptyl diradical, since cycloheptane, the 1,7-heptyl diradical, and 1-heptene all have the same mass-to-charge ratio, these isomers could not be identified by the mass spectra alone, and thus, it was difficult to obtain their relative populations at different temperatures in this chapter. According to the reaction energetics calculations that were summarized in Figure 8.3, the thermal dissociation was initiated by the C-C bond breaking of the cycloheptane, producing the $\cdot C_7H_{14}\cdot$ diradical via TS1. The lowest energy pathway of the 1,7-heptyl diradical is isomerization to 1-heptene via TS2, with a threshold energy of 4.4 kcal/mol. The β-scission of the 1,7-heptyl diradical could lead to the formation of the 1,5-pentyl diradical via TS3. Among the two exiting channels for the 1,7-heptyl diradical, according to the calculations, the TS2 has a lower threshold energy than the TS3 channel, which indicated that the isomerization between cycloheptane and 1-heptene was predominant. Unlike cyclohexane, the sequential H_2 elimination channel of cycloheptane was not observed,[6] probably due to a less stable ring configuration.

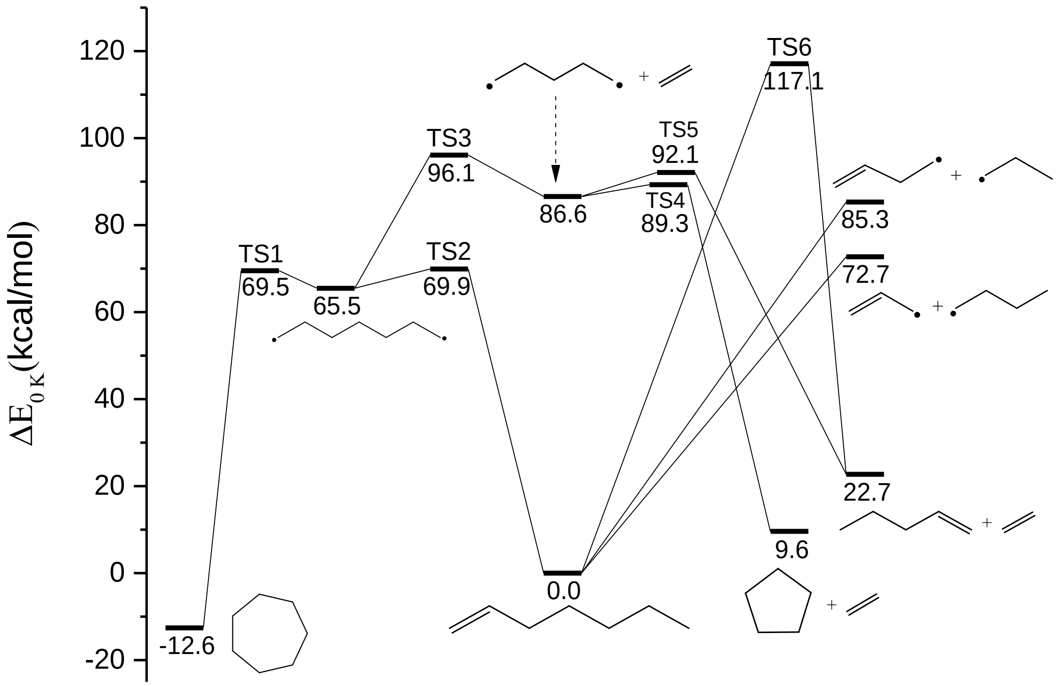

Figure 8.3 Energetics of the initiation reaction channels of cycloheptane and possible reaction pathways leading to the formation of the m/z = 70 products in the cycloheptane pyrolysis, and other reaction channels of the main initial reaction product, 1-heptene. All geometry optimizations and zero-point energy corrections were performed at UB3LYP/cc-pVDZ level. The single-point electronic energy of all species involved were performed at UCCSD(T)/cc-pVDZ level of theory. Detailed information of the calculated geometries of the transition states and related species is provided in Supplementary Material.

(a) Dissociation reactions of 1-heptene

Possible fragment signals produced by the secondary reactions of 1-heptene were found. The *m/z* = 41 (•C_3H_5) and *m/z* = 57 (•C_4H_9) peaks were captured as evidence supporting the mechanism of C3-C4 bond fission of 1-heptene (reaction (8.2)).[17, 18] Both peaks were detected at 1050 K. The intensity of the *m/z* = 41 peak increased with the temperature until 1310 K and then started to decrease as the temperature further increased, probably because it could further lose one hydrogen atom forming the C_3H_4 species.[8, 39] The signal of the *m/z* = 57 peak was weak when first observed at 1050 K, and it did not increase significantly as the temperature continued to build up, probably due to its unstable nature which may lead to the formation of smaller fragments. According to previous studies, the butyl radical could quickly decompose into C_2H_5 and C_2H_4 (reaction (8.8)) or C_4H_8 and H (reaction (8.9)).[18, 40] These were reasonably well reflected in our observations, as the *m/z* = 29 peak was first observed at the temperature of 1050 K. The onset temperature for reaction (8.2) is the lowest among all other initiation channels, which is consistent with that there is only a 72.7 kcal/mol threshold energy above 1-heptene which makes it the most energetically favorable pathway. Therefore, reaction (8.2) is considered to be the predominant pathway in the thermal decomposition of cycloheptane, and this conclusion is consistent with Gusel'nikov et al.[17] and Sikes et al..[18]

$$\bullet C_4H_9 \rightarrow \bullet C_2H_5 + C_2H_4 \qquad (8.8)$$

$$\bullet C_4H_9 \rightarrow C_4H_8 + \bullet H \qquad (8.9)$$

Other dissociation channels of 1-heptene were found. 1-heptene could decompose into $\bullet C_4H_7$ plus $\bullet C_3H_7$ via the C4-C5 bond fission (reaction (8.10)). According to Figure 8.1 and 8.2, the *m/z* = 55 signal was found to increase at around 1150 K. It suggested that the C_4H_7 species was less likely from the secondary reactions of C_4H_8 and instead from reaction (8.9), since the energy required to break the C-H bond (in C_4H_8) is higher than that of a C-C bond. Its counterpart signal *m/z* = 43 was first detected at 1150 K and without further increasing with the temperature. The weak signal of the *m/z* = 43 peak could be explained by the quick dissociation of $\bullet C_3H_7$ into C_2H_4 and $\bullet CH_3$ or C_3H_6 and $\bullet H$.[8] The detection of the *m/z* = 15 peak (CH_3) at 1150 K was consistent with this assumption. The

C5-C6 bond rupture of 1-heptene, producing $\cdot C_5H_9$ followed by a quick H-loss reaction leading to the C_5H_8 species, could readily explain the appearance of the *m/z* = 68 signal at 1150 K. And it is considered that the C5-C6 bond fission reaction took place at around 1150 K. The *m/z* = 66 signal was found at 1190 K, and it could be due to the sequential H_2 elimination reaction of the *m/z* = 68 species. Similarly, the *m/z* = 82 peak (C_6H_{10}) that first appeared at 1190 K could be explained by the secondary reaction of the methyl-loss product of 1-heptene (C_6H_{11} radical). No *m/z* = 97 signal (for the *c*-heptyl radical from C-H fission) was observed at all the elevated temperatures. There was a very minor, tentative signal at *m/z* = 96 found only at 1190 and 1240 K. The appearance of a minor *m/z* = 27 peak at 1150 peak was unusual as similar observations were not found in the cyclohexane pyrolysis under similar experimental conditions. It could possibly be produced by secondary dissociations of initiation reaction fragments with larger masses. As will be discussed later in the text, the direct dissociation of 1-heptene to 1-pentene was considered trivial, and the formation of the *m/z* = 70 species could possibly be explained by the further reactions of the 1,7-heptyl diradical.

$$1\text{-}C_7H_{14} \rightarrow \cdot C_4H_7 + \cdot C_3H_7 \qquad (8.10)$$

The energetics for the 1-heptene dissociations were also calculated. As discussed in the previous section, the isomerization of the 1,7-heptyl diradical to 1-heptene was predominant. According to the calculations shown in Figure 8.3, there are three possible dissociation channels for 1-heptene. Among them, the C3-C4 bond fission producing $\cdot C_4H_9$ and $\cdot C_3H_5$ has the lowest threshold energy, which is 72.7 kcal/mol relative to 1-heptene, while the energy threshold for the C4-C5 bond fission forming $\cdot C_4H_7$ and $\cdot C_3H_7$ is 85.3

kcal/mol. It was consistent with the experimental observations that the C3-C4 bond fission took place at the temperature of 1050 K, while the onset temperature for the C4-C5 bond fission was determined as 1150 K. The energy barrier for the 1-pentene formation (TS6) is 117.1 kcal/mol, and therefore this channel is considered insignificant.

1.2 The dissociations of the 1,7-heptyl diradical

The possible experimental evidence for the two possible dissociation channels of the 1,7-heptyl diradical was also found. As shown in Figure 8.1 and 8.2, the *m/z* = 70 peak (C_5H_{10}) was first found to increase at 1190 K. Its intensity did not grow significantly with the temperature; the ratio of peak areas *m/z* 70/98 is displayed in Figure 8.4 to indicate the onset temperature for reaction (8.6).[22] The grow of the curve suggests the positive contributions from the thermal decomposition reactions.[22] As shown in Figure 8.4, the ratio curve remained almost constant at low temperatures and started to increase at around 1190 K. The curve increased gradually as the temperature further increased. The 1,5-pentyl diradical (*m/z* = 70) might be less stable, and it might quickly isomerize to cyclopentane (or 1-pentene). The observation of *m/z* =70 is consistent with the production of cyclopentane from direct dissociation of the 1,7-heptyl diradical (reaction (8.6)), which was observed in the VLPP coupled with low temperature matrix infrared spectroscopy.[17] At higher temperatures, further dissociations of the resulting cyclopentane or 1-pentene took place, which might explain why the intensity of the *m/z* = 70 peak did not increase significantly with temperatures. C_2H_4 (*m/z* = 28), the counterpart of the 1,5-pentyl diradical, was also identified at 1190 K.

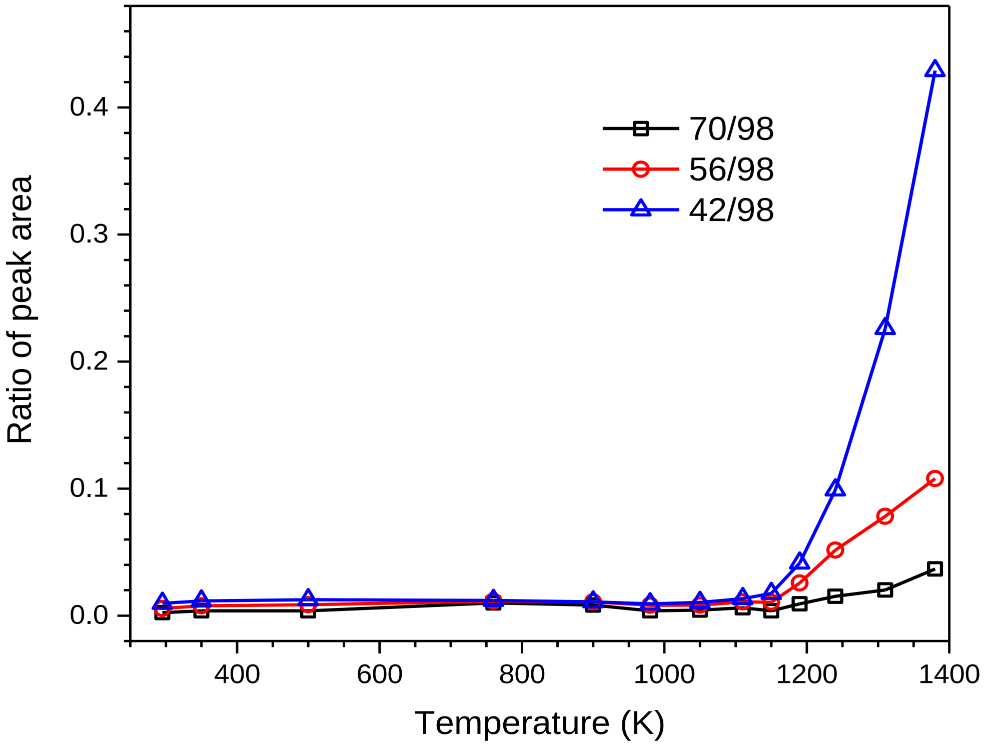

Figure 8.4 Ratio of peak area of m/z = 42 (C_3H_6), 56 (C_4H_8) and 70 (C_5H_{10}) with respect to the parent peak (C_7H_{14}) in the cycloheptane pyrolysis.

The energetics regarding the formation of the *m/z* = 70 peak in the cycloheptane pyrolysis were also shown in Figure 8.3. According to the calculations displayed in Figure 8.3, the energy barrier via TS3 is 30.6 kcal/mol for the 1,7-heptyl diradical to overcome. The 1,7-heptyl diradical could be energetically activated from additional collisions with the He carrier gas molecules to overcome the energy barrier. The 1,5-pentyl diradical (C_5H_{10}) has two isomerization channels, to cyclopentane via TS4 with an energy barrier of 2.7 kcal/mol, and through TS5 to 1-pentene with an energy barrier of 5.5 kcal/mol. As TS3 is higher in energy than TS4 and TS5, the β-scission of the 1,7-heptyl diradical to the 1,5-pentyl diradical could facilely lead to the cyclopentane or 1-pentene product. This is consistent with the observation of the *m/z* = 70 peak around the onset decomposition temperatures, and is also supported by the observation of cyclopentane by the low temperature matrix infrared spectroscopy in the VLPP study.[17] The C_5H_{10} species could also be produced from the secondary reactions of 1-heptene via TS6, with a threshold energy of 117.1 kcal/mol. However, this reaction pathway required more energy than the previous mechanism via TS4 or TS5, which indicated that the formation of *m/z* = 70 peaks was more likely caused by the direct dissociation of the $\cdot C_7H_{14}\cdot$ diradical. In addition, since the bimolecular reactions were minimized, the C_5H_{10} species were most likely produced by the unimolecular dissociation of the 1,7-heptyl diradical.

The *m/z* = 56 peak, which was the signal of 1,4-butyl diradical ($\cdot C_4H_8\cdot$) and 1-butene, was also observed. This peak was observed as a very minor photoionization fragmentation signal at the room temperature of 295 K. At around 1150 K, its intensity started to grow, and further increased with the increasing temperature. Figure 8.4 shows the ratio of peak area of *m/z* 56/98. It indicates that below ~ 1150 K, the curve is almost constant and when the temperature reached 1150 K, the curve started a sharp increase, indicating the formation of the C_4H_8 species. The C_4H_8 species (*m/z* = 56) could be evolved from the diradical mechanism (reaction (8.11)). However, the quantum calculation results did not support this pathway, since the calculated energy barrier for reaction (8.11) is almost 25 kcal/mol higher than that of reaction (8.6). The C_4H_8 species could also be formed from the H-loss decomposition of the $\cdot C_4H_9$ radical (reaction (8.9)) that was produced in the secondary reactions of 1-heptene, as the *m/z* = 57 peak was first observed at 1110 K, prior to the increase of the *m/z* = 56 signal.[41] Therefore, the formation of the *m/z* = 56 species was possibly caused by the secondary reactions of the butyl radical ($\cdot C_4H_9$), and hence, could not serve as a direct evidence for the diradical mechanism. The *m/z* = 42 peak was found to increase at ~ 1150 K simultaneously with the *m/z* = 56 peak. Similarly, the secondary reactions of $\cdot C_3H_7$ could also lead to the formation of the *m/z* = 42 peak (reaction (8.12)).

$$c\text{-}C_7H_{14} \leftrightarrow \cdot CH_2(CH_2)_5H_2C\cdot \rightarrow \cdot CH_2(CH_2)_2H_2C\cdot + C_3H_6 \qquad (8.11)$$

$$\cdot C_3H_7 \rightarrow C_3H_6 + \cdot H \qquad (8.12)$$

(b) Secondary reactions

Figure 8.1 and 8.2 also provide evidence for a series of secondary reactions at higher temperatures. In addition to the secondary reactions discussed above, the *m/z* = 54 peak (C_4H_6) was first captured at 1110 K, which was likely the further secondary reaction product of the $\cdot C_4H_9$ radical that was produced in reaction (8.2). The *m/z* = 52 first appeared at 1240 K, and it could be produced by the further H_2 elimination of C_4H_6. The *m/z* = 40 peak was first observed at 1150 K, and it could be formed from a H-loss channel of the allyl radical (*m/z* = 41).[22, 39] As the temperature further increased, the *m/z* = 39 peak was first captured at 1240 K, and it was probably produced by the H-loss channel of the C_3H_4 species.

8.4 Conclusions

The initial decomposition mechanism of cycloheptane was studied using a short residence time tubular microreactor coupled with single-photon ionization time-of-flight mass spectrometry from 295 K to 1380 K. Quantum chemistry calculations were also carried out to investigate the energetics of the initiation reaction channels. It was shown that the thermal decomposition of cycloheptane was initiated at around 1050 K via C-C bond rupture and ring opening to the 1,7-heptyl diradical, which readily isomerizes to 1-heptene that dissociates to the C_4H_9 and C_3H_5 radicals, and the produced 1-heptene could also decompose into C_4H_7 and C_3H_7 radicals, with the onset temperature determined to be 1190 K. It was also suggested that the direct dissociation of the 1,7-heptyl diradical is the pathway responsible for the formation of the $m/z = 70$ species.

Overall, the cycloheptane pyrolysis has shown similarities with the pyrolysis of cyclohexane, especially for the initiation reaction mechanism, and yet, it also showed some differences compared to cyclohexane, as the sequential H_2 elimination channels in cycloheptane were not found. The main initiation reaction channels of cycloheptane decomposition, as well as some other products from the secondary reactions of the initiation reaction products, are summarized in Scheme 8.2. This chapter, as well as the previous work on the 1-hexene and 1-heptene pyrolysis by Liu et al.[8] and on the cyclohexane pyrolysis by Shao et al.,[6] has provided insights into further numerical modeling studies on similar cycloalkane systems.

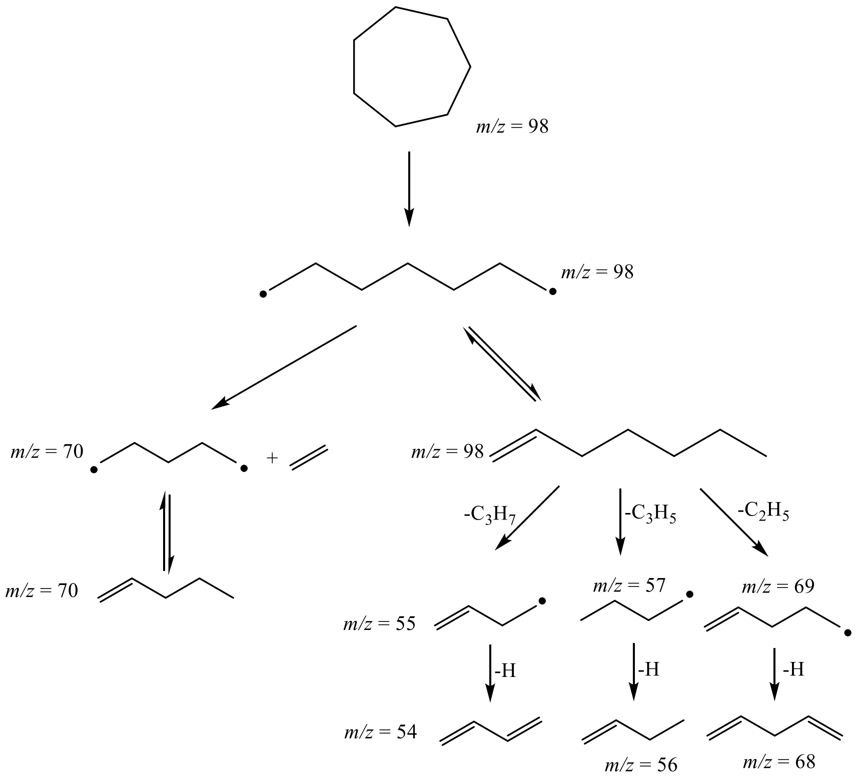

Scheme 8.2 Main initiation decomposition pathways of cycloheptane and important secondary reactions in the cycloheptane pyrolysis.

REFERENCE

1. G. W. Huber, S. Iborra and A. Corma, *Chemical Reviews*, 2006, **106**, 4044-4098.

2. A. M. Mastral and M. S. Callén, *Environmental Science & Technology*, 2000, **34**, 3051-3057.

3. E. Ranzi, A. Cuoci, T. Faravelli, A. Frassoldati, G. Migliavacca, S. Pierucci and S. Sommariva, *Energy & Fuels*, 2008, **22**, 4292-4300.

4. W. Jin, L. Pastor-Pérez, D. Shen, A. Sepúlveda-Escribano, S. Gu and T. Ramirez Reina, *ChemCatChem*, 2019, **11**, 924-960.

5. L. Mo, W. Yu, H. Cai, H. Lou and X. Zheng, *Frontiers in Chemistry*, 2018, **6**.

6. K. Shao, X. Liu, P. J. Jones, G. Sun, M. Gomez, B. P. Riser and J. Zhang, *Physical Chemistry Chemical Physics*, 2021, **23**, 9804-9813.

7. M. Yahyaoui, N. Djebaïli-Chaumeix, C. E. Paillard, S. Touchard, R. Fournet, P. A. Glaude and F. Battin-Leclerc, *Proceedings of the Combustion Institute*, 2005, **30**, 1137-1145.

8. X. Liu, W. Yuan, J. Zhang, J. Yang and Z. Zhou, *Proceedings of the Combustion Institute*, 2021, **38**, 651-659.

9. W. Tsang, *International Journal of Chemical Kinetics*, 1978, **10**, 1119-1138.

10. D. S. Aribike, A. A. Susu and A. F. Ogunye, *Thermochimica Acta*, 1981, **51**, 113-127.

11. D. Voisin, A. Marchal, M. Reuillon, J. C. Boettner and M. Cathonnet, *Combustion Science and Technology*, 1998, **138**, 137-158.

12. A. El Bakali, M. Braun-Unkhoff, P. Dagaut, P. Frank and M. Cathonnet, *Proceedings of the Combustion Institute*, 2000, **28**, 1631-1638.

13. U. Steil, M. Braun-Unkhoff, C. Naumann and P. Frank, in *Proceedings of the European Combustion Meeting*, Louvain-la-Neuve, Belgium April 3−6, 2005.

14. J. H. Kiefer, K. S. Gupte, L. B. Harding and S. J. Klippenstein, *The Journal of Physical Chemistry A*, 2009, **113**, 13570-13583.

15. Z. Wang, Z. Cheng, W. Yuan, J. Cai, L. Zhang, F. Zhang, F. Qi and J. Wang, *Combustion and Flame*, 2012, **159**, 2243-2253.

16. D. S. Aribike and A. A. Susu, *Applied Petrochemical Research*, 2018, **8**, 193-201.

17. L. E. Gusel'nikov, V. V. Volkova, P. E. Ivanov, S. V. Inyushkin, L. V. Shevelkova, G. Zimmermann, U. Ziegler and B. Ondruschka, *Journal of Analytical and Applied Pyrolysis*, 1991, **21**, 79-93.

18. T. Sikes, K. B. Burdett, R. L. Speth, C. F. Goldsmith, R. Sivaramakrishnan and R. S. Tranter, *Proceedings of the Combustion Institute*, 2021, **38**, 929-937.

19. C.-M. Gong, Z.-R. Li and X.-Y. Li, *Energy & Fuels*, 2012, **26**, 2811-2820.

20. B. Sirjean, P. A. Glaude, M. F. Ruiz-Lopez and R. Fournet, *The Journal of Physical Chemistry A*, 2006, **110**, 12693-12704.

21. S. D. Chambreau, J. Zhang, J. C. Traeger and T. H. Morton, *International Journal of Mass Spectrometry*, 2000, **199**, 17-27.

22. K. Shao, Y. Tian and J. Zhang, *International Journal of Mass Spectrometry*, 2021, **460**, 116476.

23. X. Liu, J. Zhang, A. Vazquez, D. Wang and S. Li, *The Journal of Physical Chemistry A*, 2019, **123**, 10520-10528.

24. D. W. Kohn, H. Clauberg and P. Chen, *Review of Scientific Instruments*, 1992, **63**, 4003-4005.

25. K. Shao, Y. Tian and J. Zhang, *The Journal of Physical Chemistry A*, 2022, **126**, 1085-1093.

26. S. D. Chambreau and J. Zhang, *Chemical Physics Letters*, 2001, **343**, 482-488.

27. S. D. Chambreau, J. Lemieux, L. Wang and J. Zhang, *The Journal of Physical Chemistry A*, 2005, **109**, 2190-2196.

28. Q. Guan, K. N. Urness, T. K. Ormond, D. E. David, G. Barney Ellison and J. W. Daily, *International Reviews in Physical Chemistry*, 2014, **33**, 447-487.

29. K. Shao, J. Brunson, Y. Tian and J. Zhang, *International Journal of Mass Spectrometry*, 2022, **482**, 116933.

30. P. J. Jones, B. Riser and J. Zhang, *The Journal of Physical Chemistry A*, 2017, **121**, 7846-7853.

31. K. H. Weber, J. M. Lemieux and J. Zhang, *The Journal of Physical Chemistry A*, 2009, **113**, 583-591.

32. E. Kraka and D. Cremer, *Journal of the American Chemical Society*, 2000, **122**, 8245-8264.

33. P. Sinha, S. E. Boesch, C. Gu, R. A. Wheeler and A. K. Wilson, *The Journal of Physical Chemistry A*, 2004, **108**, 9213-9217.

34. D. H. Ess, E. R. Johnson, X. Hu and W. Yang, *The Journal of Physical Chemistry A*, 2011, **115**, 76-83.

35. T. Ziegler, A. Rauk and E. J. Baerends, *Theoretica chimica acta*, 1977, **43**.

36. G. W. T. M. J. Frisch, H. B. Schlegel, G. E. Scuseria, M. A. Robb, J. R. Cheeseman, G. Scalmani, V. Barone, B. Mennucci, G. A. Petersson, H. Nakatsuji, M. Caricato, X. Li, H. P. Hratchian, A. F. Izmaylov, J. Bloino, G. Zheng, J. L. Sonnenberg, M. Hada, M. Ehara, K. Toyota, R. Fukuda, J. Hasegawa, M. Ishida, T. Nakajima, Y. Honda, O. Kitao, H. Nakai, T. Vreven, J. A. Montgomery, Jr., J. E. Peralta, F. Ogliaro, M. Bearpark, J. J. Heyd, E. Brothers, K. N. Kudin, V. N. Staroverov, R. Kobayashi, J. Normand, K. Raghavachari, A. Rendell, J. C. Burant, S. S. Iyengar, J. Tomasi, M. Cossi, N. Rega, J. M. Millam, M. Klene, J. E. Knox, J. B. Cross, V. Bakken, C. Adamo, J. Jaramillo, R. Gomperts, R. E. Stratmann, O. Yazyev, A. J. Austin, R. Cammi, C. Pomelli, J. W. Ochterski, R. L. Martin, K. Morokuma, V. G. Zakrzewski, G. A. Voth, P. Salvador, J. J. Dannenberg, S. Dapprich, A. D. Daniels, Ö. Farkas, J. B. Foresman, J. V. Ortiz, J. Cioslowski, and D. J. Fox, *Gaussian 09*, (2009), Wallingford, CT.

37. W. E. W. NIST Mass Spectrometry Data Center, director, NIST Chemistry WebBook, NIST Standard reference database number 69, Eds. P.J. Linstrom and W.G. Mallard, National Institute of Standards and Technology, Gaithersburg MD, 20899, https://doi.org/10.18434/T4D303, (retrieved November 2, 2020).

38. O. Kostko, B. Bandyopadhyay and M. Ahmed, *Annual Review of Physical Chemistry*, 2016, **67**, 19-40.

39. B. S. Narendrapurapu, A. C. Simmonett, H. F. Schaefer, J. A. Miller and S. J. Klippenstein, *The Journal of Physical Chemistry A*, 2011, **115**, 14209-14214.

40. J. B. Randazzo, R. Sivaramakrishnan, A. W. Jasper, T. Sikes, P. T. Lynch and R. S. Tranter, *Physical Chemistry Chemical Physics*, 2020, **22**, 18304-18319.

41. V. D. Knyazev and W. Tsang, *The Journal of Physical Chemistry A*, 2000, **104**, 10747-10765.

CHAPTER 9 Conclusion

9.1 Summary of works

In Chapter 3 to Chapter 6 of this thesis, the flash pyrolysis mechanism for allyltrichlorosilane, allyltrimethylsilane, 1,1,2,2-tetraethylsilane, trimethylchlorosilane, and tetraethylsilane were reported. In the decomposition of allyltrichlorosilane, Si-C bond cleavage is the initial step, producing $\bullet SiCl_3$ and $\bullet C_3H_5$, which then undergo further reactions. In allyltrimethylsilane, three main initial reaction products were considered. The study found that allyltrichlorosilane decomposes primarily via Si-C bond homolysis, while allyltrimethylsilane decomposes via both molecular eliminations and Si-C bond fissions. The study on the isolated allyl reactions in allyltricholorosilane helped to unravel the complex decomposition mechanism of allyltrimethylsilane. In the pyrolysis study of 1,1,2,2-tetramethylsilane, four major initiation steps were identified, including molecular elimination reaction, Si-Si bond fission, H_2 elimination, and decomposition to trimethylsilane and methylsilylene. The most kinetically favored reaction was found to be the molecular elimination reaction, and the overall mechanism of 1,1,2,2-tetramethyldisilane pyrolysis was summarized. In the pyrolysis study of trimethylchlorosilane, the predominant pathway was found to be the HCl molecular elimination channel of the parent molecule producing HCl and $Me_2Si=CH_2$ via a van der Waals intermediate. The onset temperature for this reaction was around 1210 K, and the appearance of $SiCl_2$ signals at high temperatures was believed to be involved with minor bimolecular reactions. The pyrolysis study of tetraethylsilane revealed that the Si-C bond homolysis was found to be the predominant reaction pathway in the initiation step, and the unimolecular rate constant calculations revealed that the rate constant of the Si-C bond fission channel was significantly higher than the β-hydride elimination pathway. Several secondary reactions were identified, including the further dissociation reaction of $HSiEt_2$ and possible dissociation channels of $HSiEt_2$ and $:SiEt_2$, which led to the formation of various species.

Chapter 7 and Chapter 8 discussed the thermal decomposition mechanism of two aviation fuel prototypes, cyclohexane and cycloheptane. In the mechanistic study of the cyclohexane pyrolysis, the main initiation reaction pathway was the C-C bond rupture of cyclohexane, producing the 1,6-hexyl diradical, and the key evidence for the direct dissociation of the 1,6-hexyl diradical was found. The study also found that the pyrolysis of cyclohexane did not produce the $\bullet C_6H_{11}$ radical by C-H bond fission, and direct evidence for the sequential H_2 eliminations leading to the formation of benzene was found. In the study of cycloheptane pyrolysis, the decomposition was initiated at around 1050 K via C-C bond rupture and ring opening to the 1,7-heptyl diradical, which isomerizes to 1-heptene that dissociates to C_4H_9 and C_3H_5 radicals. The main initiation reaction channels and some secondary reaction products of cycloheptane decomposition were summarized. These two studies provided new insight into numerical modeling studies on similar cycloalkane systems.

9.2 General knowledge

In this study, the experimental investigations have yielded intricate details regarding the reaction intermediates, reactants, and products, presenting a much more comprehensive understanding of the pyrolysis system that traditional methods could not offer. From a theoretical standpoint, we have focused on the molecular-level properties of the species involved, including their molecular structure, energetics, and rate constants of elementary reactions. Through an examination of the thermodynamics and kinetics of the pyrolysis systems, this work has further contributed to establishing a correlation between the overall pyrolysis mechanism and the molecular-level chemical properties of the species involved.

For example, In Chapter 3, the pyrolysis mechanisms of allyltrichlorosilane and allyltrimethylsilane were investigated. The mass spectra analysis yielded crucial experimental information, revealing the presence of C_3H_6 in the pyrolysis of allyltrimethylsilane. However, the competing bond homolysis channel products, C_3H_5, were also observed. In the absence of additional experimental evidence to determine the more dominant reaction pathway, quantum chemistry calculations were employed. These calculations demonstrated that the molecular elimination channel, which produced C_3H_6, was more favored, leading to the conclusion that it was the predominant channel. Furthermore, while the experimental evidence detected smaller fragments, it did not provide insights into the responsible reaction pathways for these species. Computational chemistry bridged this gap by establishing connections between the potential reactants and products, offering justifications for their likelihood.

This comprehensive investigation demonstrated its effectiveness in exploring complex pyrolysis systems, as exemplified in Chapter 4. The thermal decomposition mechanism of 1,1,2,2-tetramethyldisilane was examined in this chapter. Given the intricate nature of the parent molecule, the mass spectra exhibited a complex pattern with numerous small peaks, posing challenges in determining the reaction pathway. To gain deeper insights into the decomposition characteristics of this system, systematic theoretical calculations were performed to investigate the initiation reaction mechanism. These calculations revealed four potential initiation reaction pathways. By further exploring these major initiation channels and their subsequent reactions, additional components of the species involved in this system could be connected, leading to a satisfactory explanation of the pyrolysis mechanism. Furthermore, energetics calculations played a crucial role by providing criteria to substantiate the significance of each reaction pathway. This comprehensive approach facilitated a thorough understanding of the intricate pyrolysis process of 1,1,2,2-tetramethyldisilane.

Theoretical calculations of energetics not only offer powerful explanations for the pyrolysis mechanism but also enable the prediction of reaction products, thereby constructing hypotheses for research. In Chapter eight and nine, the thermal decomposition of cyclohexane and cycloheptane was investigated. Prior to conducting the pyrolysis experiments on these two systems, theoretical calculations were performed. The results of these calculations indicated that the 1,6-hexyl diradical or 1,7-heptyl diradical could potentially undergo further decomposition reactions, resulting in the formation of C_4H_8 and C_5H_{10} as possible products. Theoretical calculations further suggested that the appearance of these two peaks in the mass spectra could only be attributed to the direct dissociation of their corresponding diradicals. Consequently, before conducting the experiments, the primary objective shifted to identifying the signals of these specific species. Subsequent experimental results validated this prediction, thus confirming this long debated diradical mechanism.

These examples illustrate thermodynamically controlled reactions. However, for reactions that are kinetically controlled, relying solely on thermodynamic calculations of the energetics is insufficient to elucidate the reaction mechanism. In such cases, additional kinetic calculations are necessary to provide a comprehensive understanding of the decomposition mechanism.

Chapter 6 focused on the pyrolysis study of tetraethylsilane. The experimental findings clearly demonstrated the feasibility of the Si-C homolysis channel as the predominant initiation step, while the β-hydride elimination channel remained unobserved. However, in the energetic calculations, both pathways exhibited comparable energy barriers, and the Si-C homolysis channel did not exhibit a significant advantage over its competing pathway, which required a well-defined transition state, as observed experimentally. This scenario represents a classic example of a kinetic-controlled reaction. In the Si-C bond homolysis channel, although the energy required for bond-breaking was similar to that of the transition state route, it did not necessitate a specific transition state structure, providing more flexibility in bond cleavage. Consequently, from a statistical perspective, the bond homolysis reaction was more favored compared to its competing transition state route to molecular elimination. To validate this theory, transition state theory calculations were conducted. The results revealed that, across all temperature ranges, the rate constants for the Si-C bond homolysis reaction were five orders of magnitude higher than those for the competing molecular elimination reaction. This example revealed the importance of kinetics investigations in the study of pyrolysis mechanisms.

Those examples have demonstrated the utilization of the VUV-TOFMS experimental method as a means to obtain crucial mass signal information, as well as the use of thermodynamic and/or kinetic calculations to assemble evidence and develop a comprehensive pyrolysis mechanism. In future studies, it is recommended to employ this combination method. Prior to conducting experiments, conducting a literature search or theoretical calculations is advised to identify potential intermediates or products in the system. Thermodynamics of each reaction pathway can be estimated based on the relative stability of the involved species, while kinetics can be assessed by evaluating the flexibility of the transition state or trial transition states, as well as the energetics of these specific reaction routes. Additionally, future investigations should focus on refining kinetic modeling, such as incorporating calculations of reaction conditions and monitoring the time evolution of key relevant species. These investigations necessitate a detailed characterization of the fluid dynamics within the microreactor.

In conclusion, the pyrolysis mechanism of a specific system can be elucidated through two complementary approaches. First, the analysis of key reactive intermediates obtained from mass spectra provides valuable insights. Second, theoretical calculations offer understanding of the specific reaction energetics involved. While experimental results help bridge gaps in our knowledge, theoretical calculations serve to connect missing pieces and construct a comprehensive overview of the mechanism.